UNIVERSITÀ
DI PARMA

Department of Chemistry, Life Sciences and
Environmental Sustainability

# Functional Luminescent Materials for Two-Photon Applications

Domna-Maria Nikolaidou

Supervisor: Prof. Francesca Terenziani

Coordinator: Prof. Enrico Dalcanale

A thesis presented for the degree of
Doctor of Philosophy in Material Science
Cycle XXIX

Parma, Italy
April 2017

*Dedicated to my family*

*"Ta panta rhei"*
(Everything flows)
Heraclitus

This PhD thesis leading to these results received funding from the People Programme (Marie Curie Actions) of the European Union’s Seventh Framework Programme FP7/2007-2013 under REA grant agreement no. 607721 (ITN Nano2Fun).

# Contents

# Abstract

Novel organic materials with luminescent properties and non-linear response are studied in this PhD work. Organic nanoparticles, easily obtained via the reprecipitation method, and thin films have been developed and characterized for application based on Two-Photon Absorption.

At the beginning of the thesis, the reprecipitation method was optimized. A number of aspects that can affect and modify the process, such as the chemical composition of the starting material, the influence of concentration and the solvent effects were studied. Our results indicate that the molecular geometry and the way of packing of molecules within the particles are important, and the optimal final concentration of the chromophore in suspension is $\leq 10^{-5}$ M in order to present some fluorescence. The optimized conditions were followed for the preparation of all the successive suspensions.

Core@Shell@Shell and Composite ternary organic nanoparticles were designed, prepared and investigated. In the multicomponent nanoparticles an excitation energy-transfer cascade between the different molecular components occurs, with an enhancement of luminescence in the red spectral region. The two-photon brightness of the ternary nanoparticles is greatly enhanced with respect to that of the single-component nanoparticles. In particular they can be two-photon excited over a broad spectral range (from 600 nm to 1200 nm) inside the biological transparency window. This property, together with good luminescence in red spectral region and good colloidal stability in aqueous suspension, suggests that these fully organic multicomponent nanosystems can be potential nanoprobes for Two-Photon bioimaging.

Moreover the luminescence properties of new materials based on open-shell molecular systems were studied. Organic nanoparticles and polymeric films doped with carbon-centered radicals, namely polychlorotriphenylmethyl radicals, were prepared and optically characterized. The luminescence properties of these binary systems are improved with respect to molecule in solution or in the solid state. Organic nanoparticles and films with low radical doping exhibit up to 10 times higher luminescence quantum yield than the radical in solution. Increasing the radical doping leads to a progressive decrease of the luminescence quantum yield and the appearance of a new broad excimeric band at longer wavelengths. The formation of excimers from stable and persistent supramolecular radical-pairs was observed here for the first time. The good stability and luminescence properties with emission in the red-NIR region (650-800 nm), together with the open-shell nature of the emitter, make these free-radical excimer-forming materials candidates for optoelectronics and bioimaging applications.

A part of the thesis is devoted to the work I performed during my secondments in University of Sloupsk (Poland) and in University of Bordeaux (France), and it is related to Two-Photon Polymerization. Particularly, fluorescence is applied to monitor the photo-polymerization process and the organic synthesis of an asymmetric aldehyde as Two-Photon initiator it is described.

The final part of the thesis summarizes the outreach activities performed during my training period in the framework of the Nano2Fun ITN project and of the International Year of Light 2015.

# Acknowledgements

The defence of a PhD thesis is a hard and long process, that would not materialized, without the contribution of a number of people. Firstly, I would like to express my sincere gratitude to my advisor Prof. Francesca Terenziani for the continuous support of my PhD study and related research, for her guidelines and immense knowledge. Her notifications helped me in all the time of research and writing of this thesis.

My PhD has been an amazing experience, that took place in the frame of Marie Curie European Project "Nano2Fun". Thanks to funding from Nano2fun and its network, I had the opportunity to visit a number of laboratories in different countries, to attend meetings and conferences, and collaborate with scientists in multidisciplinary field. I would like specially thank Prof. Anna Painelli, the coordinator of the project, Dr. Cristina Sissa and Dott. Paola Rossi, for the administrative help.

I would like to extend thanks to the many people, in many countries, who contributed to the work that is presented, during my secondments. My sincere thanks go to Prof. Jaume Venciana, Prof. Mireille Blanchard-Desce, Prof. Vladimir Tomin, Prof. Eric Vauthey, who provided me the opportunity to join their laboratories and have access to their research facilities. Moreover, I would like to appreciate Dr. Imma Ratera, Dr. Antonio Bautista, and the PhD students Davide Blassi and Dimitri Ushakou for their collaboration.

Special mention goes to my labmates, Somananda Sanyal, Sergei Kurhuzenkau,

Francesco Di Maiolo, Francesca Delchiaro and Nicola Castagnetti, for the stimulating discussions, the encouraging and the excellent coexistence, all these three years. Further I would like to thank my personal friends Dr. Konstantinos Konstantinou and Dr. Panagiotis Giounanlis for their constant support during my PhD studies.

Finally, but by no means least, thanks go to my mother and my father for their personal and mental encouragement. They are really important for me and I would like to dedicate this thesis to them.

# Acronyms

**2PA** Two Photon Absorption

**2PM** Two Photon Microscopy

**2PP** Two Photon Polymerization

**TPEF** Two Photon Excited Fluorescence

**ACQ** Aggregation Cause Quenching

**AIE** Aggregation Induced Emission

**RIR** Restriction of Intramolecular Rotation

**DLS** Dynamic Light Scattering

**PDI** Polydispersity Index

**EET** Excitation Energy Transfer

**FONs** Fluorescent Organic Nanoparticles

**ICT** Intramolecular Charge Transfer

**LQY** Luminescence Quantum Yield

**ONPs** Organic Nanoparticles

**OLED** Organic Light-Emitting Diode

**WOLED** Organic White Light-Emitting Diode

**TEM** Transmission Electron Microscopy

**RET** Resonance Energy Transfer

**TTM** tris 2,4,6-trichlorophenyl methyl

**PTM** perchlorotriphenylmethyl

**TTMaH** tris 2,4,6-trichlorophenyl methane

**PMMA** Poly(methyl methacrylate)

**THF** Tetrahydrofuran

**2MeTHF** 2-Methyl Tetrahydrofuran

**DCM** Dichloromethane

**ITN** Initial Training Network

# Chapter 1

# Introduction

An enormous development of applications based on the two-photon absorption (2PA) process has been achieved during the last decades. 2PA has important applications in three-dimensional optical data storage [1,2], photolithography [3,4], scanning fluorescence microscopy [5–8], optical power limiting [9, 10] etc. Meanwhile, many organic compounds with 2PA properties have been proposed and synthesised, and new supramolecular structures such as dendrimers [11], nanoparticles [12, 13] or thin films [14] with sought non-linear response have been developed. Although, in the field of photonics the production of novel materials with non-linear optical properties, optimized performance and low-cost is a constant demand.

To define suitable materials for these applications, one has to analyse carefully their optical characteristics. For instance, in imaging applications an important issue for two-photon probes is their one- and two-photon absorption spectral range and intensity as well as sizeable to good luminescence in the sought spectral range. Moreover photostability and toxicity should be taken into account. Hence, the optimization strategy is not always straightforward.

This thesis is devoted to study aggregation and confinement effects on optical properties of materials based on organic chromophores. Luninescence characteristics of organic nanoparticles and films have been examined and energy transfer phenomena in nanoassemblies are exploited to optimise their performance as materials for applications in two-photon microscopy (2PM) and in two-photon polymerization (2PP).

The thesis is structured according to the following: Chapter 1 introduces the main concept of two-photon absorption and its major applications; two-photon microscopy and two-photo polymerization are outlined. Aggregation and confinement effects on optical properties of molecules are discussed and a brief introduction on the excitation energy transfer is given. Chapter 2 focuses on the preparation and study of fluorescent organic nanoparticles. The preparation method of nanoparticles from organic chromophores, namely reprecipitation, is introduced and preliminary spectroscopic results are presented. Chapter 3 is devoted to synthesis of multicomponent organic nanoparticles for application in two-photon microscopy. Energy transfer phenomena inside the nanoparticles are exploited to extend the excitation range still having emission in the red spectral region (transparency window of biological tissues) and to enhance their two-photon response. In Chapter 4 we present a systematic study of linear and non linear optical properties of organic radicals in solution, in nanoparticles and films. Organic nanoparticles and thin films doped with radical molecules have been prepared and examined, and the formation of excimers is discussed. Chapter 5 concentrates on two-photon polymerization. Fluorescence spectroscopy is applied to monitor the photo-polymerization process. Further, the organic synthesis of an asymmetric aldehyde meant to work as initiator for two-photon polymerization is described. Chapter 6 is devoted to communication of science to the general public. A series of experiments related to basic optical phenomena, performed during public demonstrations, is described.

## 1.1 Two-Photon Absorption

For high intensity light, the interaction with a material becomes non-linear and phenomena such as multiphoton absorption can occur [15–17]. Two-photon absorption (2PA) is a third-order nonlinear optical process in which a molecule absorbs two photons of equal or different energies simultaneously and is promoted from the ground state to a higher-energy electronic state.

The polarization of the material is:

$$\boldsymbol{P} \; = \boldsymbol{\chi}^{(1)}\varepsilon \; + \boldsymbol{\chi}^{(2)}\varepsilon^2 \; + \boldsymbol{\chi}^{(3)}\varepsilon^3 \; + \boldsymbol{\chi}^{(4)}\varepsilon^4 ... + \boldsymbol{\chi}^{(n)}\varepsilon^n \tag{1.1}$$

$\varepsilon$ is the amplitude of the electric field, the quantities $\boldsymbol{\chi}^{(1)}$, $\boldsymbol{\chi}^{(2)}$, $\boldsymbol{\chi}^{(3)}$ and so forth, are tensors representing the first (linear), second-order and third-order optical susceptibilities. Energy and momentum can be exchanged between electromagnetic fields and molecules, through absorption and emission. The light-matter energy exchange per unit time and volume is given by the equation:

$$\frac{dW}{dt} \; = \langle \hat{P} \frac{d\vec{E}}{dt} \rangle \tag{1.2}$$

where $\vec{E}$ is the electric field vector, $\hat{P}$ is the polarization operator and the brackets denote the time average.

Even-order processes cannot exchange energy (except from the case of at least one static field), so that they are described by the real part of the relevant susceptibilities ($\boldsymbol{\chi}^{(2)}$, $\boldsymbol{\chi}^{(4)}$) . Only odd-order processes can occur with energy exchange. In particular, the non-linear absorption is described by the imaginary part of $\boldsymbol{\chi}^{(3)}$, $\boldsymbol{\chi}^{(5)}$, of which typical effects are two-photon and three-photon absorption respectively.

The two-photon absorption can be degenerate or nondegenerate. In degenerate two-photon absorption (fig.1.1), two photons of identical energy are absorbed simultaneously. In nondegenerate two-photon absorption two photons of different energies are absorbed simultaneously to promote the molecule to an excited state. Since two photons (either degenerate or not) are used to reach the excited state, typically NIR or red light is needed, instead of UV-Vis as required by linear absorption.

For degenerate 2PA, the energy absorption rate is:

$$\frac{dW}{dt} = \frac{3}{8}\omega I^2 Im[\boldsymbol{\chi}^{(3)}] \tag{1.3}$$

where *I* is the intensity of the electromagnetic field. It is seen that the 2PA rate has a quadratic dependence on the light intensity. The capability of the material to absorb photons via 2PA process is described by the value of the 2PA cross section $\sigma_2$ :

$$\frac{dn_p}{dt} = \sigma_2 N F^2 \tag{1.4}$$

where $N$ and $n_p$ are the number density of absorbing molecules and the number of absorbed photons, respectively. $F = I/\hbar\omega$ denotes the photon flux. 2PA was theoretically predicted by Maria Goeppert-Mayer in 1931 and the two-photon absorption cross section is quoted in units **Goeppert-Mayer (GM)**. According to eq.1.4 the 2PA cross section is:

$$\sigma_2 = \frac{24\pi^2\,\hbar\omega^2}{c^2 n^2 N}\, Im[\boldsymbol{\chi}^{(3)}] \tag{1.5}$$

The most widespread methods to measure two-photon absorption cross section are the Z-scan technique and the two-photon excited fluorescence (TPEF) technique. The Z-scan method is based on the measurement of the nonlinear transmittance of a sample [18, 19]. The transmittance is measured as a function of the intensity as the sample is scanned through the focal plane of a tightly focused Gaussian laser beam (Z-position). In non-resonant conditions, a 2PA process is characterized by a decrease in the transmittance which is used to extract the magnitude of the non-linear process. The TPEF technique measures the fluorescence signal induced by two-photon absorption and derives the TPEF action cross section ($\sigma_2\Phi$, where $\Phi$ is the fluorescence quantum yield) by comparison to a reference compound or to the one-photon excited fluorescence of the same compound [15, 20]. In this thesis, the two photon absorption cross section was measured by TPEF and the technique is described in detail in Appendix 1.

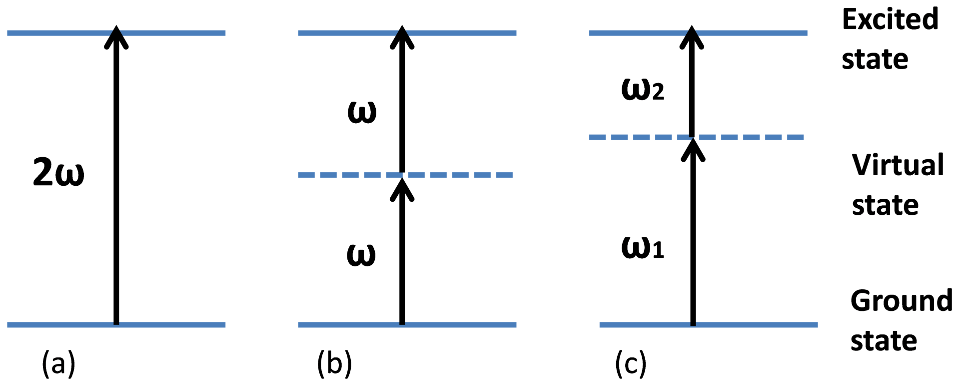

Figure 1.1: (a) One-photon absorption; (b) Degenerate two-photon absorption; (c) Nondegenerate two-photon absorption.

For 2PA applications, molecules with large values of 2PA cross section are required. Molecular design of compounds with large 2PA cross-section typically includes: a long conjugated $\pi$-backbone system with a planar conformation; the presence of electron-donor (D) and electron-acceptor (A) groups able to promote an intense displacement of charge during the transition. Typically, molecular structures that show strong two-photon absorption are donor-bridge-acceptor (D-$\pi$-A) dipolar structures, donor-bridge-donor (D-$\pi$-D), acceptor-bridge-acceptor (A-$\pi$-A), donor-acceptor-donor (D-$\pi$-A-$\pi$-D) and acceptor-donor-acceptor (A-$\pi$-D-$\pi$-A), the latter four corresponding to quadrupolar structures [11, 21, 22].

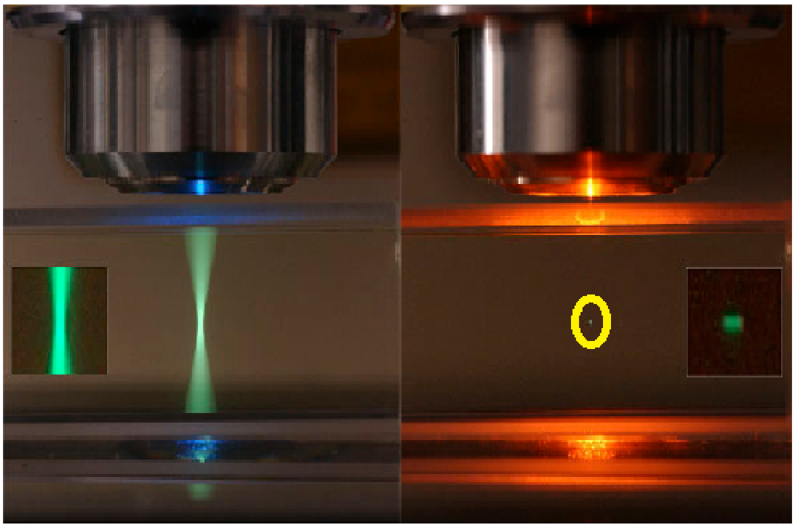

Figure 1.2: One-photon and Two-photon excited fluorescence of a dilute fluorescein sample in a quartz cuvette. The blue laser (488 nm) excites, via one-photon, an entire column of sample (left). The NIR pulse laser excites, via two-photon absorption, only a small volume within 3-D localised spot (right). Image copyright S. Ruzin and H. Aaron, UC Berkeley.

Since the 2PA probability is proportional to the square of the light intensity, the two-photon excitation will occur in a tiny volume (order of magnitude: femtoliter) close to the focal point of the incident laser beam. The excitation rate for 2PA and the intensity of the two-photon induced fluorescence decrease as the forth power of the distance from the focal plane. In the solution in fig.1.2 the two-photon induced fluorescence is sizeable at the beam focus and its intensity drops off very quickly on either side of the focal plane, resulting in what looks like emission from a single point (small volume, actually) in the solution. This volume is the so-called **Voxel** corresponding to the intrinsic 3-D resolution that the process provides. Two-photon microscopy and two-photon polymerization exploit this ability to confine and control the excitation volume in a material with good resolution in three dimensions.

### 1.1.1 Two-Photon Microscopy

One of the most important applications based on two-photon absorption lies in the field of microscopy. 2-Photon Fluorescence Microscopy (2PM) exploits the two-photon excitation (fig.1.3) of a fluorophore and provides unique capabilities in the field of 3-D microscopy [5, 8]. The first two-photon microscope was introduced by Denk et al at the beginning of 1990 [7]. Two-photon excitation in combination with a microscope occurs only at the focal point of a diffraction-limited spot and it is possible to create thin optical sections of thick biological samples in order to obtain three dimensional resolution. 2PM microscopy excels at high-resolution imaging in thick tissues such as brain slices, embryos, whole organs, and live animals [23]. Moreover, 2PM has become an important technique to monitor dynamic processes such as protein folding in nanometer dimension, both in time and in space [24, 25].

The technique has some major advances over confocal microscopy for 3-D imaging. First of all, the penetration depth of red or near-infrared light typically used for two-photon excitation is much deeper than that of visible light used in conventional confocal microscopy. Two-photon excitation of thick biological samples allows imaging to depths of more than 200 $\mu$m. Moreover, molecules are excited at the focal plane only, therefore no pinhole is required like in conventional confocal microscopy. In addition, two-photon excitation minimizes photobleaching and photodamage that are usually limiting factors in conventional live cell imaging. Non linear microscopy also offers the possibility to image through other non linear process such as second and third harmonic generation (SHG and THG respectively). With SHG imaging for example, tissue structures like collagen and muscle fibers can be imaged without labelling [26].

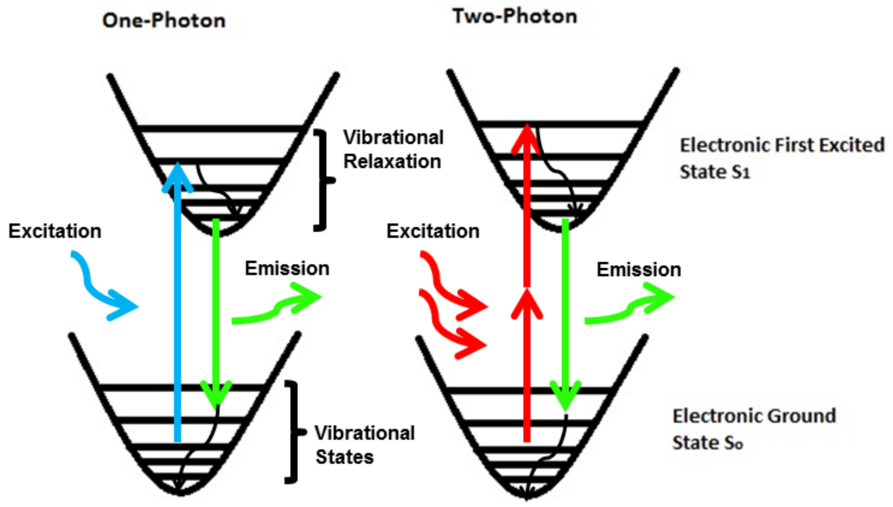

Figure 1.3: Jablonski diagram for one and two photon excitation. Excitation occurs from the ground state $S_o$ to the first excited state $S_1$ through the absorption of one photon (left) or simultaneously two lower-energy photons (right). After either the excitation, the molecule relaxes to the lowest excited state via internal relaxation. The subsequent fluorescence emission is the same independently of the excitation process.

A two-photon microscope is designed with three basic elements. An excitation light source, a high through put scanning fluorescence microscope and a high detection system. The setup of a typical commercially available microscope is reported in fig. 1.4 [27]. In fig.1.5 is reported an image upon 3-D image reconstruction of genetically dual coloured labelled cancer cells spheroids in a collagen matrix, obtained via a two-photon microscope.

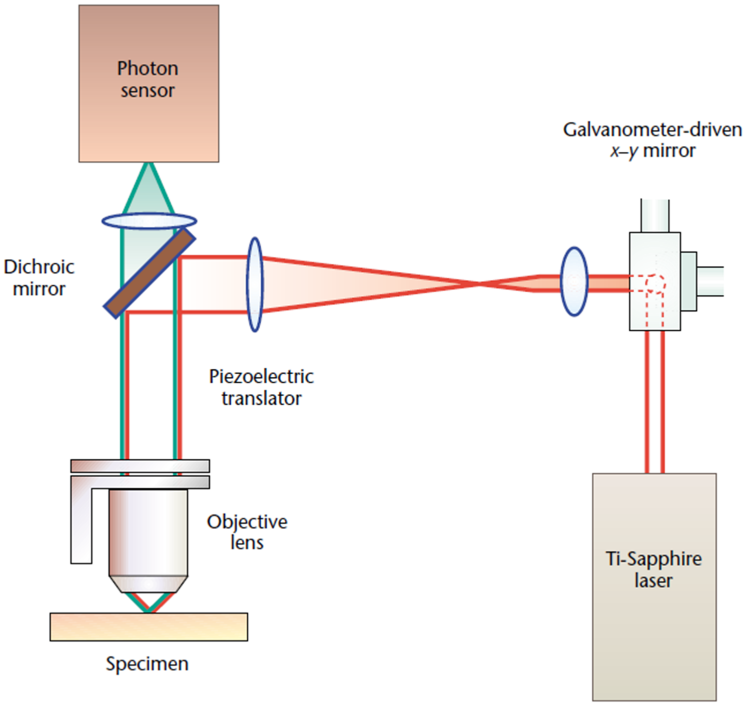

Figure 1.4: A schematic drawing of typical components in a two-photon microscope. Scheme copyright ref. [27]

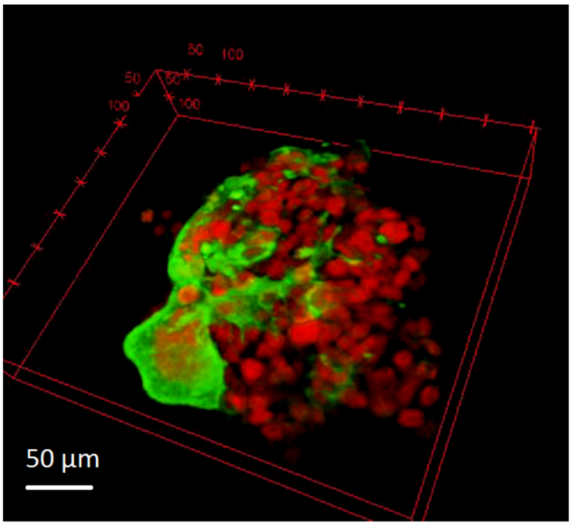

Figure 1.5: Image of dual coloured labelled cancer cells spheroids in a collagen matrix, obtained via 2PM.

Today, two-photon microscopy has a great impact in areas such as physiology, neurobiology, embryology, for which imaging of highly scattering tissues is required. Highly opaque tissues such as human skin have been visualized with cellular detail [28].

### 1.1.2 Two-Photon Polymerization

Another important application based on two-photon absorption is the two-photon polymerization (2PP). The process was reported for the first time in 1965 by Pao and Rentzepis, as an example of multiphoton induced chemical reaction [29]. Today, this method represents a promising three dimensional technique for micro and nano fabrication in various fields of industry [30–32].

Photo-polymerization refers to the process of using light as an energy source to induce the conversion of small molecules in the liquid state to solid macromolecules through polymerization reactions [33]. The basic components of the starting liquid material (the so-called resist) are monomers and/or oligomers. An important feature of polymerization is the chain reaction by which macromolecules are created, and given by the following equation:

$$M \xrightarrow{M} M_2 \xrightarrow{M} M_3 \, ...M_{n-1} \xrightarrow{M} M_n$$

Here $M$ is the monomer or oligomer unit and $M_n$ the macromolecule containing $n$ monomer units. In order to initiate the polymerization, one or several low-weight molecules that are more sensitive to light irradiation are added. They form initiating species of radicals or cations upon photoexcitation. Such small molecules are called photoinitiators and the process of production of active species that attack monomers or oligomers is called photoinitiation. The photoinitiation is possible to occur via one photon or multiphoton absorption (two-photon, three photon and so on).

The 2PP provide a number of advantages in the field of micro and nanofabrication. First of all, it has intrinsic ability to produce 3D structures. In addition, the long wavelength required for 2PA has less linear absorption and less scattering, which gives rise to deeper penetration of light. The use of ultrashort pulses can start intense non-linear processes at relatively low average power, without thermally damaging the samples.

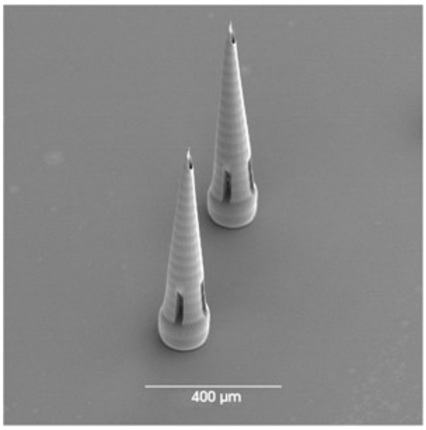

Figure 1.6: SEM image of microneedles for drug delivery fabricated by two-photon polymerization. Image copyright ref. [34].

Two types of photosensitive materials can be structured by two-photon polymerization: negative and positive-tone photoresists. With negative-tone photoresists, two-photon exposure results in cross-linking of polymer chains, allowing the unexposed resist to be washed out. With positive-tone resists, light exposure leads to chain scission, creating shorter units that can be dissolved and washed away in the development process. The technique is effective for the fabrication of micro-optical components and devices such as microprism arrays, diffractive optical elements or graphic microstructures (fig.1.7). Further, the two-photon polymerization technique is promising for biological applications, including tissue engineering, drug delivery, medical implants and medical sensors [30–32]. Figure 1.6 shows microneedle arrays for transdermal delivery of a wide diversity of pharmacologic agents, fabricated via two-photon polymerization [34].

Figure 1.7: SEM image of Nano2Fun logo fabricated via two-photon polymerization in Laser Zentrum Hannover (LZH) during the 5th meeting of ITN Nano2Fun.

## 1.2 H and J aggregates

Aggregation effects have strong impact on optical properties of a material. The aggregates in solution exhibit distinct changes in the absorption band as compared to single molecules. Intermolecular interactions have significant role and the spectroscopic characteristic of compounds are ruled by them [35]. According to well-established theories, the pattern of aggregation can be guessed taking into account absorption spectral shifts. Commonly, aggregates are classified as J-aggregates and as H-aggregates. J-aggregates absorption spectrum shifts to longer wavelength with respect to monomer. The J refers to E.E. Jelley who discovered the phenomenon in 1936. Examples of J-aggregate-forming dyes are polymethine dyes, cyanines, merocyanines, squaraines. J-aggregates are characterised by high luminescence quantum yields. H-aggregates show a blue shift in absorption spectra with respect to monomer and are typically non-fluorescent (fig.1.8).

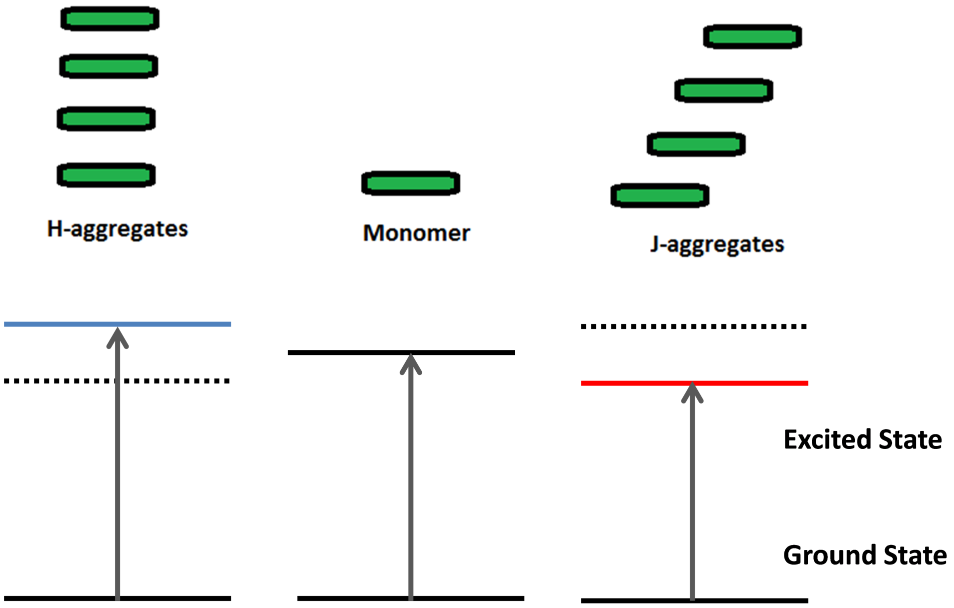

Figure 1.8: Electronic transition corresponding to molecular arrangement of one-dimensional H-aggregates and J-aggregates.

The linear optical properties of J-aggregates and H-aggregates are commonly intepreted by Frenkel molecular exciton theory [36]. Over the last 20 years studies of optical properties of supramolecular aggregates have been carried out with the aim of discovering their potential as nonlinear optical materials. Theoretical predictions of strong enhancements of a nonlinear optical response in molecular aggregates have been made by McRae et al and Spano et al. There are noumerous references reporting J-aggreagates with enhanced 2PA with respect to monomers. G.D'Avino et al.report amplified by orders of magnitude of two-photon absorption cross section in J-aggregates of quadrapolar dyes. [37]. K.Belfild et al. report strong enhancement of the two-photon absorption cross-section of pseudocyanines in supramolecular J-aggregate assembly in aqueous solution [38]. Kim et al. report anthrancine J-aggregates with enhanced fluorescence and large two photon absorption cross section [39].

On this basis, we are motivated from this strategy and in this thesis aggregation effects are exploited. We present different possibilities to generate highly luminescent materials together with a strong non-linear response. Particularly, monocomposite nanoparticles, multicomponent nanoparticles, core@shell@shell nanoparticles, nanoparticles doped with radical molecules and thin films are prepared and studied.

## 1.3 Theory of Excitation Energy Transfer

Transfer of excitation energy of a molecule (donor) to another (acceptor), is a photophysical process that occurs in a variety of physical, chemical or bio systems. Natural processes such as photosynthesis, energy transfer among DNA nucleobases [40], bioluminescence [41] of proteins [42] are typical paradigms of energy transfer in nature. A number of applications and techniques such as FLIM [43] or FRET [44] in fluorescence microscopy are based on that principle, and widely used for the fundamental study of bio-systems. The sensitivity of fluorescence and the nanoscale range upon which these phenomena occur, provide a significant detection tool in life science. Excitation Energy Transfer is a powerful tool for determining distances comparable to the range of few of tens Ångstroms, e.g. distance between two chromophores in a macromolecule, size of biological macromolecules, information on the expression of proteins, thickness of biological membranes [45–47].

The energy transfer can be divided in **heterotransfer** and **homotransfer**. When energy transfer occurs from a chromophore (D) to another (A) that is chemically different, the process is called heterotransfer and is described according to the expression:

$$D^* + A \rightarrow D + A^*$$

where the * denotes the excited species. If the donor and acceptor are identical, we can have homotransfer. When homotransfer occurs repeatedly over long distance, it is called **excitation transport** or **energy migration**.

Another important distinction is among **radiative** and **non-radiative** transfer. In radiative mechanism, the donor molecule is excited and emits a photon. This emitted field works as excitation source for an acceptor molecule. Such transfer is possible to occur when the distance between Donor-Acceptor is larger than the wavelength of the emitted radiation. The efficiency of the process depends on the overlap between the emission spectrum of donor and absorption spectrum of acceptor and on the concentration.

Antithetically, non-radiative transfer occurs without emission of real photons, when distance between D and A is shorter than the wavelength and arises from interaction between the donor and acceptor. The nature of interactions involved in non-radiative energy transfer interactions can be either Coulombic either due to intermolecular orbital overlap.

### 1.3.1 Förster Resonance Energy Transfer

The Coulomb interaction can be approximated by long range dipole-dipole interactions [48, 49]. A good approximation, when dipole-dipole interactions are dominant, has been given by the German scientist Theodor Förster [50]. In this approximation the efficiency of resonance energy transfer (RET) depends upon the following factors:

- The spectral overlap between emission of donor and absorption of acceptor:

  $$J = \int I_D(\lambda)\epsilon_A(\lambda)\lambda^4 d\lambda \tag{1.6}$$

  where $I_D$ is the fluorescence spectrum of the donor normalized to unit area, $\epsilon_A$ is the molar extinction coefficient of acceptor.

- The luminescence quantum yield of donor ($\Phi_D$).

- The orientation between donor and acceptor dipole moments.
- The distance between the two molecules.

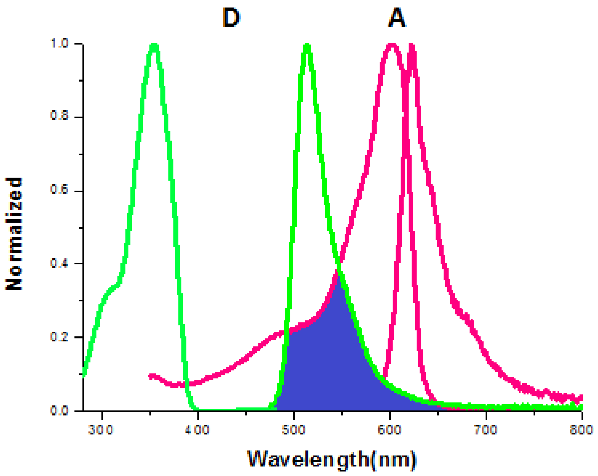

Figure 1.9: Absorption and emission of a donor-acceptor pair. The emission spectrum of donor (green) overlaps with the absorption spectrum of acceptor (red).

The dipole-dipole energy transfer rate, proposed by Förster [50] is given by the following equation:

$$k_{RET} = \frac{9 \times 10^{52} ln(10)}{1280\pi^5 N_A n^4} \frac{\kappa^2}{R_{DA}^6} \frac{\Phi_D^o}{\tau_D} J \tag{1.7}$$

$\tau_D$ is the donor emission lifetime in the absence of acceptor, $R_{DA}$ is the distance between the donor and the acceptor, $\kappa^2$ is the orientation factor, $\Phi_D^0$ is the fluorescence quantum yield of the donor in the absence of acceptor, $N_A$ is Avogadro number, $n$ is the refractive index and $J$ is the spectral overlap between emission of donor and absorption acceptor (eq.1.6). The characteristic inverse sixth power dependence on distance should be noted and the typical range is from 10 to 100 Å.

The orientation factor $\kappa^2$ is given by the formula:

$$\kappa^2 = (\cos\theta_{DA} - 3\cos\theta_D\cos\theta_A)^2 \tag{1.8}$$

or

$$\kappa^2 = (\cos\theta_D\sin\theta_A cos\phi - 2\cos\theta_D\cos\theta_A)^2 \tag{1.9}$$

In this formula $\theta_{DA}$ is the angle between the transition dipole moment of donor and acceptor, $\theta_D$ and $\theta_A$ angles are the angles between these, respectively, and the separation vector, $\phi$ is the angle between the projections of the transition moments on a plane perpendicular to the line through the centers (see fig.1.10). According to the relevant orientation of transition moments of donor and acceptor, $\kappa^2$ ranges from 0 to 4, perpendicular and collinear transitions taking values 0 and 4, respectfully. For parallel dipole moments $\kappa^2 = 1$. Often, molecules are free to rotate at faster rate than the de-excitation rate of the donor, so that the average value of $\kappa_2 = 2/3$ has to be considered. When the medium is rigid, i.e. a viscous solvent or a solid matrix, the random orientantion does not change during the lifetime of the excited state, and in this case $\kappa^2 = 0.476$. Fluorescence anisotropy measurements can set boundaries on $\kappa$ values [51] that can reduce the uncertaines in calculated distance.

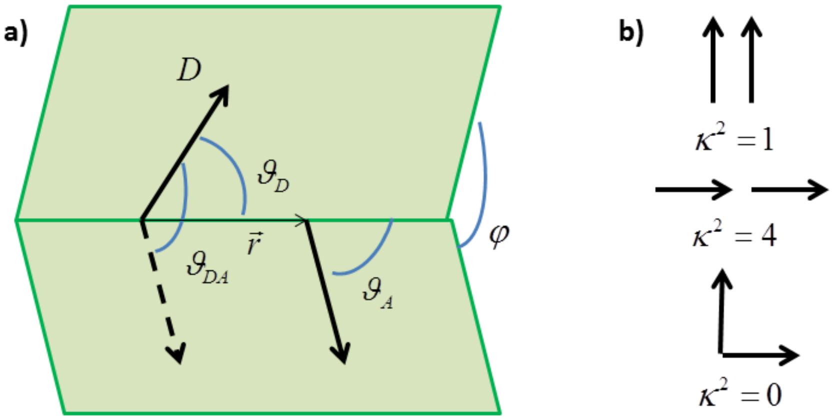

Figure 1.10: (a) Angles defined the D-A mutual orientation; (b) Transition dipoles configuration and orientation factor $\kappa^2$ .

The critical distance where RET is 50% efficient is called Förster radius. The Förster radius can easily estimated from the spectral properties of the isolated donor and acceptor molecules:

$$R_0^6 = \frac{9 \times 10^{52} ln(10) \kappa^2 \Phi_D^o}{1280 \pi^5 N_A n^4} J \tag{1.10}$$

The efficiency of Förster Resonance Energy Transfer (FRET) process is the fraction of photon absorbed by the donor that is transferred to the acceptor. In terms of rate, the fraction can be written:

$$E = \frac{k_T}{\tau_D^{-1} + k_T} \tag{1.11}$$

i.e. the ratio of the transfer rate to the total decay rate of the donor. The efficiency will be now:

$$E = \frac{R_0^6}{R_0^6 + R_{DA}^6} \tag{1.12}$$

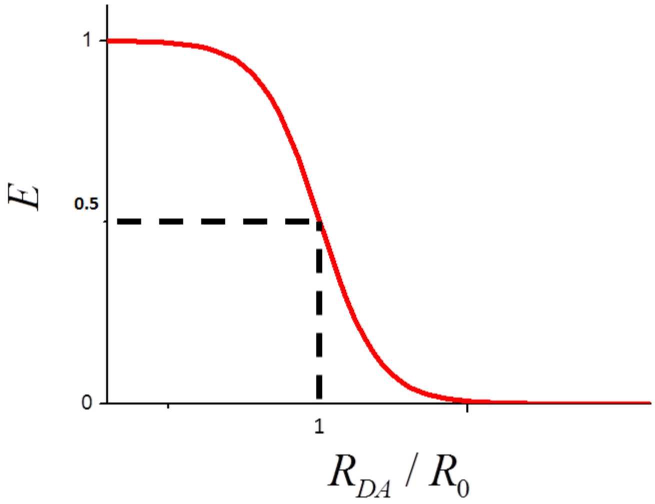

Figure 1.11: The resonance energy transfer efficiency is a sigmoid funtion of distance ratio $R_{DA}/R_0$.

Generally, the efficiency can experimentally be estimated by fluorescence measurements. Either the data of fluorescence intensity, either the data of lifetime decays of donor, in absence $(F_D, \tau_D)$ and presence $(F_{DA}, \tau_{DA})$ of acceptor, can be used to estimated the efficiency of the process by the formulas:

$$E = 1 - \frac{\tau_{DA}}{\tau_D} \tag{1.13}$$

$$E = 1 - \frac{F_{DA}}{F_D} \tag{1.14}$$

# Chapter 2

# Synthesis of Fluorescent Organic Nanoparticles (FONs)

## 2.1 Introduction

During the last years different strategies have been suggested for the synthesis of organic nanoparticles. Versatile methods involving emulsification and dessolvation [52, 53], or even more sophisticated technologies, including spray-drying [54], piezo-electrical ways [55], have been developed. These synthetic methods are mainly related to the preparation of bioorganic nanoparticles, to associate bio-macromolecules with different functionalities, for drug delivering or other bioapplications. For instance dessolvation, is usually proposed for the production of nanoparticles of different types of proteins [56]. Therefore, the choice of the synthetic route is central to optimize the final properties of nanoparticles designed for a specific application.

In this chapter we discuss a rapid and facile way to prepare fluorescent nanoparticles (**FONs**) from organic chromophores, named reprecipitation method. Nanoparticles have optical properties that are sensitive to size, shape, concentration, agglomeration. Hence, a number of parameters can affect their photophysical characteristics, during the preparation process. Their morphology and colloidal stability are additional factors that should be taken into account.

Another essential issue of the method is the choice of the chromophore. The molecular structure of a dye has a vital role on the way the molecules arrange during the nanoparticle formation and has significant influence on their optical response. Emission properties are particularly sensitive to these phenomena. Most of aromatic hydrocarbons and their derivatives are fluorescent in solution. Although, when their molecular concentration increases, luminescence is weakened, or even quenched, a phenomenon widely known as concentration quenching, or refereed to as Aggregation caused Quenching (**ACQ**). A main cause for the quenching process is the packing interactions. Typicaly, ACQ arises from $\pi$-$\pi$ interactions in fluorophores where aromatic rings comprised on a planar way (e.g. coumarin, perylene, rhodamines) when molecules aggregate, or from intermolecular hydrogen bonding between neighbouring fluorophores [48].

Alternative to ACQ, which often is detrimental for a number of applications, a number of luminophores exhibit high luminescence in high concentrated solutions,a process referred to as Aggregation-induced Emission (**AIE**) [57, 58]. Yuning et al. reported a series of silole derivatives that were non-emissive in dilute solutions, but became highly luminescent when their molecules were aggregated after drop-casting to form solid films [59]. AIE is found typically in non planar molecules, often with propeller-like shape, i.e. molecules that cannot pack through a $\pi - \pi$ stacking process, while the intramolecular rotations are restricted. Hence, this restriction of intramolecular rotations (**RIR**) blocks the non-radiative pathway and opens up the radiative way to annihilate the excited state. Up to now a lot of effort has been put to produce materials with AIE. Molecular design, including the design and the synthesis of the molecule, often functionalized with bulky units, or engineering approaches, including additives to control the intermolecular interactions, are some of the strategies reported in order to hinder fluorescence quenching.

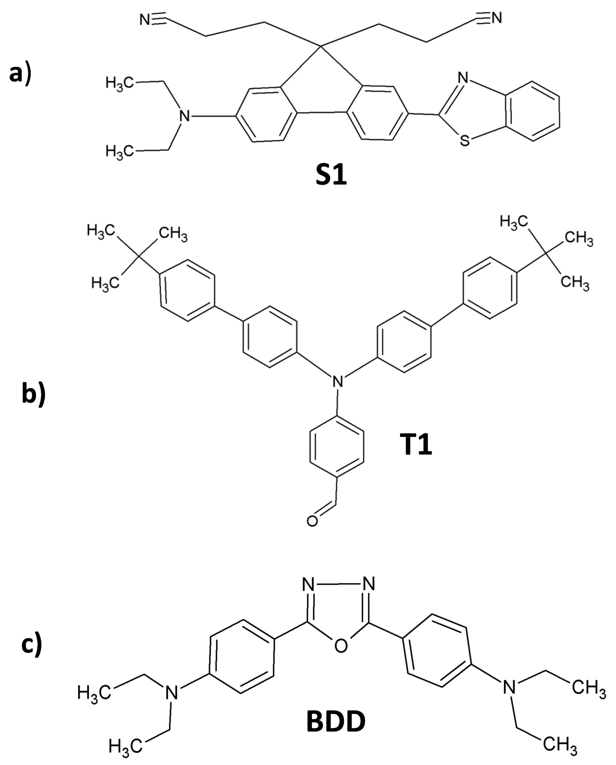

Figure 2.1: Molecular structures of the compounds investigated in this chapter. a) Fluorene derivative **S1**; b) Triphenylamine derivative **T1**; c) Oxadiazole derivative **BDD**

From that point of view, in this chapter we focus on the study of a number of aspects that can affect and modify the synthetic process, concerning the chemical composition of the starting material, the influence of concentration and the solvent effects.

In particular, the three compounds that are used as starting materials are:

- A Fluorene derivative (**S1** in fig. 2.1)
- A Triphenylamine derivative (**T1** in fig. 2.1)
- An Oxadiazole derivative (Commercially available) (**BDD** in fig.2.1)

All these molecules are characterised by electron donor (D) and electron acceptor (A) moieties, responsible intramolecular charge transfer (**ICT**).

## 2.2 Reprecipitation Method

The reprecipitation method is a simple and versatile way to prepare a suspension. The method was firstly reported in growing of organic crystals by Nakanishi et al. [60]. In a brief description, the preparation of NPs can be carried out by dissolving an hydrophobic compound in a hydrophilic organic solvent, and then few drops of this stock solution are introduced in an excess of water (working as an anti-solvent), under vigorous stirring. The disparity of solubility of the compound in the two solvents and the great miscibility between them are crucial for the method. During the mixing of stock solution in water, the micro-environment of the molecules changes abruptly. Hydrophobic forces induce the nucleation and the molecules tend to aggregate.

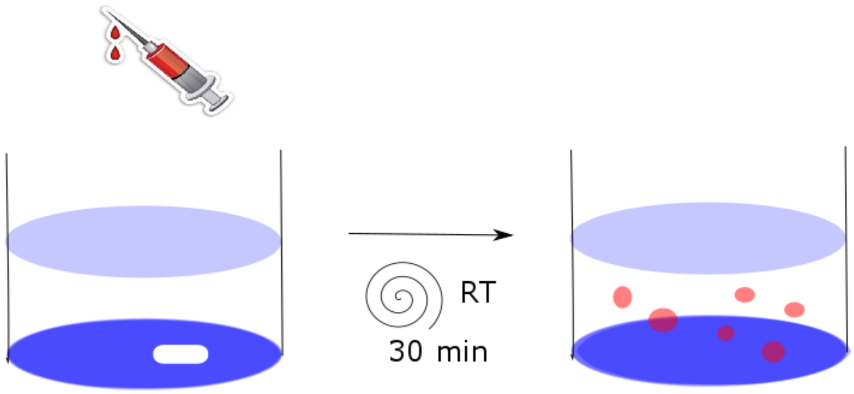

Figure 2.2: The standard reprecipitation method. The stock solution is injected with a syringe in water, under vigorous stirring. At the end of precipitation, a transparent suspension is obtained.

The method has been applied for different organic compounds such as $\pi$- conjugated, NLO dyes [61], fluorescent dyes, fullerene [62] or several polymers [63]. The choice of the solvent/antisolvent is critical and depends upon the purpose of the application. In this work, water has been chosen as antisolvent, aiming at bioapplications. As "solvent", hydrophilic solvents, like small-chain alcohols, acetone, acetonitrile or tetrahydrofuran (THF), can be used since they are miscible with water.

## 2.3 Fluorene-based FONs

Organic dyes based on fluorene and its derivatives generally exhibit high luminescence quantum yields, high photostability, excellent thermal stability and large values of two-photon absorption cross section. Hence, fluorene derivatives [64] have been extensively used in photonic applications, like electroluminescent devices [65], photodynamic therapy [66], fluorescent labelling and so on [67]. Therefore, a fluorene-dye with interesting photophysical properties was selected to begin our study and acquire confidence with the reprecipitation method.

**S1** is an unsymmetrical D-A-R substituted fluorene compound, where D is the diethylamino group acting as a electron-donating unit, R is the benzothiazole unit and A is the fluorene core [68] acting as acceptor. Its molecular structure is presented in fig. 2.1a.

**Preparation of FONs** For the preparation of nanoparticles the standard repricipitation method was followed, as described in the previous section. Tetrahydrofuran (THF) was chosen as organic solvent, considering the miscibility with water and compound solubility. A stock solution of concentration $C = 10^{-3}$M was prepared and few $\mu$L were injected in MilliQ water, under vigorous stirring, at room temperature. The final nominal concentration of the dye in suspension was $C = 10^{-5}$M. Reprecipitation is allowed for 30 minutes, before the characterization measurements.

**Spectroscopic Characterization** When the reprecipitation is achieved and nanoparticles are formed, the suspension appears transparent to the naked eye. The photophysical properties were studied via **UV-Vis** and **Fluorescence** spectroscopy. **UV-Vis** absorption spectra were recorded on a Perkin Elmer Lambda 650 spectrometer. **Steady-state** and **Time-resolved fluorescence** measurements were carried out on a Horiba Jobin Yvon Fluoromax-3 spectrofluorometer. **Fluorescence decays** were measured in a **TCSPC** (time-correlated single-photon counting) configuration, under excitation from 405 nm nanoLED. For comparison, spectroscopic data of the dye in THF were collected and are provided in figures 2.3, 2.4 and on table 2.1. The fluorescence quantum yields were estimated using fluorescein as reference. Fluorescence decays were fitted with exponential functions and the quality of the fits was judged by the reduced $\chi^2$ value ($\chi^2 < 1.1$). The average diameter of nanoparticles and their size distribution were defined through Dynamic Light Scattering (**DLS**).

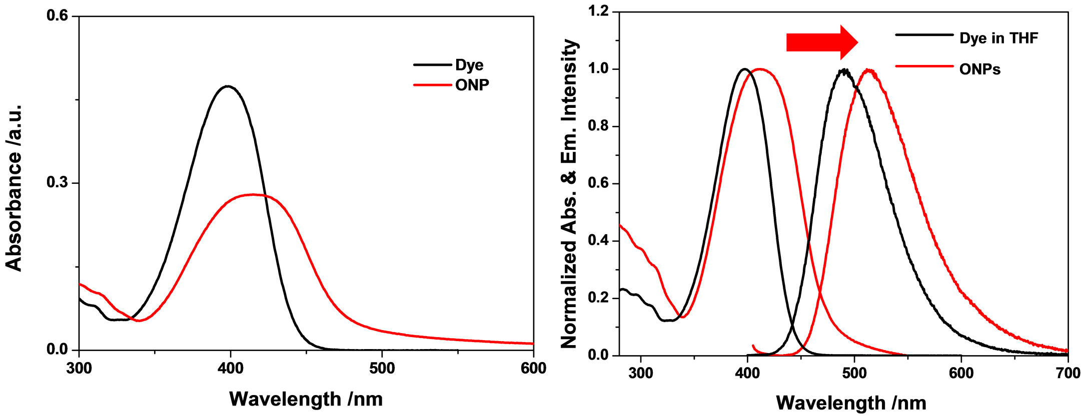

Figure 2.3: (left) UV-Vis spectra of **S1** fresh prepared FONs and solution in THF ($C = 10^{-5}$M). (right) Normalized UV-Vis and fluorescence spectra of **S1**, in THF and fresh prepared ONPs

The UV-Vis absorption spectra of FONs based on **S1** show one broad band with maximum at 416 nm. This band has a hypochromic effect compared to the dye dissolved in THF, the molar extinction coefficient ($\epsilon$) on the maximum being reduced by

41%. Moreover, this band presents a broadening and a red shift with respect to the dye in solution. Concerning the emission properties, the dye in THF shows a fluorescence peak at 501 nm, while it is shifted to the red upon nanoaggregation with a maximum at 514 nm. This shift to lower energy is consistent with the formation of J-aggregates.

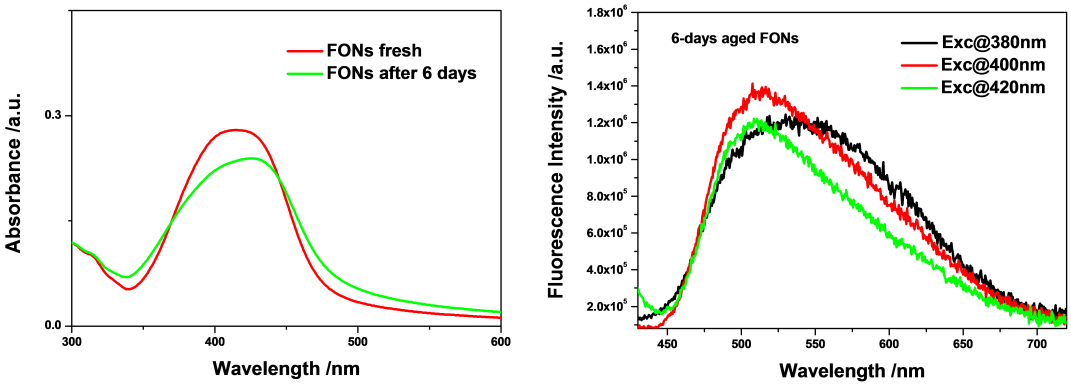

Figure 2.4: (left) UV-Vis spectra of freshly prepared FONs and 6-days aged. (right) Fluorescence spectra of **S1** FONs 6-days aged for different excitation wavelength.

Table 2.1: Spectroscopic Characteristics of **S1** in THF and FONs.

| Sample | $\lambda_{Abs}$ max (nm) | $\lambda_{Em}$ max (nm) | Stokes Shift $(cm^{-1})$ | $\epsilon$ max $M^{-1}cm^{-1}$ | $\Phi$ [a] % | $\tau_1$ (nsec) [b] | $\tau_2$ (nsec) | $\tau_3$ (nsec) |
|---|---|---|---|---|---|---|---|---|
| **THF** | 397 | 501 | 5228 | 47418 | 0.86 | 1.6 | - | - |
| **FONs** | 416 | 514 | 4583 | 27964 | 0.10 | 0.44 (0.45) | 1.6 (0.45) | 6.2 (0.1) |

[a] Fluorescence quantum yield was estimated through the comparative method, using fluorescein as a reference. ($\Phi = 0.9$)

[b] Fluorescence decays fitted with exponential function (mono-exponential for the dye and three-exponential for ONPs). In parenthesis is the relative contribution in total decay.

The fluorescence quantum yield of FONs was estimated to amount to 10%. This value is significant lower than that of dye in THF (86%), or in other solvents as reported in literature [68]. Consequently, **S1** molecules pose Aggregation-caused Quenching (**ACQ**) phenomena probably due to stacking interactions among the aromatic rings. The lifetime decay of the compound in THF was fitted with a mono-exponential function, instead for nanoparticles a three-exponential function was needed, suggesting a strong heterogeneity.

Another point that deserves attention is the colloidal stability of the system. Absorption and emission spectra of FONs were recorded after six days. From spectroscopic data in fig. 2.5, in UV-vis spectrum of 6-days aged FONs, the main absorption band presents a further hypochromic effect, this can be ascribed to a possible re-organization of aggregates in suspension. This re-organization can lead to a further aggregation or agglomeration, and these new species have different optical behaviour. This evidence can be confirmed by fluorescence results in fig.2.4, where emission spectra are dissimilar for different excitation energies.

Finally DLS measurement provide us information on average diameter of ONPs and their size distribution in suspension. For freshly prepared FONs the effective diameter is $\sim$ 160 nm and the polydispersity index (PDI) is 0.052.

## 2.4 Triphenylamine-based FONs

The second chomophore that was studied is a dipolar triphenylamine-based molecule named **T1** and its molecular stracture is illustrated in fig 2.1b. Depending upon the core and functionalization of the peripheral units, triphenylamine derivatives are found in many materials for 2PA applications. Ishow et al. are reporting in ref. [69] the photophysical properties of a serie of Triphenylamine push-pull compounds with different substituents, where solid-state emission is tuned by the strength of ICT, while their absorption band and main structural backbone remain unchanged. The **T1** chromophore is constituted by the electron-donating (D) triphenylamino core and by an aldehyde as electron acceptor (A). Bulky substitutents are attached to two of the three branches, in order to avoid the stacking and obtain stable and highly luminescent nanoparticles.

From this perspective, **T1** compound was selected for the preparation of two series of samples, where a couple of parameters were examined during the reprecipitation process. The first tested parameter is the final nominal concentration of the chromophore in suspension, and the second one is the proportion between solvent and anti-solvent during the preparation.

Firstly, the optical characterization of the dye dissolved in solvents of different polarity has been performed. The absorption solvatochromic behaviour has been evaluated and the fluorescence characteristics (quantum yield, lifetime) have been estimated. The photophysical characteristics are provided in table 2.2. All Uv-vis absorption and fluorescence spectra in organic solvents with different polarity are displayed in fig. 2.5.

Table 2.2: Spectroscopic Characteristics of **T1** Dye in solvents of different polarity.

| Solvent | $\lambda_{Abs}$ max (nm) | $\lambda_{Em}$ max (nm) | $\Phi$ [a] % | $\tau_1$[b] (nsec) | $\tau_2$ (nsec) |
|---|---|---|---|---|---|
| **Toluene** | 336 | 472 | 39 | 1.3<br>(17.7) | 4.2<br>(82.34) |
| **Chloroform** | 336 | 553 | 11 | 0.1<br>(3.6) | 2.4<br>(96.36) |
| **DCM** | 340 | 557 | 8.4 | 1.1<br>(8.9) | 2.1<br>(91.15) |
| **THF** | 336 | 505 | 12.7 | 0.7<br>(3.89) | 4.1<br>(96.11) |
| **ACN** | 339 | 581 | 1.2 | 0.4<br>(97.90) | 3.1<br>(2.10) |
| **DMSO** | 340 | 581 | 1.9 | 0.4<br>(96.89) | 3.6<br>(3.11) |

[a] Fluorescence quantum yield was estimated through the comparative method, using fluorescein as a reference. ($\Phi = 0.9$, NaOH 0.1M)

[b] Lifetimes decays were fitted with bi-exponential functions. In parenthesis is the relative contribution in total decay.

Two peaks appear in absorption spectra: one located in the ultraviolet spectral region ($\sim$ 335 nm) and the second with a maximum at 365 nm extending to the visible region. No significant solvatochromic behaviour is observed in absorption. The situation is different in fluorescence spectra, where the emission band shifts to the red increasing the solvent polarity. This red shift is accompanied by a fluorescence quenching for highly polar solvents (Acetonitrile, DMSO). The quantum yield of the dye is reduced from 39% in toluene (the less polar solvent) to less than 2% in acetonitrile and DMSO.

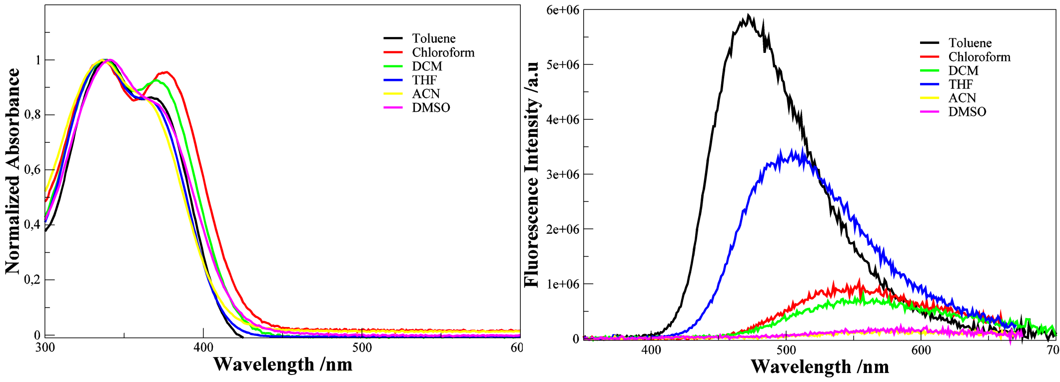

Figure 2.5: **T1** dye in solvents of different polarity. (left) UV-vis absorption spectra and (right) fluorescence spectra normalized with respect to absorbance.

For the preparation of FONs, the standard method was followed, as for **S1**. Tetrahydrofuran (THF) was chosen as organic solvent and a solution of **T1** compound, in concentration $C = 10^{-3}$M was prepared. Then few $\mu$L were injected in purified water, under vigorous stirring. The final nominal concentration of the dye in suspension was $C = 10^{-5}$M. In fig. 2.6 the absorption and emission spectra of nanoparticles are reported and compared to dye dissolved in THF.

The UV-vis absorption spectrum of FONs based on **T1** displays two peaks: the first one has maximum at 338 nm and the second at 390 nm, shifted more to the red, with respect to the dye in THF. Consistently with results for the fluorene derivative, the UV-vis bands display a broadening and an hypochromic affect, with a reduction of molar extinction coefficient ($\epsilon$). Fluorescence of FONs is located in spectral region similar to the dye dissolved in THF. The detailed spectroscopic behaviour and the photophysical characteristics of suspensions are analysed further in next experimental subsections.

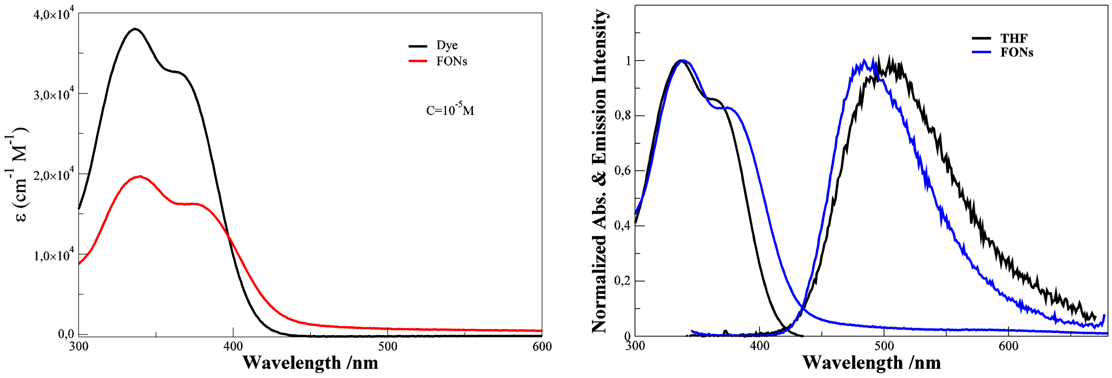

Figure 2.6: (left) Molar extinction coefficient of **T1** dye and FONs ($C = 10^{-5}$M). (right) Normalized UV-Vis and fluorescence spectra of **T1** in THF and fresh prepared FONs.

### 2.4.1 Concentration Effects

In order to understand the influence of concentration and to define the most favourable conditions for our purpose, an analytical study on repreciptation process have been done, concerning the optimization of the preparation method [70]. A series of suspensions have been prepared, in various concentration of **T1** compound and their optical properties have been examined.

**Preparation of ONPs** For the fabrication of nanoparticles, the standard method was followed, altering each time the amount of the initial solution injected in water. Particularly, Tetrahydrofuran (THF) was chosen as organic solvent, considering its good miscibility with water and the compound solubility. A stock solution in concentration $C = 10^{-3}$M was prepared and different amounts of this solution were inserted in MilliQ water under vigorous stirring. The final concentration of the dye in suspension and the mixing ratio of stock solution (solvent) and MilliQ water (antisolvent), are reported in table 2.3.

Table 2.3: Nominal dye concentration in suspension and water/THF ratio

| Concentration | $H_2O$:THF |
|---|---|
| $10^{-5}$ M | 99:1 |
| 2x$10^{-5}$ M | 98:2 |
| 5x$10^{-5}$ M | 95:5 |
| $10^{-4}$ M | 90:10 |
| 2x$10^{-4}$ M | 80:20 |
| 5x$10^{-4}$ M | 50:50 |

The stirring is allowed for 30 minutes and then the suspension is allowed to rest for at least 30 minutes. .

**Spectroscopic characterization of FONs** UV-vis and steady state fluorescence spectra have been recorded for all samples at room temperature. All spectroscopic characteristics are collected and provided in table 2.4 and in fig.2.7. Increasing the concentration, UV-vis spectra display an increase of the relative intensity of the CT band (extended in visible region), with respect to band at 338 nm (UV region)

In fluorescence spectra a slight red-shift is obtained while the concentration of the dye is increased. The fluorescence quantum yield progressively decreases with the concentration of the dye, with a reduction of 90% for one order of magnitude increase in the concentration of the compound. Hence, it is possible to conclude that a nominal concentration of the dye in suspension $\leq 10^{-5}$ M is necessary to avoid strong quenching phenomena of fluorescence.

The lifetime decays were measured, using as an excitation source, a single- wavelength Nanoled at 374 nm. To fit the experimental decays a three exponential deconvolution analysis was applied. The origin of three lifetimes decays can be ascribed to the het-

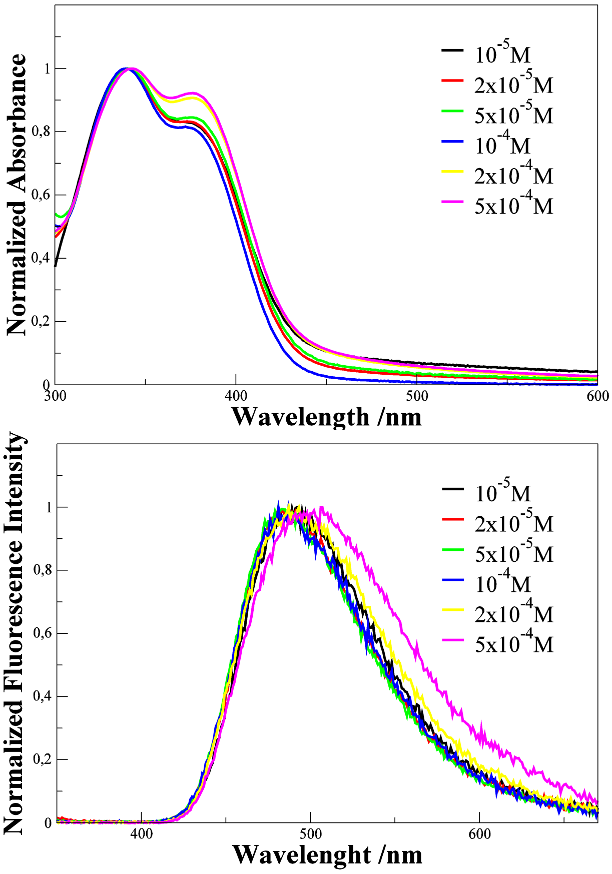

Figure 2.7: (top) Normalised UV-vis spectra and (bottom) fluorescence spectra of **T1** FONs in different nominal concentration.

erogeneity of the nanosystem, ascribed to nanoparticles of different size, with different lifetimes of radiative emission. In chapter 4 we discuss in detail an alternative fitting analysis, with a stretched exponential function, particularly suited for heterogeneous samples.

### 2.4.2 Solvent/Antisolvent Proportion

**Preparation of FONs** The second parameter investigated is the proportion blending of solvent (THF) and antisolvent (water). In this case, the standard recrecipitation method was used, but a number of initial solutions have been prepared, to reach the final concentration of the dye in each suspension of $10^{-5}$M, independently of the mixing ratio of solvents. The proportion among solvents and the concentration of starting

Table 2.4: Spectroscopic Characteristics of ONPs in various nominal concentration **T1**.

| Sample | $\lambda_{Abs}$ *max* (nm) | $\lambda_{Em}$ *max* (nm) | $\Phi$ [a] % | $\tau_1$ [b] (nsec) | $\tau_2$ (nsec) | $\tau_2$ (nsec) |
|---|---|---|---|---|---|---|
| $10^{-5}$ M | 340/377 | 490 | 6.2 | 2.8<br>(47.58) | 0.7<br>(17.34) | 6.4<br>(35.02) |
| 2x$10^{-5}$ M | 340/377 | 488 | 7.4 | 1.9<br>(47.84) | 0.5<br>(18.46) | 5.0<br>(33.70) |
| 5x$10^{-5}$ M | 340/378 | 485 | 3.2 | 2.2<br>(50.96) | 0.6<br>(20.75) | 5.4<br>(28.29) |
| $10^{-4}$ M | 339/377 | 483 | 0.9 | 2.1<br>(47.06) | 0.5<br>(13.08) | 5.2<br>(39.86) |
| 2x$10^{-4}$ M | 342/378 | 492 | 0.7 | 1.6<br>(36.44) | 0.2<br>(7.97) | 4.0<br>(55.59) |
| 5x$10^{-4}$ M | 342/378 | 505 | 0.7 | 1.3<br>(39.17) | 0.2<br>(12.50) | 3.0<br>(48.34) |

[a] Fluorescence quantum yield was estimated through the comparative method, using fluorescein as a reference. ($\Phi = 0.9$, NaOH 0.1M)

[b] Lifetimes decays were fitted with three exponential functions. In parenthesis is the relative contribution in total decay.

solution are provided in table 2.5.

The first information is obtained with naked eye: the ratio between THF and water affects the macroscopic picture of suspension. When water is dominant (water/THF 99:1), the suspension is transparent. As the THF is increasing, the suspension becomes turbid and the most cloudy sample is the 80:20. Indeed, turbidity did not allowed UV-vis spectrum to be recorded. Further, increasing THF respect to water, the suspension becomes again transparent (60:40, 50:50). In other words, there is an unusual miscibility gap of THF-Water, a transition from a miscible regime to an immiscible regime, and then back to another miscible regime. [71].

Table 2.5: Proportion among solvents and concentration of initial solution for the preparation of each sample

| Water:THF | Concentration initial sol. |
|---|---|
| 50:50 | $2x10^{-5}$M |
| 60:40 | $2.5x10^{-5}$M |
| 70:30 | $3.3x10^{-5}$M |
| 80:20 | $5x10^{-5}$M |
| 90:10 | $10^{-4}$M |
| 99:1 | $10^{-3}$M |

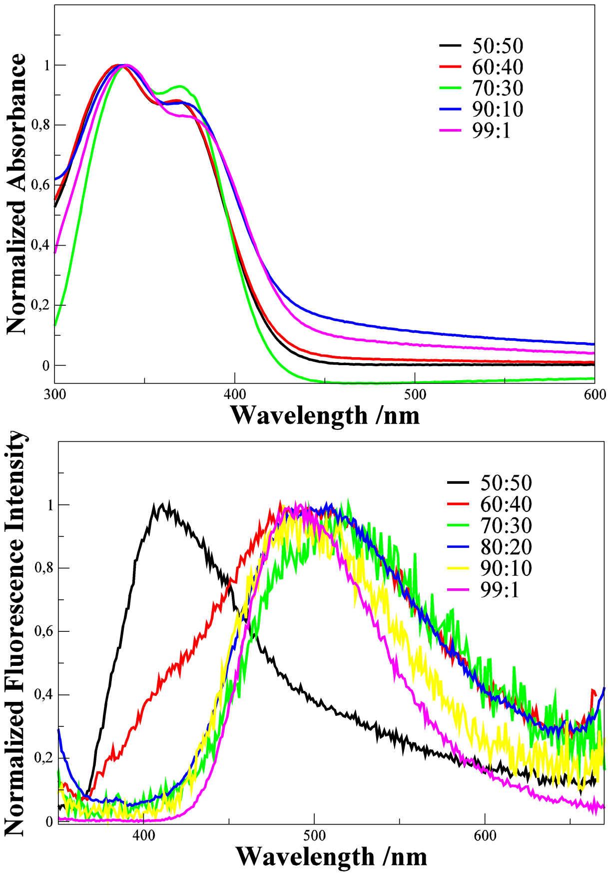

Figure 2.8: (top) Normalised UV-vis spectra and (bottom) fluorescence spectra of **T1** suspension in various proportions water-THF.

Table 2.6: Spectroscopic Characteristics of **T1** FONs in various proportion water-THF.

| Sample | $\lambda_{Abs}$ max (nm) | $\lambda_{Em}$ max (nm) | $\Phi$ [a] % | $\tau_1$ [b] (nsec) | $\tau_2$ (nsec) | $\tau_3$ (nsec) |
|---|---|---|---|---|---|---|
| 50 : 50 | 336/368 | 415 | 0.7 | 1.5<br>(58.86) | 0.2<br>(8.68) | 2.4<br>(32.46) |
| 60 : 40 | 336/368 | 495 | 0.6 | 0.2<br>(31.21) | 0.7<br>(54.70) | 2.1<br>(14.90) |
| 70 : 30 | 340/370 | 510 | 2.4 | 0.1<br>(41.46) | 0.3<br>(56.24) | 1.8<br>(2.30) |
| 80 : 20 | – | 498 | – | 0.1<br>(58.32) | 0.3<br>(41.68) | – |
| 90 : 10 | 339/374 | 490 | 2.5 | 0.2<br>(39.45) | 0.8<br>(43.46) | 2.3<br>(17.09) |
| 99 : 1 | 340/377 | 490 | 6.2 | 2.8<br>(47.58) | 0.7<br>(17.34) | 6.4<br>(35.07) |

[a] Fluorescence quantum yield was estimated through the comparative method, using fluorescein as a reference. ($\Phi = 0.9$, NaOH 0.1M)

[b] Lifetimes decays were fitted with multi-exponential functions. In parenthesis is the relative contribution in total decay.

**Spectroscopic characterization of FONs** UV-vis and steady state fluorescence spectra have been recorded for all samples at room temperature. All spectroscopic characteristics are reported in table 2.6 and in fig.2.8. In the UV-vis spectra the unusual behaviour of the binary system THF-water affects the conditions of measurements. For turbid samples it was not possible to obtain a good baseline. Hence, the estimation error of quantum yield is higher for these samples. No significant changes were observed in UV-Vis spectra of samples in terms of energy and intensity of absorption bands.

The fluorescence band of most of samples is located around ~500 nm, with the exception of the 50:50 sample, whose emission band appears shifted to the blue, at 415 nm. This blue shift can be ascribed to different aggregations when water and THF molecules are statisticaly equal in suspension, suggesting a trapped exciton whose relaxation is hindered or the formation of H-aggregates. Modifying the proportion among solvents, also leads to weakening of fluorescence. The quantum is reduced by 90%, from 99:1 sample to 50:50 sample. The lifetime decays were measured, using as an excitation source, a single wavelength Nanoled emitting at 374 nm. The results are analysed with three exponential functions.

## 2.5 Oxadiazole Derivative

The third chromophore that was studied, is a commercially available Oxadiazole derivative (fig. 2.1c). 2,5-Bis(4-(diethylamino)phenyl)-1,3,4-oxadiazole (BDD) is a recognized important laser dye for the blue-green spectral region and there are a number of references on its photochemical and photophysical properties [72]. Further, BDD finds application in electronic devices as charge transfer layers (CTLs) or photoconductors [73].

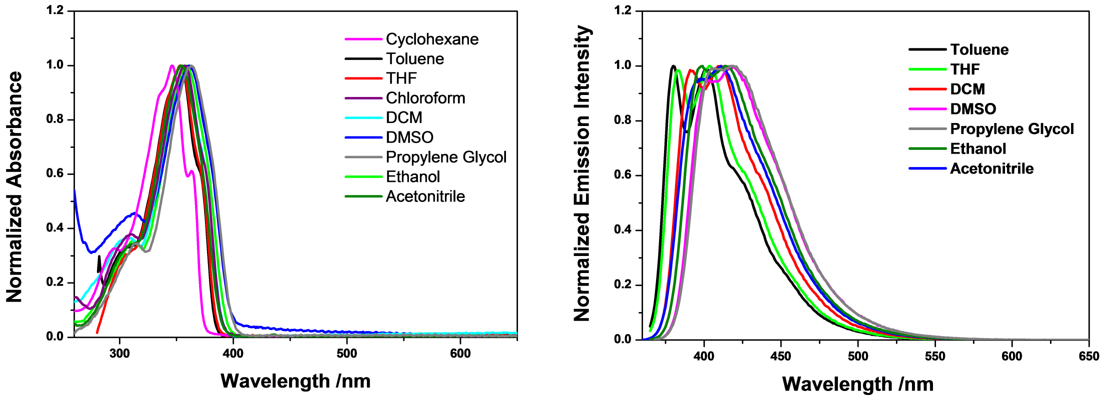

Figure 2.9: (left) Normalised UV-vis spectra (right) fluorescence spectra of **BDD** dye in solvent of different polarity.

A spectroscopic characterization of the dye in solvents of different polarity has been performed. UV-Vis and fluorescence spectra and the spectroscopic characteristics are reported in fig. 2.9 and in table 2.7.

Table 2.7: Spectroscopic Characteristics of **BDD** dye in solvents of different polarity.

| Solvent | $\lambda_{Abs}$ max (nm) | $\lambda_{Em}$ max (nm) | Stokes Shift $(cm^{-1})$ | $\epsilon$ $M^{-1}cm^{-1}$ | $\Phi$ [a] % | $\tau$ [b] (ns) |
|---|---|---|---|---|---|---|
| **Cyclohexane** | 346 | - | - | - | - | - |
| **Toluene** | 354 | 401 | 3310 | - | 8.0 | 1 |
| **Chloroform** | 357 | - | - | - | - | - |
| **DCM** | 357 | 410 | 3620 | 48570 | 8.8 | 1.1 |
| **THF** | 354 | 404 | 3496 | 48600 | 8.3 | 1.1 |
| **ACN** | 354 | 410 | 3858 | 47610 | 9.3 | 1.2 |
| **DMSO** | 361 | 418 | 3777 | - | 8.5 | 1.2 |
| **Ethanol** | 358 | 415 | 3836 | - | 9.3 | 1.2 |
| **Propylene Glycol** | 362 | 418 | 3700 | - | 9. | 1.3 |

[a] Fluorescence quantum yield was estimated through the comparative method, using fluorescein as a reference. ($\Phi = 0.9$, NaOH 0.1M)

[b] Lifetimes decays were fitted with an exponential function. In parenthesis is the relative contribution in total decay.

Spectroscopy results indicate not intense but significant solvatochromic behaviour both in absorption and emission spectra. In particular a slight red shift is observed obtained when solvent polarity increases. Fluorescence quantum yield was estimated to amount to $8\%$ for less polar solvents, while reaches $10\%$ for highly polar and viscous solvents (DMSO, Propylene Glycol). For Cyclohexane and Chloroform data are not reported data, since samples were not photostable enough. Fluorescence lifetimes decays were fitted by a mono-exponential function.

For the preparation of nanoparticles the standard reprecipitation method was followed, but even after a couple of efforts nanoparticles were not formed. A possible explanation could be that the compound is not fully insoluble in water.

## 2.6 Conclusions

To summarise, in this chapter we presented the preliminary results of the preparation method, named reprecipitation, of fluorescent organic nanoparticles (FONs). Aim of the experimental work was to obtain a fundamental experience on the synthetic routine, on characterization techniques and optimize a number of parameters in the preparation process. Three chromophores with different molecular structure were selected to be studied. Two series of FONs based on a triphenylamine derivative were studied in terms of concentration and proportion of water-THF.

From the experimental results, it is possible to conclude that aggregation has strong effects on the optical properties. Aggregation often results in quenching of fluorescence of a fluorophore, particularly when $\pi$-$\pi$ stacking is not hindered.

Not only the molecular geometry and the way of packing within the particles is important, but also the concentration should be taken into account. We found that the final nominal concentration of the dye in suspension modifies the optical properties, the optimal final concentration of the chromophore in suspension being $\leq 10^{-5}$ M in order to present some fluorescence.

The choice of the solvent and the solvent/antisolvent ratio are critical. The molecule should be soluble in the organic solvent and insoluble in water. Moreover, the miscibility between the solvents has its own influence. A miscibility gap for THF and water was found. The increase of THF in suspension and decreasing the water, result to a progressive weakening of fluorescence of FONs and the optimal proportion is 99:1 water:THF.

Even, if these parameters were optimized, there are numerous other factors that should be taken into account. It is impossible to have a general rule that guarantees to obtain highly fluorescent and stable nanoparticles, or dyes with similar structure result to nanoparticles with similar optical and colloidal behaviour. From empirical point of view, it seems that molecules functionalized with bulky groups tend to give more stable and highly fluorescent nanoparticles. For instance the triphenylamine-based suspension is more stable during time, than the fluorene-based one.

# Chapter 3

# Organic Nanoparticles for Energy Transfer

## 3.1 Introduction

Multifunctional systems have attracted wide interest in bioimaging during the last years [74,75]. The complexity of biological systems and the lack, frequently, of materials with peculiar optical and mechanical properties, call for novel structures in micro and nanoscale, that can allow better resolution and improve the penetration depth in live tissues [76,77]. As already discussed in the introduction, one of the most important issues in fluorescence microscopy applications is the spectral region of absorption and emission of a fluorophore, and its linear and non-linear response in the transparency window of biological tissues. Another important point is the biocompatibility between the compound and the living cell or tissue, specially for *in-vivo* observations [78, 79].

For these purpose, up to now, different structures of inorganic, organic or hybrid materials have been developed. Luminescent quantum dots (**LQD**) [80, 81], graphene quantum dots (**GQD**) [82], incorporated dyes in **Silica** nanoparticles [83] or carbon nanotubes (**CNT**) functionalised with dyes are some of the innovative materials, that have attracted the attention recently in this field. Although, still there are important defects, that are detremental for living organisms. For instance, the bleaching or the chemical degradation of a luminophore can often be toxic and significantly perturb or even kill cells. [84, 85].

As an alternative, in this chapter we propose the preparation of fully organic multicomponent nanoparticles in water [86], where energy transfer phenomena are exploited. Particularly, a cascade energy transfer between different molecular components is suggested, with tunable emissive properties and a strong non-linear optical response, in the transparency window of living cells [87–89]. The development of controlled cascade energy transfer (**EET** cascade) among three chromophores, generates an enhanced emission in the red spectral region. The two-photon brightness of these nanoparticles is greatly enhanced, with respect to that of the single-component nanoparticles. Thanks to this property, together with the good colloidal stability in water suspension, these fully organic multicomponent trenary nanoassemblies are promising nanoprobes for application in Two-Photon Microscopy.

## 3.2 Multicomponent Fluorescent Organic Nanoparticles

Two types of multicomponent fluorescent nanoparticles (FONs) have been fabricated, by one-step and by multi-step reprecipitation method. The latter is addopted for the preparation of ternary **Core@Shell@Shell**, nanoparticles, where the three dyes are organized in the nanoparticle "layer by layer", with a core and two shells (internal and external). In the second type, named **Composite** nanoparticles, the three compounds are randomly distributed in the total volume of each nanoparticle.

The colloidal stability and the optical properties were examined, in the absence and in the presence of a polymeric stabilizer, namely Poly-methyl methacrylate (**PMMA**) A completely morphologic and spectroscopic characterization have been performed. Absorption and fluorescence characteristics have been recorded by the same instrumentation reported in chapter 2. The size and the morphology have been defined via **Dynamic Light Scattering (DLS)** and **Transmission Electron Microscopy (TEM)**. In addition, the temporal evolution of these characteristics has been investigated.

Supplementary, the non linear response of ternary nanoparticles was been measured by **Two-Photon Excited Fluorescence (TPEF)**. FONs have been two-photon excited over broad spectral range (from **600** to **1200 nm**) in the biological transparency window. The experimental details and the instrument setup for TPEF measurements are reported in Appendix 1.

### 3.2.1 Dyes for Energy Transfer: Triphenylamine derivatives

Three triphenylamine-based "push-pull" aromatic compounds have been carefully chosen, according to their spectral range of absorption and emission. The structures of these dyes are provided in fig.3.1 and for ease of reference, they are named **TW0**, **TW1**, **TW2** [90]. The scope of this selection is an efficient cascade energy transfer, to result in emission in spectral region of red irrespectivelly of the excitation wavelength. A sequential energy transfer between two Donor-Acceptor pairs (**TW0** and **TW1**, **TW1** and **TW2**) contributes to obtain an efficient and directional excitation energy-transfer cascade (fig.3.1). **TW0** is excited with a UV light and can act as energy donor to **TW1** which, in turn, can act as energy donor toward **TW2**, which finally emits red light.

A crucial criterion, in order EET to occurs, is the spectral overlap between fluorescence emission spectrum of the donor molecule and the absorption spectrum of the acceptor chromophore. In our case the three chromophores satisfy this requirement. In fig. 3.2 the overlap between the emission spectrum of **TW0** and the absorption spectrum of **TW1**, as well as between the fluorescence spectrum of **TW1** and the absorption spectrum of **TW2** is highlighted.

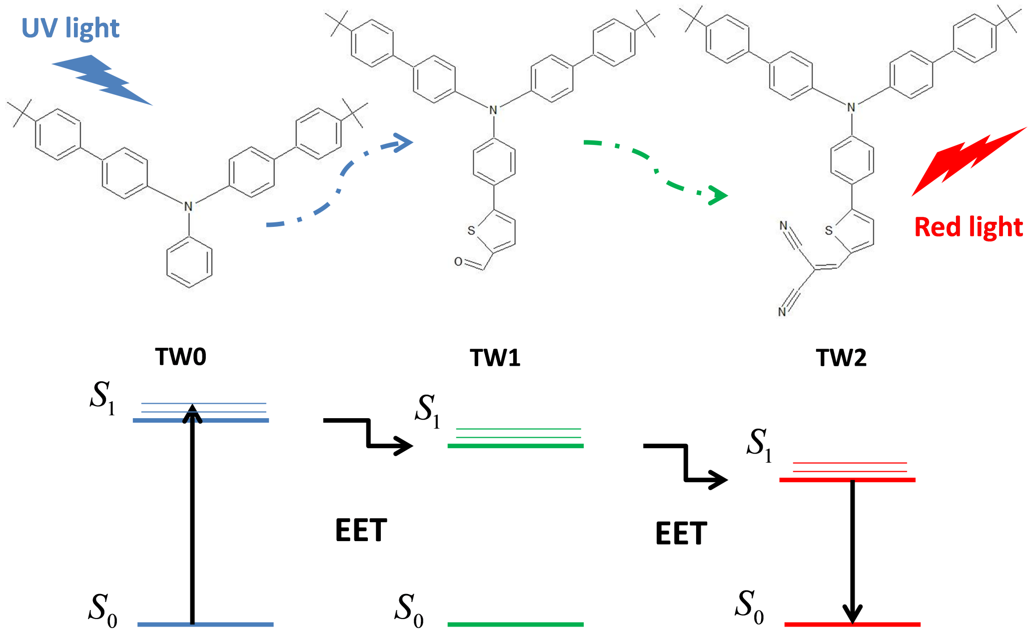

Figure 3.1: Chemical structures of triphenylamine derivatives **TW0** , **TW1** and **TW2** and the **EET** cascade scheme. **TW0** is excited and non-radiatively transfers excitation energy to **TW1**. Then, **TW1** non-radiatevely transfers excitation energy to **TW2** which finally radiatively emits photons.

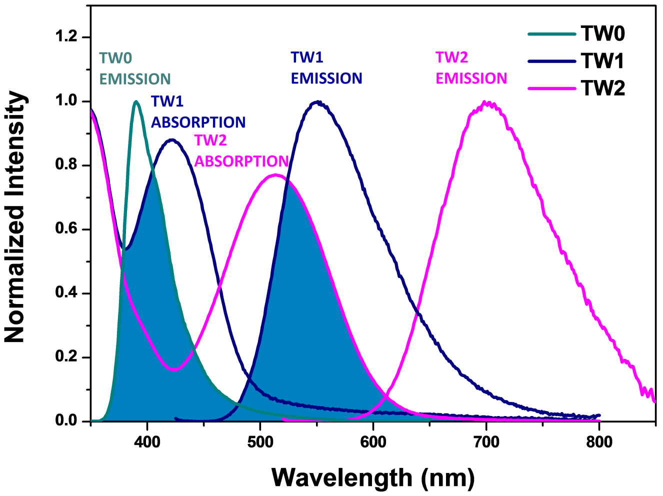

Figure 3.2: The spectral ovelap among **TW0** emission and **TW1** absorption, and between **TW1** emission and **TW2** absorption in THF. Exictation Energy Transfer 1:**TW0 -TW1** and Excitation Energy Transfer 2: **TW1-TW2**

In case of **Core@Shell@Shell** nanoparticles, **TW2** is used to compose the core of the nanoparticle, **TW1** to form the inner shell and **TW0** to compose the external shell (in contact with water). In this way, ternary **Core@Shell@Shell** nanoassemblies are obtained where efficient **EET** from external layer (shell) to internal (secondary shell) and finally to the core can occur. Additionally, **Composite** ternary nanoparticles were prepared, where the three different dyes are randomly mixed inside the nanoassemblies. The suggested structures of dyes dispersed in the volume of the particle are visualized in fig.3.3

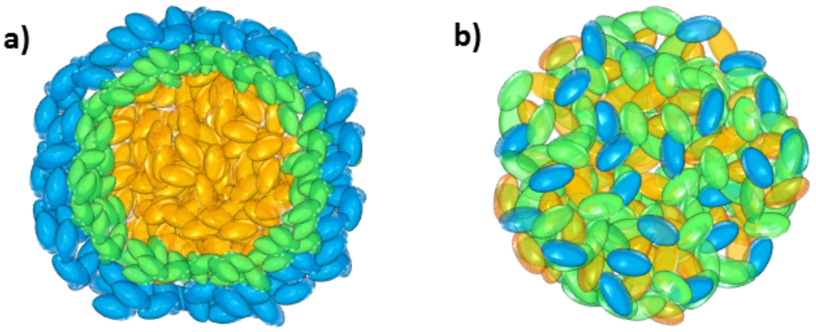

Figure 3.3: Suggested structures of trenary nano-assemblies: a) **Core@Shell@Shell FONs**; b) **Composite FONs**.

### 3.2.2 Reprecipitation method: One and multi-step process

For the formation of ternary FONs, two different versions of reprecipitation method were followed according to the sought final structure. Additionally, some of the nanoparticles were doped with **PMMA**, to test the effects on the colloidal stability. In summary, the types of FON, that we were prepared, are:

- **TW2@TW1@TW0** nanoparticles.

- **TW2@TW1@TW0** nanoparticles with **PMMA**.
- **Composites** nanoparticles.
- **Composites** nanoparticles with **PMMA** .

**Core@Shell@Shell** were prepared by a multistep reprecipitation method, instead **Composite** nanoparticles that were assembled in one step. In addition, monocomponent **TW0**, **TW1**, **TW2** and **TW0-PMMA**, **TW1-PMMA**, **TW2-PMMA** organic nanoparticles were prepared using the standard reprecipitation method, to correlate with multicomponent samples.

### Core@shell@shell Nanoparticles

The preparation of **Core@Shell@Shell** nanoparticles was achieved using a multistep reprecipitation process, extending the standard method in three sequential stages. The concept in this extension is a bottom-up approach, to built up the structure from core to shell, layer by layer. In this approach, no chemical reaction is taking place but the aggregation is driven by the hydrophobic reaction of the molecules in water. Firstly, **TW2** FONs (core) were prepared by addition of an aliquot of a concentrated THF solution of **TW2** in a large volume of ultrapure water under vigorous stirring. In a second step, an aliquot of a concentrated THF solution of **TW1** was added to the aqueous suspension of **TW2** FONs, in order to cover **TW2** FONs with a layer of **TW1**. Finally, an aliquot of a concentrated THF solution of **TW0** was added to the obtained **TW2@TW1** FONs suspension to create an outer layer of dye TW0. The final nominal concentration is $10^{-5}$ M for each of the three different dyes.

### Core@shell@shell Nanoparticles with PMMA

**Core@Shell@Shell** nanoparticles were obtained using the same starting compounds but, in this case, a small amount of the optically neutral polymer polymethylmetacrylate (**PMMA**) was added as a dopant into the nanoparticles. The process is similar to the previous one. **TW2** and **PMMA** solutions in THF were mixed together, and a small amount of this solution was added to a known large volume of ultrapure water. When **PMMA**-doped **TW2** nanoparticles are obtained, in this suspension an aliquot of a THF solution of **TW1** and **PMMA** was added, in order to obtain **PMMA**-doped **TW2@TW1** FONs. Finally, an aliquot of a THF solution of **TW0** and **PMMA** was added to the binary suspension, to give **TW2@TW1@TW0 PMMA**-doped nanostructures. The final nominal concentrations are : $10^{-5}$ M for each one of the three chromophores, and $3\text{x}10^{-7}$M for **PMMA**.

#### Composites nanoparticles

**Composite** nanoparticles were obtained via the standard reprecipitation method, in one step, by adding a small amount of a concentrated THF solution of the three chromophores, to a large amount of pure water under vigorous stirring. The final nominal concentration is $10^{-5}$ M for each one of the compounds.

#### Composites nanoparticles with PMMA

**PMMA**-doped **Composite** nanoparticles were obtained in one step by adding an aliquot of a stock solution of the three chromophores and PMMA to water. The final nominal concentrations are: $10^{-5}$ M for each one of the chromophores and $3\text{x}10^{-7}$ M for **PMMA**.

### 3.2.3 Morphological Characterization and Colloidal Stability

The morphologic characteristics and the agglomeration of FONs have been checked during time. The features of undoped and **PMMA**-doped FONs were compared, and the role of **PMMA** is significant in the colloidal stability of nanoparticles in water. The measurements have been performed for fresh suspensions and after 11 weeks.

The diameter and the morphology of nanoparticles were defined via **Transmission Electron Microscopy** (**TEM**) with a JEOL 2200FS analytical TEM equipped with in-column energy filter working at 200 kV. To enhance the contrast in image, a treatment of FONs with a staining agent was compulsory. All samples were stained with uranyl acetate (2$\%$ w/w in water). A droplet of the aqueous suspensions was placed on a carbon grid and the liquid excess was drawn off with paper. Then, the grids were allowed to dry for 1 day, before performing the measurement. A statistical analysis of particle size has been performed.

To confirm the average size of the aggregates and to identify the homogeneity of the particle size in water, **Dynamic Light Scattering** (**DLS**) and **Zeta-potential** analysis were performed [91]. The effective diameter and the polydispersity index were estimated. A size distribution analysis have been performed as well. The instrumentation for DLS measurements was a 90Plus Particle Size Analyzer digital autocorrelator (Brookhaven), with 635 nm laser at $\theta = 90^\circ$ and $25^\circ C$. Data were analysed using cumulant fit (CMFT) analysis. Zeta-potential analysis was performed using the same 90Plus instrument equipped with BI-PALS option.

**Results** The qualitative control of the suspensions through the naked eyes confirms that no big aggregates are formed, either in the fresh prepared suspensions or even after many weeks. In fact, no scattering is observed in absorption and fluorescence spectra, even for 11-week aged nananoparticles. The good colloidal stability is confirmed by the Zeta potential analysis, giving values lower than -30 mV for all the nanoparticles. All data of Zeta-potential and TEM analysis are given in table 3.1.

A first proof of the **Core@Shell@Shell** FONs formation is detectable from Zeta-potential results. Monocomposite **TW0** FONs and nanostructures obtained via the three-step reprecipitation process show very similar Zeta-potentials, slightly different, for example, from the Zeta-potential value measured for pure **TW2** FONs. This can be ascribed to the presence of **TW0** at the surface of **Core@Shell@Shell** nanoparticles.

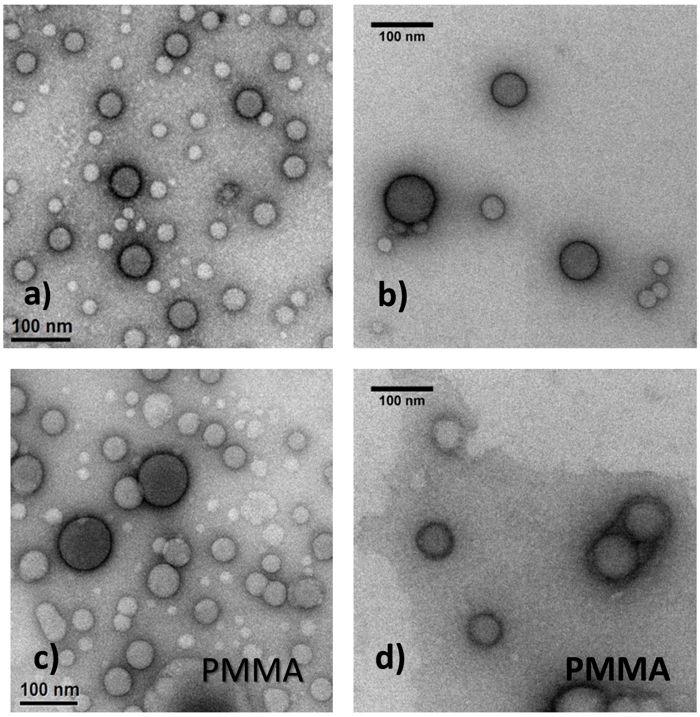

Figure 3.4: TEM images of free (top) and doped-**PMMA** (bottom) **Core@shell@shell FONs**, freshly prepared (left) and after 11 weeks (right).

**TEM** images of **Core@Shell@Shell** nano-assemblies, without and with **PMMA**, deposited from freshly prepared suspensions and from 11-weeks-aged suspensions are reported in fig.3.4 and show well shaped, spherical nanoparticles. From images, but also from statistical analysis we can argue that no significant agglomeration occurs. The size distribution analysis in fig.3.5 shows that the particle distribution slightly shifts towards larger sizes for 11-aged FONs.

Concerning the role of **PMMA**, the 11-weeks-aged **TW2@TW1@TW0** nanoparticles without **PMMA** display a considerable growth of the average diameter, compared to the same nanosystems deposited just after preparation (from **42** to **56 nm**).

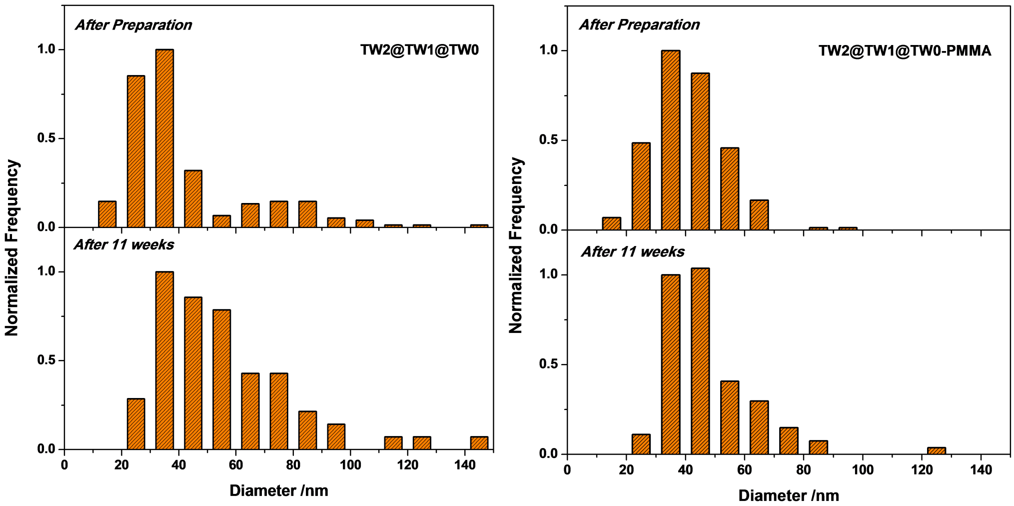

Figure 3.5: Size distribution analysis of undoped an doped-**PMMA Core@Shell@Shell FONs** from TEM images obtained for fresh suspensions (top) and after 11 weeks (bottom).

Contrariwise, nanoparticles doped with **PMMA** display only a weak increase of the diameter (**41** to **48** nm) after 11 weeks, and also maintain a similar size distribution. This is a strong evidence that **PMMA** can play the role of stabilizer and its presence can reduce a further agglomeration.

Moreover, FONs were characterized with DLS, and compared with TEM analysis. The effective diameter and the polydispersity have been directly estimated, while a lognormal distribution analysis provides the number-weighted size classification of NPs in water. The DLS data for freshly prepared and 11-week-aged samples are collected in the table 3.2. The mean diameter, estimated via TEM, is comparable with the number-weighted mean diameter of DLS.

DLS effective diameter ($R_0$) ranges from **96** to **134** nm, and the polydispersity index (PDI) between **0.14** and **0.24**. From these data, the number-weighted mean diameter ($r$) was estimated by assuming a lognormal distribution and is ranged from **42** to **60 nm**. The effective diameter of the single-component **TW0**, **TW1** nanoparticles

Table 3.1: Colloidal and morphological characteristics:**Zeta-potential** and **TEM average diameter**, for freshly prepared FONs.

| **Sample** | **Z-potential** (mV) | **TEM mean diam.** (nm) |
|---|---|---|
| **TW0** | $-42 \pm 2$ | - |
| **TW1** | $-46 \pm 1$ | 55 |
| **TW2** | $-36 \pm 3$ | 64 |
| **TW0-PMMA** | $-42 \pm 1.5$ | - |
| **TW1-PMMA** | $-43 \pm 2$ | - |
| **TW2-PMMA** | $-31 \pm 1.5$ | - |
| **TW2@TW1@TW0** | $-44 \pm 2$ | 42 |
| **TW2@TW1@TW0-PMMA** | $-40 \pm 1.5$ | 41 |
| **Composites** | $-44 \pm 2$ | 62 |
| **Composites-PMMA** | $-34 \pm 2$ | - |

and **TW2@TW1@TW0** nanoparticles slightly increases during time (5-10%), while it stays constant for **TW2** nanoparticles and decreases (6%) for **TW0/TW1/TW2** composite nanoparticles.

The polydispersity stays constant for **TW1** and **TW2** nanoparticles, while it increases for **TW0** and composite nanoparticles and decreases for **TW2@TW1@TW0** nanoparticles. Consistently, the number-weighted mean diameter decreases for **TW0** and **Composite** nanoparticles, stays roughly constant for **TW1** and **TW2** nanoparticles and significantly increases for **Core@Shell@Shell** nanoparticles.

Table 3.2: DLS characteristics: Effective diameter ($R_0$), polydispersity index (PDI) and number-weighted mean diameter (r), for freshly prepared and 11-week aged FONs.

| | Fresh | | | 11-weeks | | |
|---|---|---|---|---|---|---|
| sample | $R_0$ (nm) | PDI* | r (nm) | $R_0$ (nm) | PDI | r (nm) |
| **TW0** | 134 | 0.19 | 57 | 141 | 0.28 | 39 |
| **TW1** | 133 | 0.24 | 45 | 141 | 0.24 | 49 |
| **TW2** | 96 | 0.17 | 44 | 96 | 0.17 | 43 |
| **TW0-PMMA** | 117 | 0.20 | 51 | | | |
| **TW1-PMMA** | 112 | 0.20 | 50 | | | |
| **TW2-PMMA** | 95 | 0.18 | 47 | | | |
| **TW2@TW1@TW0** | 118 | 0.23 | 42 | 128 | 0.18 | 57 |
| **TW2@TW1@TW0-PMMA** | 122 | 0.20 | 47 | 117 | 0.21 | 44 |
| **Composites** | 118 | 0.18 | 60 | 111 | 0.18 | 53 |
| **Composites-PMMA** | 133 | 0.18 | 58 | | | |

[*] Polydispersity Index is the normalized second cumulant defined from the polynomial fitting parameters. For a Gaussian size distribution is equal to $(\frac{width}{mean})^2$ : $PDI < 0,2$ monodispersed system, $PDI > 0,2$ polydispersed system

### 3.2.4 Linear Spectroscopic Characterization

All samples have been optically characterized and their photophysical properties have been checked during a period of 11 weeks. UV-Vis and fluorescence spectra were recorded and luminescence quantum yields of the suspensions were measured using fluorescein as reference. For comparison, the quantum yields of ternary **Composite** and **Core@Shell@Shell** nanoparticles and of **TW1** FONs were also estimated using an integrating sphere Quanta-$\Phi$, mounted in fluorometer. The linear optical properties are collected in the table 3.3.

**Fluorescence decays** were measured in a **TCSPC** (time-correlated single-photon counting) configuration, under excitation from selected nanoLED and data collected for each fluorescence band. Fluorescence lifetimes were fitted with three-exponential functions. The quality of the fits was judged by the reduced $\chi^2$ value ($\chi^2 < 1.1$).

#### 3.2.4.1 UV-Vis Spectroscopy

The absorption spectra of **TW0**, **TW1**, **TW2**, **TW2@TW1@TW0** and **Composites** FONs, with and without the stabilizer agent (**PMMA**) have been recorded and are reported in fig. 3.6. **TW0** FONs have a single absorption band at 331 nm. **TW1** and **TW2** FONs have two typical bands at 342nm/422nm and 340nm/515nmm, respectively. The ternary nanosystems show three major bands due to the superposition of the absorption spectra of the three monocomponent nanoparticles.

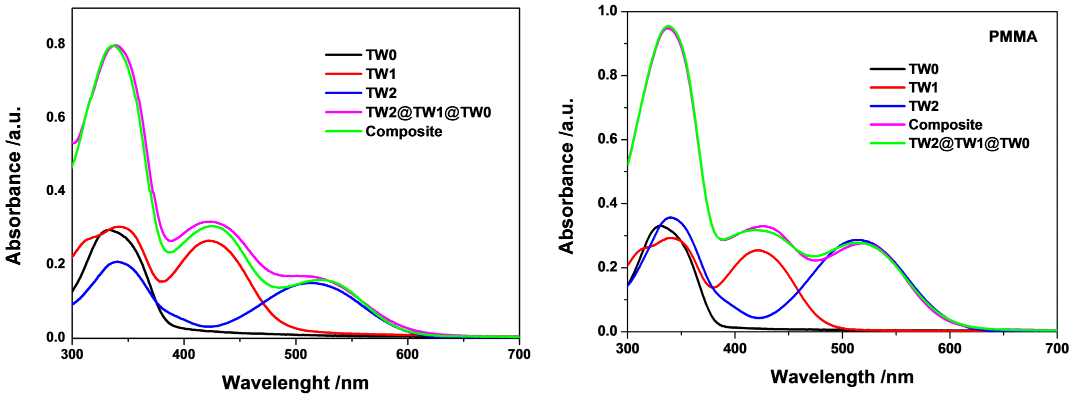

Figure 3.6: UV-Vis spectra of fresh prepared FONs (left) undoped and (right) doped-**PMMA**.

#### 3.2.4.2 Steady-State and Time-Resolved Fluorescence Spectroscopy

Steady-State Fluorescence spectra were registered for three different excitation wavelengths (**340 nm**, **420 nm**, **520 nm**), close to the maxima of absorption bands. (fig. 3.7)

When the **Core@Shell@Shell** nanoparticles are excited at 340 nm, where all of the three compounds absorb, the emissions of **TW0** and **TW1** are strongly quenched, while the emission of **TW2** in the red spectral region is strongly enhanced. A similar behaviour is observed in composite nanoparticles, with a complete quenching of the emissions from **TW0** and **TW1** and an enhancement of the fluorescence signal from **TW2**. Another interesting consideration is that the fluorescence of **Core@Shell@Shell** nanoparticles is sizably blue-shifted compared to the emission of the acceptor (**TW2**) nanoparticles and of composite nanoparticles as well.

Table 3.3: Linear optical properties of FONs (free and doped **PMMA**).

| **Sample** | $\lambda_{Abs}^{max}$ **(nm)** | $\lambda_{Em}^{max}$ **(nm)** [a] | $\Phi$ [b] |
|---|---|---|---|
| **TW0** | 331 | 390/-/- | 0.08 |
| **TW1** | 342/422 | 522/522/- | 0.07 |
| **TW2** | 340/515 | 697/697/697 | 0.06 |
| **TW2@TW1@TW0** | 338/423/514 | 623/625/692 | 0.20 |
| **Composites** | 336/424/524 | 675/675/675 | 0.15 |
| **TW0-PMMA** | 331 | 391/-/- | 0.13 |
| **TW1-PMMA** | 341/422 | 546/546/- | 0.09 |
| **TW2-PMMA** | 340/514 | 700/700/700 | 0.15 |
| **TW2@TW1@TW0-PMMA** | 338/421/516 | 652/648/687 | 0.15 |
| **Composites-PMMA** | 338/426/521 | 673/673/675 | 0.14 |

[a] Maximum of emission under excitation in three different wavelength (340nm, 420nm, 520nm).

[b] Fluorescence quantum yield was estimated through the comparative method, using fluorescein as a reference. ($\Phi = 0.9$)

When **TW2@TW1@TW0** nanoparticles are excited at 420 nm, where only **TW1** absorbs, the emission of **TW1** is strongly quenched and the fluorescence spectrum (from **TW2** acceptor) is very similar to what observed for excitation at 340 nm. From the decrease of the emission intensity of the donor (**TW1**) with respect to the single-component nanoparticles, the efficiency of the **EET** process from **TW1** to **TW2** in the **Core@Shell@Shell** nanoparticles can be estimated to 90%. Composite **TW0/TW1/TW0** nanoparticles excited at 420 nm instead show a complete quenching of the **TW1** emission occurs, and an enhanced emission from the **TW2** acceptor, similar to what observed for excitation at 340 nm.

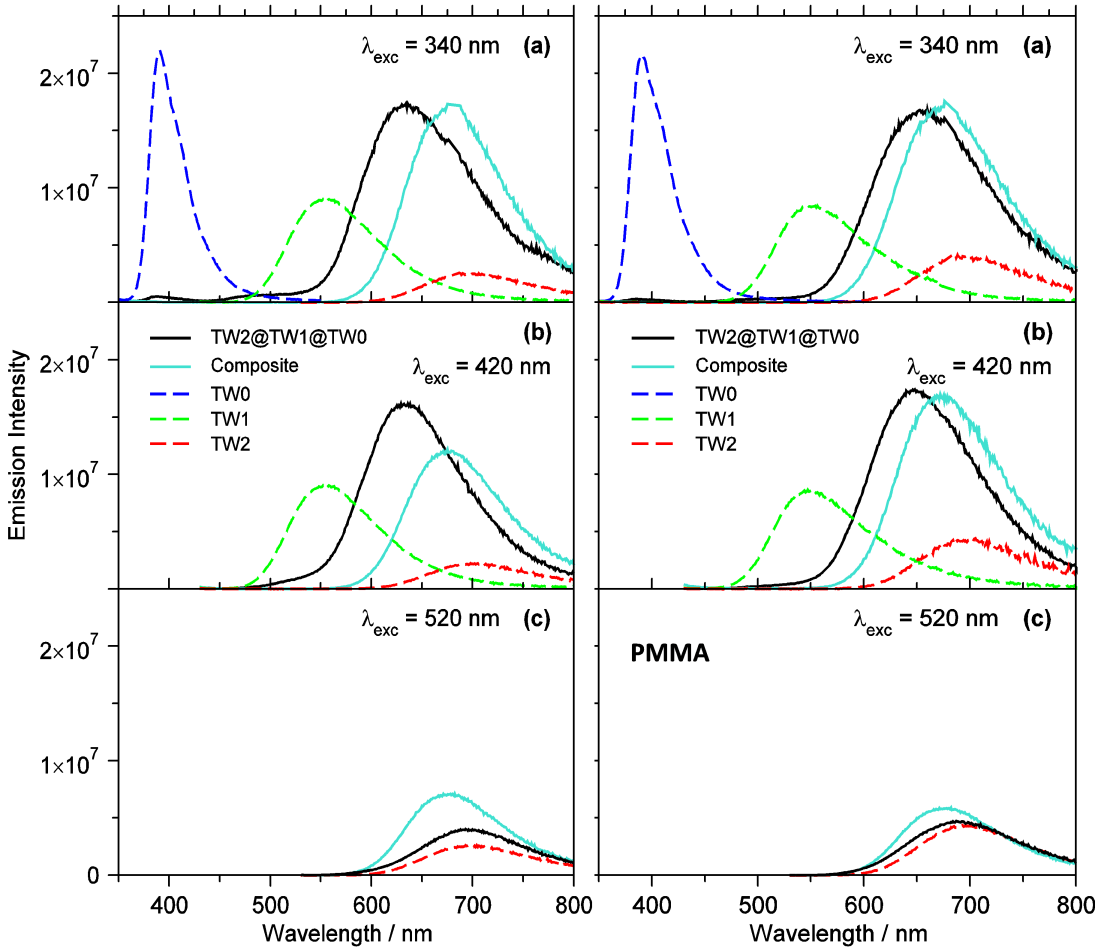

Figure 3.7: Fluorescence spectra of freshly prepared FONs (left) undoped and (right) doped with **PMMA**. Excitation wavelength (a) **340 nm**, (b) **420 nm**, (c) **520 nm**.

When the ternary nanoassemblies are excited at 520 nm, where **TW0** and **TW1** do not absorb, only **TW2** is selectively and directly excited, and is responsible for the fluorescence emission. It can be noticed that, in this case, **Core@Shell@Shell** nanoparticles have the same emission spectrum, in terms of energy and intensity, as **TW2** FONs, while the fluorescence spectrum of composite structures is slightly blue-shifted compared to the spectrum of pure **TW2** FONs.

Fluorescence excitation profiles of ternary FONs were also measured (fig.3.8). The excitation profile of **Composite** nanoparticles is independent of the emission wavelength, while the excitation spectrum of **Core@Shell@Shell** nanoparticles strongly depends on the emission wavelength. In particular, when detecting at long wavelength (700 nm), the excitation profile has a contribution from all of the three chromophores that compose the nanoparticles, while emission at shorter wavelength (625 nm) is mainly originated by direct excitation of **TW0** and **TW1** chromophores in the two shells (and subsequent EET to the core **TW2** chromophores at the core/shell nanointerface).

This different spectroscopic behaviour of **Composites** and **Core@Shell@Shell** nanoparticles suggests strongly two different natures for the two types of trenary FONs. The picture of the proposed enegy transfer mechanism will be discussed more in detail later.

To fully characterise the samples, fluorescence lifetimes have been estimated via fluorescence decays measurements. FONs were excited at two different wavelengths (375 nm and 405 nm) and decays were detected at the three maximum emission wavelengths of the three compounds. The decay data are collected in tables 3.4 and 3.5.

For excitation wavelength at 340 nm and when detecting at 620 nm , corresponding to the emission of the core **TW2**, an about threefold increase of the energy-acceptor lifetime is obtained for **Core@Shell@Shell** nanostructures, while an about twofold increase is found in composite nanostructures. Rather, if the fluorescence decays are measured at 400 and 525 nm, the emitting maxima of **TW0** and **TW1**, respectively, a major shortening of the fluorescence lifetimes is recorded for the ternary nanoassem-

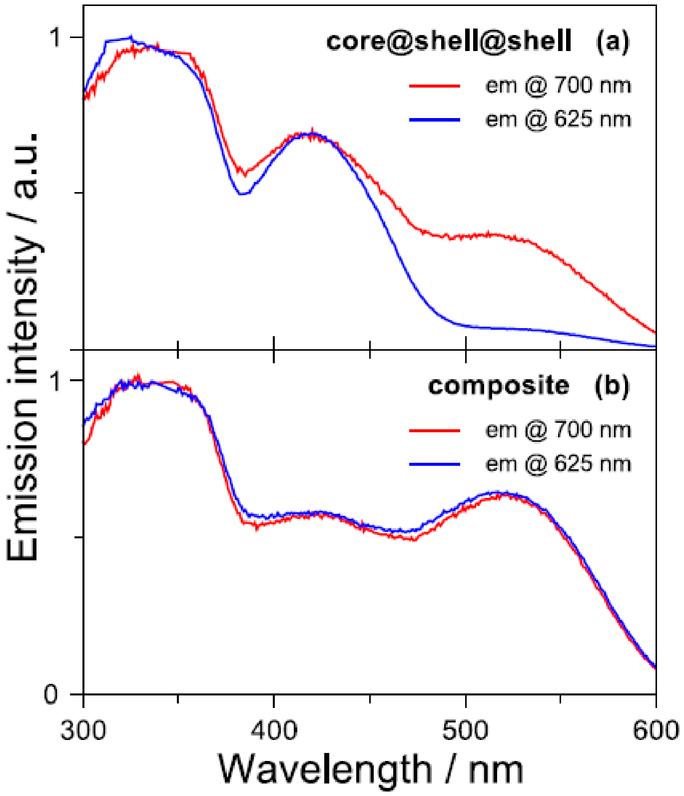

Figure 3.8: Excitation profiles, detected at 625 nm and 700 nm emission wavelength, of **TW2@TW1@TW0** (up) and **Composite** FONs (down).

blies. The marked shortening of the donor's luminescence lifetimes and the lengthening of the acceptor luminescence lifetime in these nanostructures provide another confirmation of the efficient energy transfer cascade (**TW0**→ **TW1**→**TW2**).

For excitation at 405 nm (corresponding to an almost selective excitation of **TW1**) and detecting at 620 nm: the EET process from **TW1** to **TW2** is clearly confirmed by the approximately threefold and twofold lengthening of the energy acceptor lifetimes for **Core@Shell@Shell** and **Composite** nano systems, respectively.

Experimental evidences show that the fluorescence characteristics of nanostructures are strongly affected by the organization of the chromophores within the particles (fig.3.9). In the layered **Core@Shell@Shell** structures an EET cascade takes place from the external to the inner shell and finally to the core. When excitation is at 520

Table 3.4: Lifetime decays of FONs. Excitation wavelength: 340 nm. Decay emission wavelength:400 nm, 525 nm, 620 nm

| | $\lambda_{em} = 400nm$ | | | $\lambda_{em} = 525nm$ | | | $\lambda_{em} = 620nm$ | | |
|---|---|---|---|---|---|---|---|---|---|
| sample | $\tau_1$ (nsec) | $\tau_2$ (nsec) | $\tau_3$ (nsec) | $\tau_1$ (nsec) | $\tau_2$ (nsec) | $\tau_3$ (nsec) | $\tau_1$ (nsec) | $\tau_2$ (nsec) | $\tau_3$ (nsec) |
| **TW0** | 0.48<br>(0.98) | 2.26<br>(0.02) | - | - | - | - | - | - | - |
| **TW1** | - | - | - | 0.40<br>(0.40) | 1.48<br>(0.43) | 3.93<br>(0.17) | - | - | - |
| **TW2** | - | - | - | - | - | - | 0.73<br>(0.23) | 2.64<br>(0.54) | 5.83<br>(0.23) |
| **TW0-PMMA** | 0.28<br>(0.28) | 0.62<br>(0.71) | 3.59<br>(0.01) | - | - | - | - | - | - |
| **TW1-PMMA** | - | - | - | 0.32<br>(0.38) | 1.29<br>(0.46) | 3.7<br>(0.16) | - | - | - |
| **TW2-PMMA** | - | - | - | - | - | - | 0.48<br>(0.23) | 2.92<br>(0.49) | 6.97<br>(0.28) |
| **TW2@TW1@TW0** | - | - | - | 0.35<br>(0.64) | 1.48<br>(0.30) | 6.71<br>(0.06) | 2.60<br>(0.26) | 7.51<br>(0.60) | 25.80<br>(0.14) |
| **TW2@TW1@TW0-PMMA** | ND | ND | ND | 0.34<br>(0.82) | 1.60<br>(0.12) | 6.66<br>(0.06) | 1.05<br>(0.14) | 4.62<br>(0.61) | 13.35<br>(0.25) |
| **Composites** | ND | ND | ND | ND | ND | ND | 2.7<br>(0.19) | 6.66<br>(0.65) | 22.94<br>(0.16) |
| **Composites-PMMA** | ND | ND | ND | ND | ND | ND | 0.54<br>(0.18) | 3.34<br>(0.47) | 8.25<br>(0.35) |

ND Very weak signal of fluorescence.Results of fitting with three-exponential function. In parenthesis is the relative contribution in total decay.The quality of the fits was judged by the reduced $\chi^2$ value ($\chi^2 < 1.1$).

nm, where only the core **TW2** absorbs (direct excitation of core), emission occur from the molecules located in all the volume of core, hence the emission wavelength of **Core@Shell@Shell** is the same of acceptor's (**TW2**) emission. For excitation at 340 nm or 420 nm **TW2** via EET so that the luminescence from the core is localized at the core/shell nanointerface, where the EET probability is maximized. In that case the emission of **Core@Shell@Shell** is shifted to the blue spectral region with respect to acceptor's (**TW2**) emission. The blue-shifted emission is related to the difference in environment as compared to pure acceptor nanoparticles or the **TW2** molecules in the inner part of the core in the **Core@Shell@Shell** nanoparticles.

The mechanism is different for composite nanostructures: in this case, the chromo-

Table 3.5: Lifetime decays of FONs. Excitation wavelength: 405 nm. Decay emission wavelength:525 nm, 620 nm

.

| | $\lambda_{em} = 525nm$ | | | $\lambda_{em} = 620nm$ | | |
|---|---|---|---|---|---|---|
| sample | $\tau_1$ (nsec) | $\tau_2$ (nsec) | $\tau_3$ (nsec) | $\tau_1$ (nsec) | $\tau_2$ (nsec) | $\tau_3$ (nsec) |
| **TW0** | - | - | - | - | - | - |
| **TW1** | 0.40<br>(0.38) | 1.41<br>(0.43) | 3.79<br>(0.19) | - | - | - |
| **TW2** | - | - | - | 0.47<br>(0.25) | 1.90<br>(0.60) | 5.68<br>(0.15) |
| **TW0-PMMA** | - | - | - | - | - | - |
| **TW1-PMMA** | 0.39<br>(0.28) | 1.57<br>(0.50) | 4.15<br>(0.22) | - | - | - |
| **TW2-PMMA** | - | - | - | 0.29<br>(0.36) | 1.70<br>(0.44) | 5.06<br>(0.20) |
| **TW2@TW1@TW0** | 0.4<br>(0.52) | 1.07<br>(0.39) | 2.82<br>(0.09) | 6.30<br>(0.70) | 20.96<br>(0.11) | |
| **TW2@TW1@TW0-PMMA** | 0.34<br>(0.82) | 1.60<br>(0.12) | 6.66<br>(0.06) | 1.05<br>(0.14) | 4.62<br>(0.61) | 13.35<br>(0.25) |
| **Composites** | ND | ND | ND | 0.82<br>(0.17) | 4.65<br>(0.60) | 13.12<br>(0.23) |
| **Composites-PMMA** | ND | ND | ND | 0.48<br>(0.19) | 3.15<br>(0.47) | 8.85<br>(0.34) |

ND Very weak signal of fluorescence.Results of fitting with three-exponential function. In parenthesis is the relative contribution in total decay.The quality of the fits was judged by the reduced $\chi^2$ value ($\chi^2 < 1.1$).

phores are supposedly randomly distributed inside the nanoparticles, so all acceptor molecules statistically have the same environment, hence the emission from the acceptor is independent of the excitation wavelength, i.e. it is the same if the acceptor is directly excited or if it becomes excited via EET.

#### 3.2.4.3 Optical Properties and Colloidal Stability

To evaluate the influence of **PMMA** on the stability of the suspensions, with respect to their spectroscopic characteristics, absorbance and fluorescence were recorded versus time. The evolution of absorbance and fluorescence intensity during a period of 11-

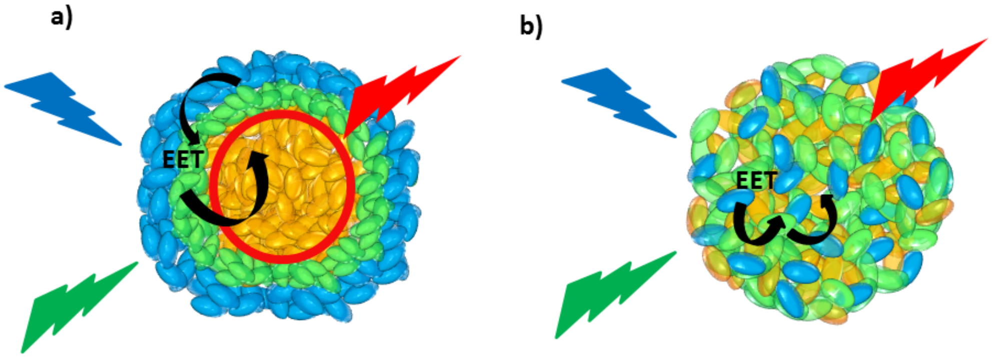

Figure 3.9: Picture of Energy Transfer mechanism in a) **Core@Shell@Shell** FONs and b) **Composites** FONs. In **Core@Shell@Shell** nanoparticles the EET is localized at the interface of donor **TW1** and acceptor **TW2**. In **Composites**, EET appears in the whole volume of the particle.

weeks, of **Core@Shell@Shell** and **Composites** FONs, with and without **PMMA** is shown in fig.3.10 and 3.11.

The UV-Vis spectra indicate a small variation of absorbance: only a slight progressive growth of the three bands is observed, which can safely be ascribed to a small variation of the concentration, due to a partial evaporation of water.

However, the emission spectrum of **Core@Shell@Shell** nanoparticles without **PMMA** dramatically decreases after three days, then the decrease becomes much slower and no significant change is detected any more after 11 weeks. The emission spectrum of **PMMA**-doped **Core@Shell@Shell** nano-assemblies has a much less pronounced initial decrease, but a smooth decrease is anyhow detected for a few weeks. A similar behaviour is observed for **Composite** nanoparticles.

The ratio between the emission maximum and the absorbance at the excitation wavelength is reported in Fig. 3.12 as a function of time. This ratio, and consequently the quantum yield (proportional to this ratio) decreases both for free and doped nanoassemblies, but the slope is steeper in systems without **PMMA** and their quantum yield stays always lower than for **PMMA**-doped systems.

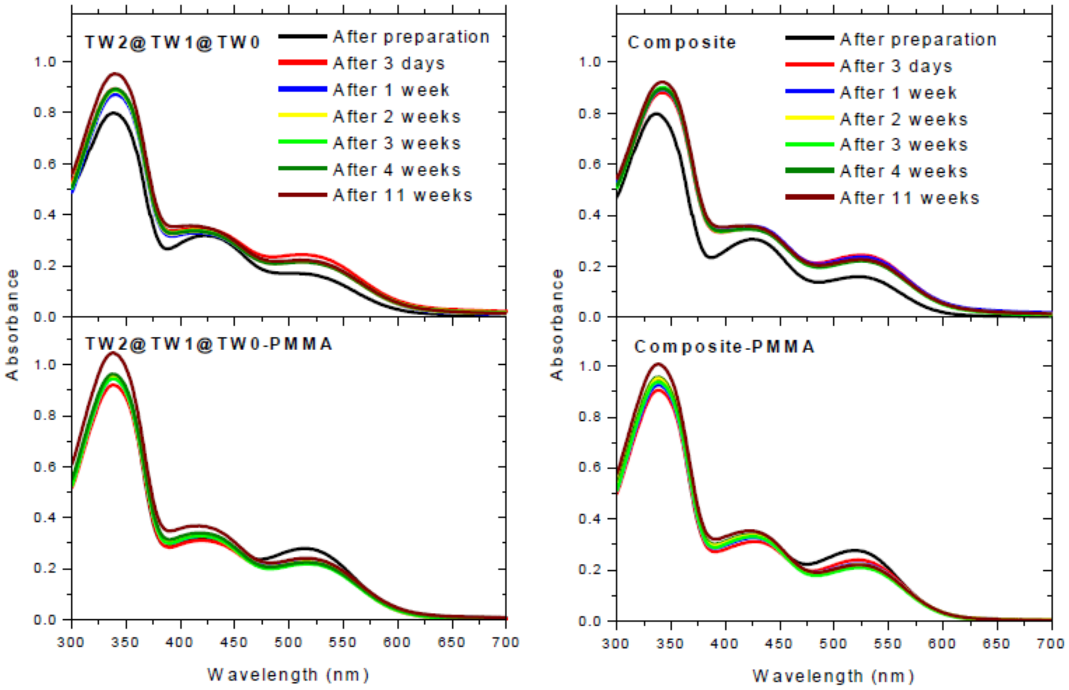

Figure 3.10: UV-Vis spectra versus the time of ternary prepared FONs (up) undoped and (bottom) **PMMA**-doped.

As there is no significant variation of the absorption spectra, the intensity variation of the emission spectra can be mainly ascribed to a slow rearrangement of molecules inside the nanoparticles, such as anti-parallel orientation of the dipolar chromophores leading to reduced radiative decay rates and favoring competing nonradiative decay processes. Apparently, the presence of **PMMA** plays a role in reducing such effects by reducing interactions between chromophores and slowing down their rearrangement within the nanoparticles.

### 3.2.5 Two-Photon Excited Fluorescence

The ternary nanosystems and the corresponding monocomponent nanoparticles were investigated with the Two Photon Excited Fluorescence (**TPEF**) technique (Appendix 1). Briefly, the experimental set-up allows to record fluorescence emission spectra under multiphoton excitation at variable excitation powers and wavelengths. Whatever

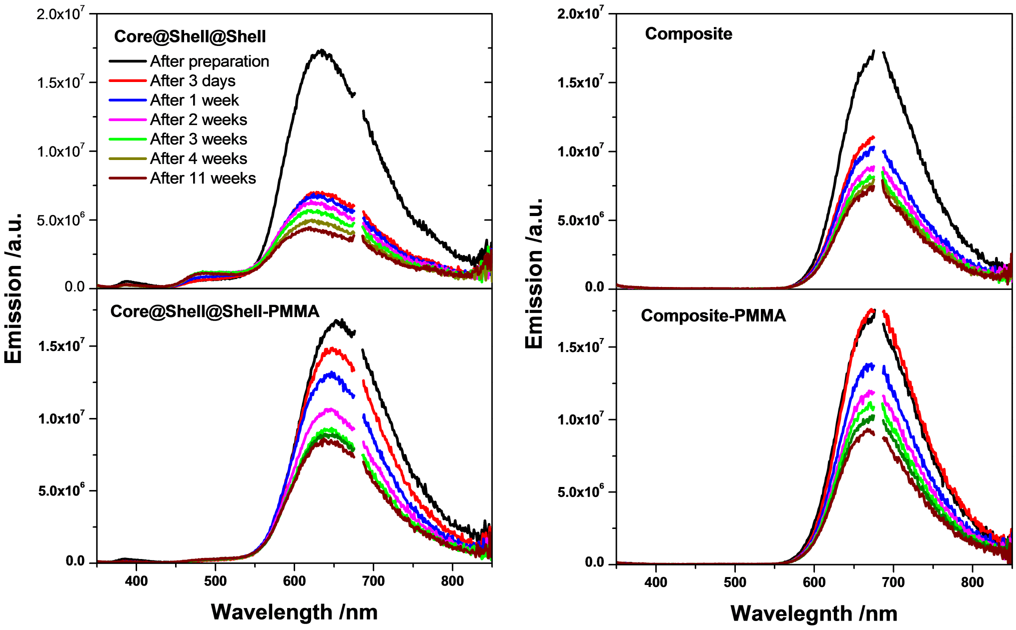

Figure 3.11: Fluorescence spectra versus the time of freshly prepared FONs (up) undoped and (bottom) **PMMA**-doped.

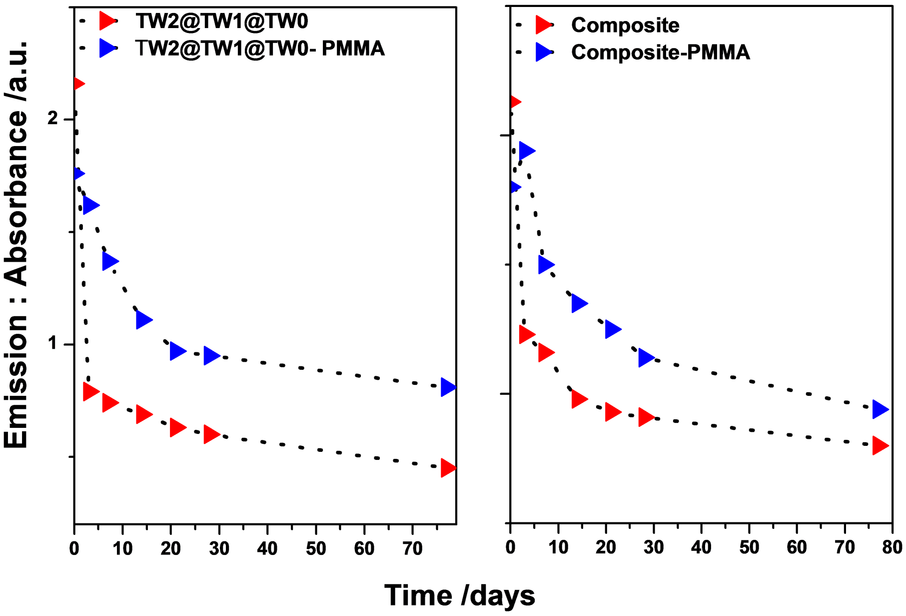

Figure 3.12: Temporal evolution of the ratio between intensity of absorption and emission, undoped and **PMMA**-doped **Core@shell@Shell** (left) and **Composite** (right) FONs.

excitation wavelength, extremely weak TPEF signals were detected from monocomponent FONs. Even when exciting at 840 nm, i.e. twice the wavelength of maximum one-photon absorption of **TW1**, only a very weak TPEF signal is detected for **TW1** FONs (fig.3.13). No significant TPEF signal could be detected from **TW2** nanoparticles, even when two photon pumping at 1040 nm, where is the twice the one-photon maximum absorption wavelength of **TW2** (fig.3.14).

Antithetically, multicomponent nanoparticles show well detectable TPEF spectra that nicely correspond to those obtained with standard one-photon excitation (fig.3.15). In particular, when pumping at 840 nm, where **TW1** is almost selectively two-photon excited (since at 420 nm the linear absorption of **TW0** and **TW2** is very low), the multicomponent nanoparticle suspensions show a dramatic increase of the two-photon induced fluorescence signal. The fluorescence signal clearly arises from **TW2** molecules that get indirectly excited via excitation energy transfer from **TW1**, as already observed in the case of one-photon excitation. The same trend is observed as in one-photon induced fluorescence spectra, i.e. the TPEF signal from **Core@Shell@Shell** nanoparticles is blueshifted with respect to the TPEF signal from composite nanoparticles. A well detectable TPEF signal is also measured for **Core@Shell@Shell** nanoparticles when two-photon excitedat 1040 nm, i.e. when directly exciting **TW2** molecules in the core.

The amplification of the TPEF signal in ternary nanoparticles cannot be simply ascribed to the increased luminescence quantum yield of **Core@Shell@Shell** and **Composite** nanoparticles with respect to the monocomponent nanoparticles. In fact, the quantum yield gain accounts only for an about threefold amplification , while the observed TPEF enhancement amounts to 12 for ternary nanoparticles excited at 840 nm. The intensity of the TPEF signal is proportional to the $\sigma_2\Phi$ product, where $\sigma_2$ is the two-photon absorption cross section. Since in the case of two-photon excitation at

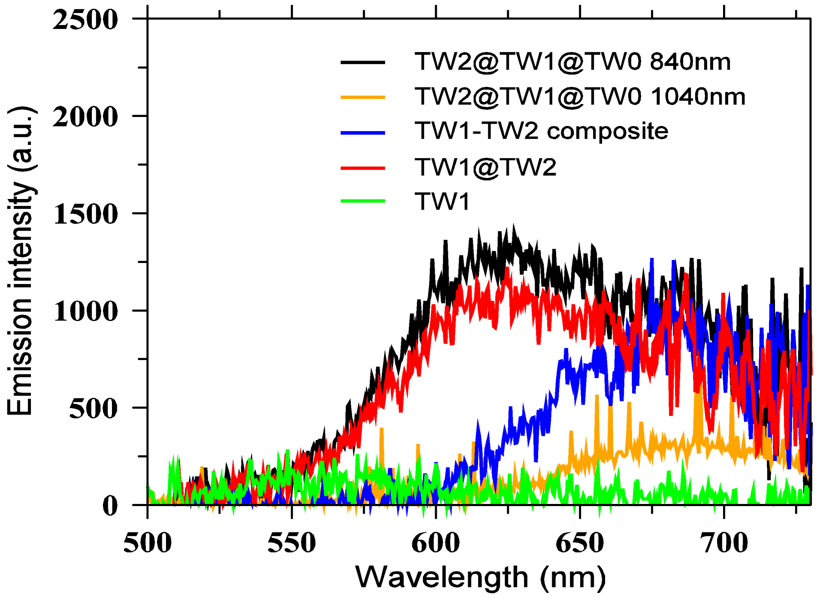

Figure 3.13: Two Photon Excited Fluorescence spectra of FONs .

840 nm only **TW1** absorbs, in our case the intensity of the TPEF signal is proportional to the two photon absorption cross section of **TW1** at 840 nm. Therefore, these results demonstrate that the $\sigma_2$ of **TW1** is strongly amplified, by a factor of about 4, in the ternary nanosystems with respect to the monocomponent nanoparticles. Similarly, the TPA cross section of **TW2** is also strongly amplified in **Core@Shell@Shell** nanoparticles with respect to monocomponent nanoparticles, but the amplification factor cannot be estimated, as the TPEF signal from pure **TW0** nanoparticles is too weak to be quantified.

The estimated molecular 2PA cross section for **TW1** nanoparticles is 35 GM at 840 nm. The estimation of the 2PA cross section of **Core@Shell@Shell** nanoparticles is smooth for excitation at wavelengths longer than 1000 nm, i.e. when only **TW2** gets two-photon excited and the TPEF signal is simply due to the emission of the directly excited **TW2** molecules. For **Core@Shell@Shell** nanoparticles, we obtain a 2PA cross section of about 80 GM at 1040 nm. On the other hand, the estimation of the 2PA cross section of multicomponent nanoparticles is not straightforward when EET occurs.

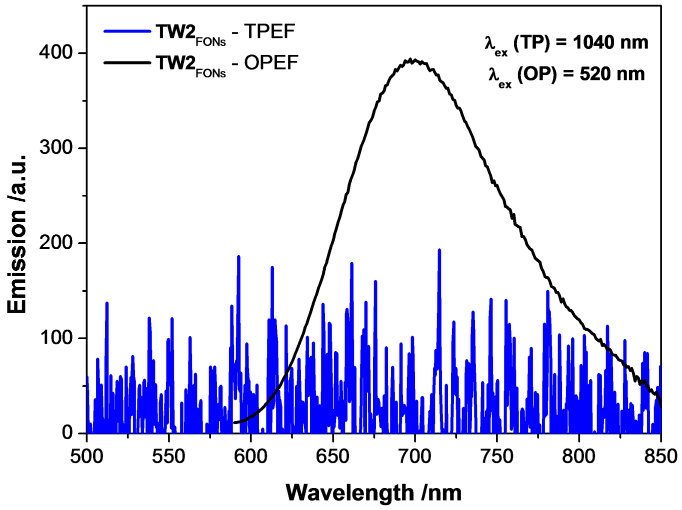

Figure 3.14: One-photon excitation fluorescence (OPEF) spectrum and two-photon excitation fluorescence (TPEF) spectrum of **TW2** FONs.

When excited at wavelengths shorter than 1000 nm, **TW1** also starts two-photon absorbing (below 800 nm also **TW0** would get two-photon excited) but emission still stems from **TW2** molecules that get excited via EET from **TW1** (or **TW0**). Therefore, in order to estimate the correct 2PA cross section at wavelengths shorter than 1000 nm, the precise energy-transfer quantum yield is needed. Assuming a 100% yield of the EET process, a nominal 2PA cross section amounting to 120 GM at 840 nm is estimated for **TW1** in the **Core@Shell@Shell** nanoparticles. However, this value is the lower-limit threshold for $\sigma_2$, that has to be corrected for the EET quantum yield (estimated to amount to 0.9 from single-photon excitation at 420 nm), leading to a final value of 133 GM. This analysis confirms that the amplification factor of the 2PA cross section of **TW1** in **Core@Shell@Shell** nanoparticles with respect to **TW1** single-component nanoparticles amounts to about 4 (at 840 nm).

The origin of this remarkable amplification can be related to the different environment experienced by the chromophores with respect to single component nanoparticles, and to local fields developing inside the ternary nanostructures at the bound-

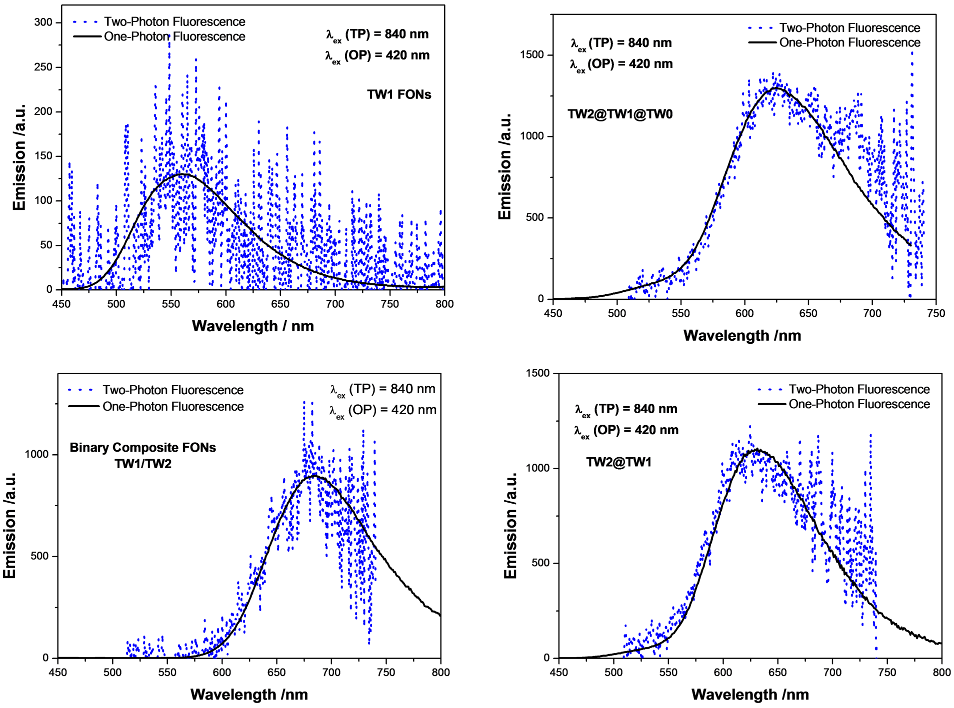

Figure 3.15: Comparison between the two-photon excited fluorescence (TPEF) spectrum and the one-photon excited fluorescence spectrum of the nanoparticle suspensions displaying a sizable TPEF signal.

ary regions between the different molecular components. Indeed two-photon absorption has been found earlier to be extremely sensitive to weak and short-range electrostatic effects. The molecular two-photon brightness ($\sigma_2\Phi$) of our **TW2@TW1@TW0** nanoparticles amounts to 27 GM at 840 nm (which is well suitable for bioimaging) versus 2 GM for **TW1** singlecomponent nanoparticles. It is worth estimating the two-photon brightness per nanoparticle by employing the mean diameter obtained via DLS and a tentative density of 1.35 g/$cm^3$ (based on the crystal density of similar compounds) [92]. We obtain 1.4x$10^5$ GM for **TW1** nanoparticles and 1.2x$10^6$ GM for **TW2@TW1@TW0** nanoparticles. These correspond to a two-photon brightness per unit nanoparticle volume of 3 GM/$nm^3$ for **TW1** nanoparticles, and 32 GM/$nm^3$ for **TW2@TW1@TW0** nanoparticles at 840 nm. This last value is much higher than what is reported for other nanoaggregates [93], or fluorescent doped mesoporous nanoparticles [94], and even better than CdSe-ZnS water-soluble quantum dots [87].

## 3.3 Conclusions

Above all, in this chapter we reported an effective and simple way to obtain ternary organic nanoassemblies for EET composed by triphenylamine-based chromophores. Two kinds of three-component nanoparticles have been prepared through the reprecipitation method: in the first type, called **Core@Shell@Shell**, the molecules are arranged in a layered nanostructure composed of an inner core (**TW2**), an internal shell (**TW1**) and an external shell (**TW0**). In second type, called composite, the three dyes are randomly mixed together to form the nanoparticles. Furthermore, the role of the optically neutral polymer **PMMA** as a stabilizer agent was evaluated in the morphological and spectroscopic properties of the fluorescent organic nanostructures.

The good colloidal stability of the suspensions has been confirmed through different experimental techniques, such as UV-vis and Fluorescence spectroscopy, Zeta-potential and DLS. The relatively good colloidal stability appears to be further improved by polymer doping. Specific **PMMA** doping could be of particular interest for materials applications, while more biocompatible polymeric additives or suitable molecular engineering of the dipolar chromophoric subunits of the nanoparticles could be preferred for bioimaging applications.

The absorption and fluorescence spectra of all the nanoparticles have been monitored during 11 weeks: while no significant variation of the absorption spectra is observed, a decrease of emission intensity is detected. This process can be ascribed to the slow rearrangement of molecules inside the nanoparticles. The presence of PMMA reduces these effects most probably by weakening intermolecular interactions between chromophoric subunits and slowing down the rearrangement leading to deleterious mutual orientation, for instance anti-parallel association of dipolar chromophoric subunits.

The prepared ternary nanoparticles show a highly efficient EET cascade between the three molecular components with a strong enhancement of the acceptor emission with respect to monocomponent nanoparticles. The luminescence behaviour of **Core@Shell@Shell** and **Composite** nanoparticles is different because of the different organization of the chromophores in the two types of ternary nanostructures. In the **Core@Shell@Shell** systems, the cascade EET process mainly excites the acceptor molecules in the core lying at the core/shell interface, producing a different luminescence signal than promoted by direct excitation of **TW2** molecules in the core. This behavior is not observed in composite nanoassemblies, where chromophores are randomly distributed and the luminescence from the acceptor is the same independently of the excitation process.

**Core@Shell@Shell** have a more than tenfold increase of the two-photon induced fluorescence signal with respect to single-component nanoparticles. The molecular two-photon brightness, at 840 nm, amounts to 27 GM for **Core@Shell@Shell** nanoparticles, versus barely 2 GM for pure **TW1** nanoparticles. The enhancement of the two-photon brightness cannot be solely ascribed to the increased luminescence efficiency, but is also related to a marked amplification of the 2PA cross section of the donor molecules in the ternary nanoparticles. In fact the 2PA cross section of **TW1** in **Core@Shell@Shell** nanoparticles amounts to 133 GM (at 840 nm), i.e. 4 times higher with respect to **TW1** single-component nanoparticles.

Therefore, we demonstrated that the indirect excitation of the acceptor chromophores via EET from donor molecules in the same nanoparticle is an effective process to improve the two-photon brightness, achieving very interesting results, comparable or even better with respect, for example, to water-soluble quantum dots. Moreover, the exploitation of EET from one of more donor species to obtain emission from the sink fluorophore widens the spectral range of excitation, covering a large part of the biological transparency window (from 600 nm to 1200 nm), still getting an orange-red emission. While a huge amplification of the two-photon brightness is observed in both types of ternary nanostructures, **Core@Shell@Shell** nanoparticles have the advantage of higher luminescence quantum yield and a directional EET cascade (from the external shell to the inner shell to the core, in our case). This last characteristic not only allows for emission localization in a sub-nanoparticle volume, but also drives the energy flow towards a specific core/ shell nanointerface that acts as a nano-heterojunction.

# Chapter 4

# Luminescent Materials based on Organic Radicals

## 4.1 Introduction

Organic radicals are multifunctional materials with peculiar magnetic and opto-electronic properties that can be used in a wide field of technological applications. Since the chemist Moses Gomberg discovered the first organic free radical at the beginning of last century, their physical and chemical properties have been source of inspiration in different fields.

Radicals often appear as intermediates in photochemical and thermal reactions, and are known to initiate and propagate polymerization and combustion reactions. Their high reactivity and their shortlife classify them as unstable materials. However, organic radicals can be modified into stable states, existing for considerable lengths of time and be exploited in various technological fields [95]. Stable radicals and their derivatives already found applications as spin labels for monitoring biolomolcules, or as building blocks for obtaining molecular materials with specific properties [96]

Polychlorotriphenyl methyl compounds are considered inert carbon-centered free-radicals, thanks to their high chemical and thermal stability both in solution and in the solid state, where their half-life is on the order of decades. This stability, joined with the unusual physical and chemical properties given by the open-shell electronic configuration, offers the possibility to exploit these molecules in different fields with remarkable applications like in spintronics as molecular switches [97], as molecular wires or as mediators in $Li/O_2$ batteries [98]. Recently, this class of materials, has been the subject of technological interest not only in electronic and magnetic applications, but also in relation to their optical and optoelectronic properties [99, 100]. Indeed, the presence of an unpaired electron is responsible for several peculiar characteristics: emission at long wavelength despite the absence of elongated $\pi$-systems, large Stokes shift and a doublet electronic configuration both for ground and excited states.

In this chapter we focus our attention on two polychloro triphenylmethyl derivatives, named tris(2,4,6-trichlorophenyl)methyl (**TTM**) and perchlorotriphenylmethyl (**PTM**) (fig.4.1). These molecules have a propeller-like comformation and are composed of three totally or partially chlorinated phenyl rings connected to a central carbon atom ($\alpha$-carbon), where the unpaired electron is mostly localized on. The bulky chlorine atoms at the ortho positions of the three phenyl groups provide a steric protection of the central carbon atom, which is the atom with the major spin density. The protection of the methyl carbon is translated into a large persistence and a very high chemical and thermal stability for this family of radicals [96].

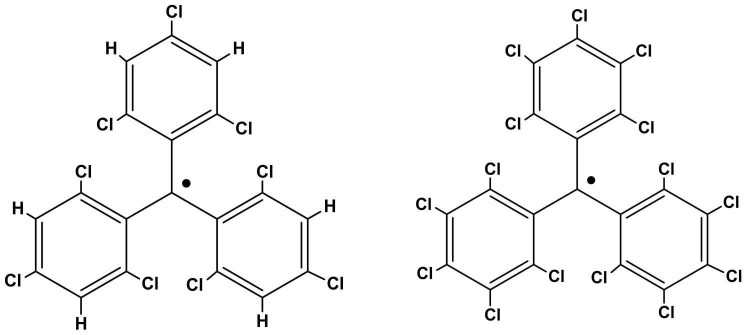

Figure 4.1: Molecular structures of **TTM** and **PTM** radicals.

Recently, Peng et al. reported on the fabrication of the first OLED based on neutral $\pi$ radicals, where the use of a doublet emitter, avoiding the formation of singlet and triplet excitons, can rise the upper limit of internal quantum efficiency up to 100% [101]. However, there are several limiting factors for the use of these radical molecules as photoactive species in optoelectronic devices or as luminescent probes for bioimaging applications. For example, their almost complete insolubility in water hinders their use in biological applications. Another limiting factor is the typically low value of luminescence quantum yield (LQY). In fact, there are only few examples in which polychlorotriphenyl methyl radical derivatives show a LQY higher than 0.3 and only in apolar or poorly polar solvents [99], [100] while in the solid state the emission is completely quenched. Moreover, photostability is also a limiting issue, particularly in solution where, for example, the **PTM** radical shows a photoreaction quantum yield of 0.3 [102].

In order to overcome these drawbacks, Hattori et al. have recently proposed different molecular strategies, like the introduction of heteroatoms in the phenyl rings, the formation of coordination complexes or the substitution of the halogen atoms in the ortho positions [103–106]. These functionalizations enabled reaching hundred times higher values of photostability in solution than the one of the **TTM** radical. A few studies on self-assembled monolayers or micro-particles of polychlorotriphenyl methyl radicals have also been reported but, to the best of our knowledge, no systematic studies are available on the confinement and nanostructuration of radical molecules in solid organic matrices such as organic nanoparticles [107, 108]. Nonetheless, interesting effects can be expected because of reduced vibrations and intermolecular interactions responsible for non-radiative decays [109]. On the other hand, the formation in the solid state of emissive supramolecular aggregates like excimers [110, 111] is a very interesting and exploited strategy in order to have a wide emission able to cover the NIR region but up to now, no examples of excimers based on stable and persistent radical pairs have been reported.

Here, we present a systematic study of the optical properties of **TTM** and **PTM** and discuss different strategies to improve the luminescence and photostability of these materials, exploiting aggregation and medium effects. Aggregation effects have been examined doping different matrices with radical molecules. In particular, we dispersed the radicals into organic nanoparticles (ONPs) and in polymeric films and studied their optical behaviour. Specifically, we investigate the optical behaviour of ONPs made by the closed-shell and optically neutral tris(2,4,6-trichlorophenyl) methane (TTM-$\alpha$H) doped with different amounts of **TTM** or **PTM**. Further, Poly(methyl methacrylate) (PMMA) films doped with different amounts of **TTM** have been deposited on quartz substrate and a fully optical characterization has been preformed.

Regarding their non linear optical (NLO) properties these derivatives are particularly interesting because they can virtually be two-photon excited in the biological transparency window and at the same time have an emission in the red-NIR region. Up to now, there are a number of studies about their NLO properties, but only as constitutive units of "push-pull" compounds that present intramolecular charge transfer (ICT) phenomena. In this work, for first time we discuss the non linear response of the radicals, not as moieties of a more involved compound but as independent molecules. Particularly, the two-photon absorption cross sections of **TTM** and **PTM** were determined recording the two-photon fluorescence excitation spectra. The possibility of two-photon excitation in the transparency window of biological tissue (between 700 and 1500 nm) together with a red-NIR emission, opens new perspectives for using these materials as probes for bioimaging.

## 4.2 Linear Optical Properties of PTM and TTM in solution

**TTM** and **PTM** have been optically characterized via UV-vis absorption and fluorescence spectroscopy in solvents of different polarity. Since radicals are highly photosensitive and their exposure to UV light induces photo-reactions, the samples were prepared and stocked in the dark. Absorption spectra were measured before and after recording fluorescence spectra, in order to check the photostability of solutions upon the irradiation necessary to measure fluorescence. The fluorescence quantum yield was estimated using cresyl violet as a reference. Fluorescence lifetime decays were fitted with single or bi-exponential functions. All spectroscopic characteristics are reported in table 4.1 and in figures 4.2, 4.3.

The UV-vis absorption spectrum of **TTM** shows three absorption bands: a main absorption band located at 375 nm accompanied by a vibronic replica, and two weaker bands in the visible spectral region (500 nm-550 nm). The molar extinction coefficient (fig.4.2) of **TTM** is estimated of ∼35000 $cm^{-1}M^{-1}$ at 375 nm in THF. The UV-vis spectrum of **PTM** is much alike to **TTM**'s, but slightly shifted to the red, with the main absorption band positioned at 385 nm and the two weaker bands at 520 nm and at 570 nm respectively. The molar extinction coefficient of **PTM** is estimated of ∼38000

$cm^{-1}M^{-1}$ at 385 nm in THF.

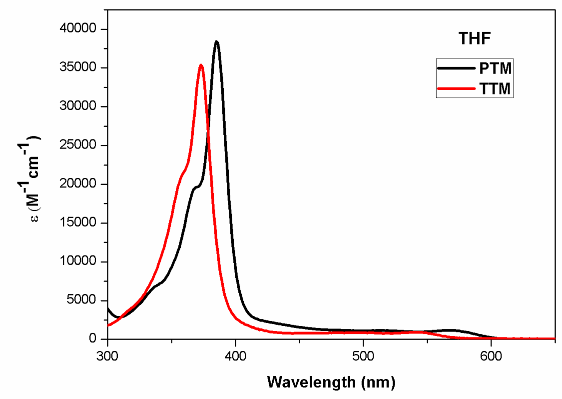

Figure 4.2: Molar extinction coefficient of (**TTM**) and (**PTM**) radicals in THF.

The fluorescence spectra have maxima at 570 (**TTM**) nm and 610 nm (**PTM**) (fig.4.3). Both molecules show weak fluorescence in solution with values of quantum yield not higher than 2% and 3% respectively. No significant solvatochromic behaviour is observed in absorption or in emission.

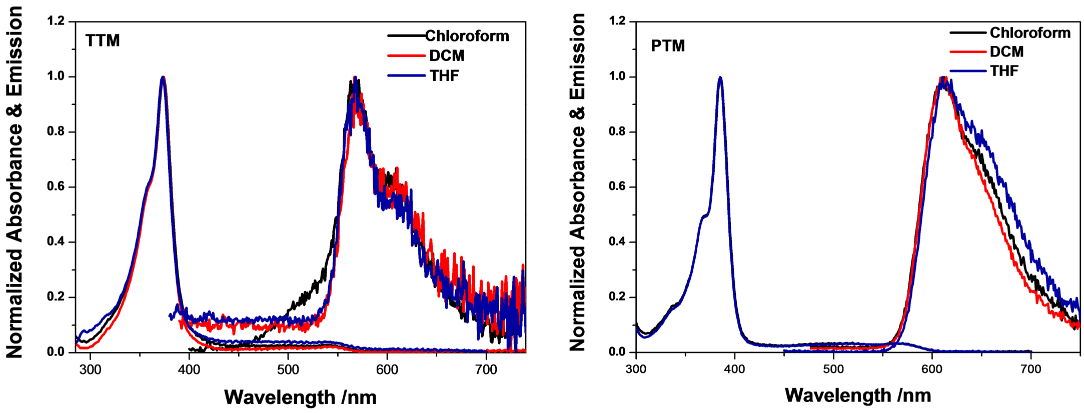

Figure 4.3: UV-vis and emission spectra of **TTM** (left) and **PTM** (right) radicals in solvents of different polarity.

At this point, studies of dispersed molecules in a rigid medium may provide ele-

Table 4.1: Spectroscopic Characteristics of **TTM** and **PTM** derivatives in solvents of different polarity.

| Sample | Solvent | $\lambda_{Abs}$ max (nm) | $\lambda_{Em}$ max (nm) | $\Phi$[a] | $\tau_1$[b] (ns) | $\tau_2$ (ns) |
|---|---|---|---|---|---|---|
| **TTM** | Cyclohexane | 372 | 564 | 0.01 | 5.1 | |
| | Toluene | 375 | 568 | 0.01 | 5.0 | |
| | Chloroform | 374 | 570 | 0.01 | 2.6 (8.76) | 6.5 (91.24) |
| | DCM | 378 | 567 | 0.01 | 5.8 | |
| | THF | 374 | 568 | 0.02 | 7.6 | |
| | 2MTHF (77K) | 375 | 556 | 0.72 | | |
| **PTM** | Chloroform | 385 | 612 | 0.02 | 7.9 | |
| | DCM | 385 | 614 | 0.03 | 9.7 | |
| | THF | 385 | 610 | 0.03 | 9.7 | |
| | 2MTHF (77K) | 387 | 590 | 0.61 | | |

[a] Fluorescence quantum yield was estimated through the comparative method, using cresyl violet as a references ($\Phi = 0.55$, EtOH).

[b] Fluorescence lifetime estimated through mono or bi-exponential reconvolution fit analysis. In parenthesis is the relative contribution in total decay. The quality of the fits was judged by the reduced $\chi^2$ value.

mentary knowledge before we shift to molecular aggregates. Hence, the optical behaviour of the compounds was studied in undercooled solution and medium effects on luminescence properties were evaluated. Typically, fluorophores at low temperature become better emissive, the spectral widths are usually reduced and the vibronic shape is better resolved. The following investigation confirms these expectations.

Absorption and emission spectra of compounds were recorded, in glassy 2-methyl THF at 77 K. In fact, when rapidly cooled at the temperature of liquid nitrogen 2-methyl THF forms a transparent glass. In order to avoid any crystallization and favour the glass transition, the solvent has been dehydrated over molecular sieves type A3, after their activation at $200^0$C. Solvent was kept in contact with sieves overnight and filtered with $0.45\mu$m PTFE filter, in order to remove any residual suspended particle. To adjust temperature, an Oxford Instrument Optistat DN Cryostat was adapted in spectrometer. Moreover, absorption spectra were recorded before and after the measurement of fluorescence, in order to check the photostability of the solutions upon the irradiation necessary to measure fluorescence and the stability upon temperature changes. The fluorescence quantum yield was estimated using cresyl violet as a reference (table 4.1).

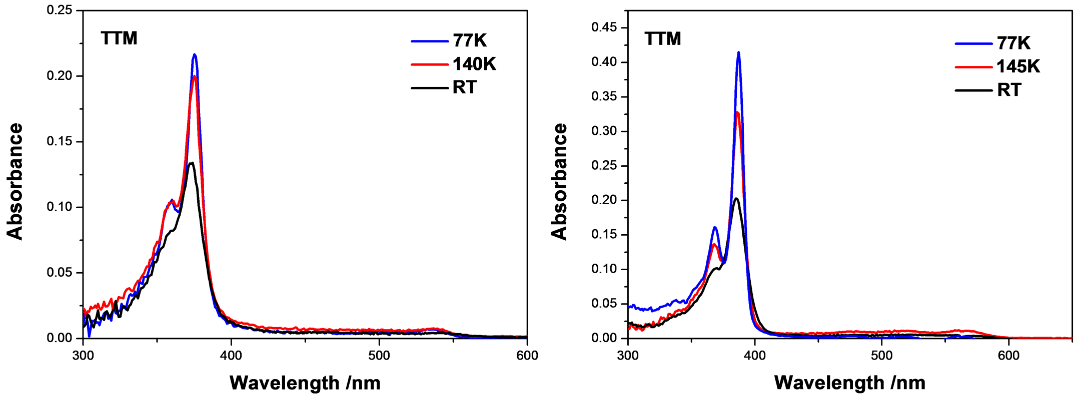

Figure 4.4: Absorbance of **TTM** (left) and **PTM** (right) at room temperature, at 145K and at 77K, in 2-methyl THF.

Absorbance of **TTM** increases (fig.4.4) while the temperature is decreased. The fluorescence signal is enhanced dramatically and the maximum of fluorescence band slightly shifts to the blue spectral region with respect to the solution at room temperature (fig.4.5). In both spectra the vibronic structure is better resolved in the glassy matrix. In the undercooled solution, **TTM** exhibits a luminescence quantum yield (LQY) of 0.72, more than 35 times higher than in THF. A similar behaviour is observed for **PTM**. The luminescence quantum yield is estimated of 0.61 at 77K.

The enhanced luminescence in the glassy matrix can be ascribed to the restriction of thermally activated rotations and vibrations, decreasing the rate of the non radiative process and promoting competitively the relaxation of the excited state via the radiative path. The narrowed absorption and emission reflects the reduced inhomogeneous broadening in the rigid medium. This is a clear evidence the confinement in a rigid medium can improve the emission efficiency.

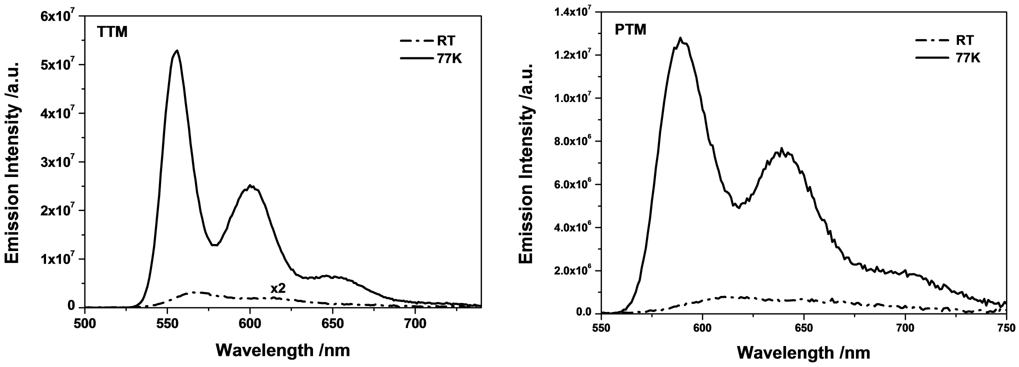

Figure 4.5: Emission intensity of **TTM** (left) and **PTM** (right) at room temperature and at 77K, in 2-methyl THF.

## 4.3 Aggregation effects on Radicals

Since medium effects had a significant influence on the spectroscopic properties of radicals, we shifted our study to molecular aggregation. ONPs composed from pure **TTM** and **PTM** were prepared with the standard reorecipitation method: an aliquot of a high concentrated solution of radical ($10^{-3}$M, THF) is injected in MilliQ water under vigorous stirring. The nominal concentration of radical in suspension was $10^{-5}$ M.

Firstly, the photostability of nanoparticles was evaluated. Absorption spectrum of ONPs was recorded after continuous exposure to room light. The UV-Vis spectra confirm that ONPs are highly stable under white light (fig.4.6), differently from to compounds in solution, which photodegrade after 20 minutes . Indeed, aggregation brings high photostability to compounds, nevertheless the fluorescence is totally quenched (AQC). Pure radical ONPs display optical behaviour very similar to powder i.e. highly stable under light but lacking of fluorescence.

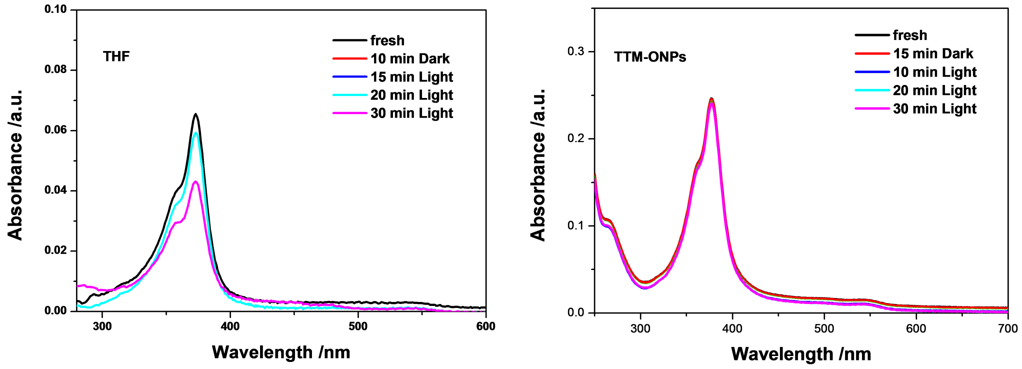

Figure 4.6: Absorbance of **TTM** in THF (left) and ONPs (right) recorded after exposure to white light.

### 4.3.1 ONPs doped with TTM and PTM

Even if it is clear from the low temperature measurements that the confinement in a rigid matrix brings an enhancement of the luminescence, the results of molecular aggregates indicate that another factor, that should be taken into account, is how the molecules interact with neighbours, namely intermolecular interactions. Since pure radical ONPs undergo complete aggregation-caused quenching (ACQ) of fluorescence, we decided to use an optical neutral material as a matrix where to dispersed the radical, in order to control the intermolecular interactions and hinder the quenching of luminescence due to aggregation. Particularly, we prepared of ONPs from the optically neutral tris(2,4,6-trichlorophenyl)methane TTM-$\alpha$H (fig.4.7) where radical molecules were dispersed into, in different amounts.

The closed-shell TTM-$\alpha$H was chosen as the matrix for the ONPs because of its optically neutral behaviour in the range of absorption and emission of the two derivatives. Moreover, its molecular structure, very similar to triphenymethyl radicals, shall grant for good solvation of their molecules, preventing their aggregation and thus reducing the concentration quenching of the luminescence.

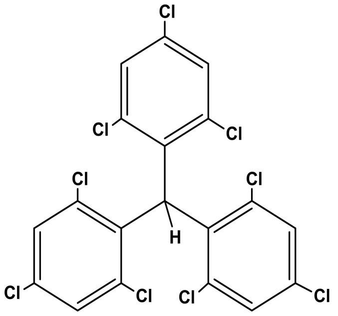

Figure 4.7: Molecular structure of closed shell TTM-$\alpha$H used as an optical neutral matrix for radical molecules.

Nanoparticles of TTM-$\alpha$H doped with different amounts of **TTM** radical (**TTMd-ONPs**) were prepared using the standard reprecipitation method. For the preparation of suspensions 2x10$^{-3}$M solutions of TTM-$\alpha$H containing different amounts of **TTM** were prepared (0.5%, 3%, 6.5%,13%, 26%, 50% of radical in molar ratio).Samples were filtered using Teflon filter of 220 nm before injection into water. Then 100 $\mu$L of these solutions were slowly dropped in 9.9 mL of MilliQ water, at room temperature under vigorous stirring (1000 rpm). At the end of reprecipitation, the nominal concentration of radical and TTM-$\alpha$H in suspension was 2x10$^{-5}$M. In the same way, a series of suspensions of TTM-$\alpha$H doped with **PTM** (0.5%, 3%, 6.5%,13%, 26%, 50% in molar ratio) were prepared, following the same experimental routine.

The qualitative control through the naked eye suggests that non big aggregates were formed in any of the suspensions. Also, before the spectroscopic characterization a qualative control of luminescence under excitation with UV lamp was performed. Under excitation with UV light **TTMd-ONPs** display an intense orange emission , while the luminescence color of **PTMd-ONPs** is more reddish. The emission is strongly quenched in highly doped samples .

### 4.3.2 Morphological characterization of ONPs

The average size of **TTMd-ONPs** and **PTMd-ONPs** and the size distribution in water have been evaluated via DLS measurements (fig.4.8) The colloidal stability of suspensions was evaluated via Z-potential. Dynamic Light Scattering (DLS) and Z-potential measurements were performed at room temperature with a Malvern Nano ZS equipped with a laser at 633 nm.

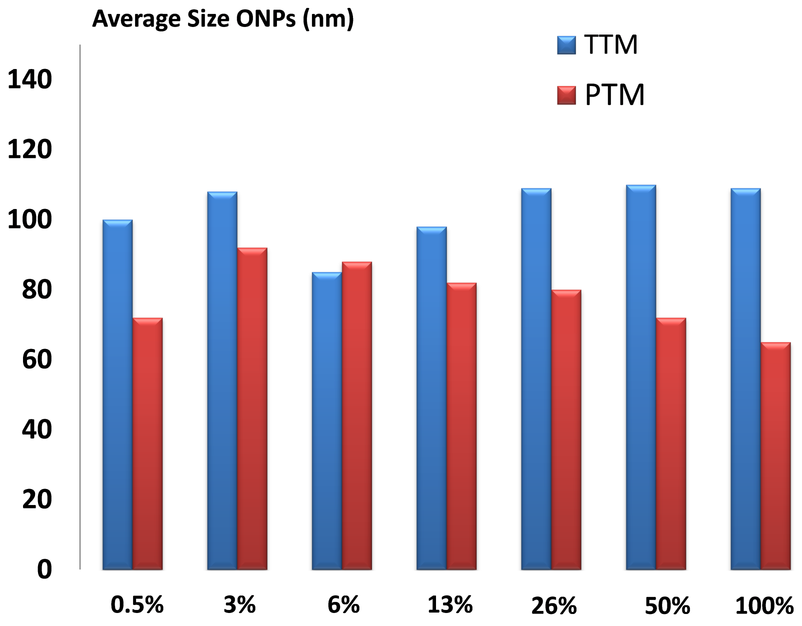

Figure 4.8: Average diameter of **TTMd-ONPs** (blue) and **PTMd-ONPs** (red).

The morphological characterization was completed with TEM images of nanoparticles retrieving their shape and morphology. Samples were observed by a Jeol TEM 1400, operating at an accelerating voltage of 120 kV, using a staining agent (uranyl acetate) to enhance the contrast in image. One drop of each sample was applied to glow-discharged carbon-coated copper grids (SPI) with a plasma treatment, for 3 min. Subsequently, one drop of 2% uranyl acetate was placed on the grid for 1-2 min before being drained off. Images were acquired using an Orius SC200 (Gatan) and are provided in fig.4.9.

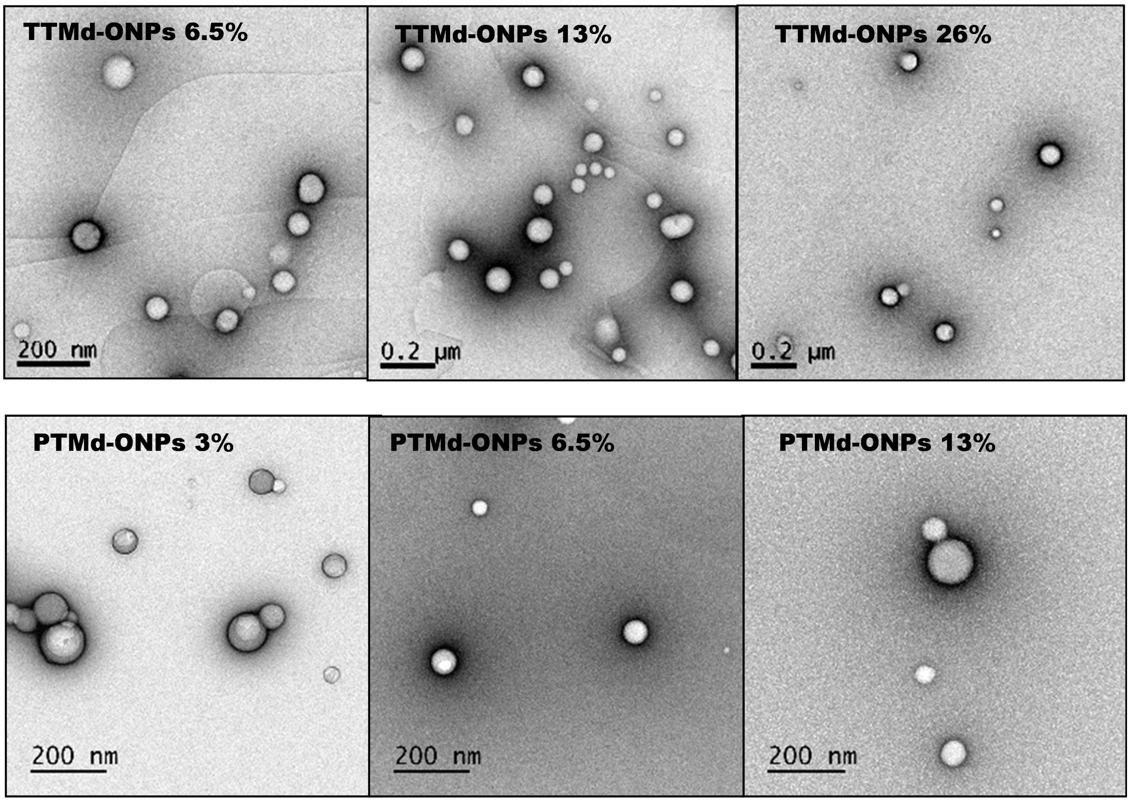

Figure 4.9: (up) TEM images of **TTMd-ONPs** , (bottom) TEM images of **PTMd-ONPs**.

All morphologic characteristics defined via DLS and Zeta pontential are collected in table 4.2. The histogram in fig.4.8 report the average diameters of **TTMd-ONPs** and **PTMd-ONPs** estimated via DLS. **TTMd-ONPs** show average diameters around 100 nm with a polydispersity index lower than 0.22. Transmission electron microscopy images (fig.4.9-up) confirm the results obtained via DLS and show the spherical morphology of the obtained ONPs. Z-potential measurements give for all the samples negative surface potential values around -40 mV, which are sufficient to ensure a good colloidal stability of the obtained ONPs aqueous suspensions. **PTMd-ONPs** show average diameters slightly smaller compared to **TTMd-ONPs**, around 80 nm and similar polydispersity . The Z-potential values (-45mV) are even more negative than **TTMd-ONPs** indicate high colloidal stability for **PTM** suspensions.

Table 4.2: Morphologic Characteristics of **TTMd-ONPs** and **PTMd-ONPs**.

| Sample | Aver. Diam.(nm)[a] | PDI [b] | Z-potential (mV) |
|---|---|---|---|
| **TTMd-ONPs** | | | |
| 0.5% | 100 | 0.19 | -44 |
| 3% | 108 | 0.18 | -42 |
| 6.5% | 85 | 0.18 | -36 |
| 13% | 98 | 0.22 | -40 |
| 26% | 109 | 0.17 | -44 |
| 50% | 110 | 0.20 | -41 |
| **PTMd-ONPs** | | | |
| 0.5% | 72 | 0.17 | -43 |
| 3% | 92 | 0.16 | -45 |
| 6.5% | 88 | 0.20 | -42 |
| 13% | 82 | 0.22 | -45 |
| 26% | 79 | 0.20 | -43 |
| 50% | 81 | 0.19 | -42 |

[a] The average diameter defined via Dynamic Light Scattering.

[b] Polydispersity Index is the normalized second cumulant defined from the polynomial fitting parameters. For a Gaussian size distribution is equal to $(\frac{width}{mean})^2$ : $PDI < 0,2$ monodispersed system, $PDI > 0,2$ polydispersed system

### 4.3.3 Linear Optical Properties of ONPs

Absorption properties of **TTMd-ONPs** and **PTMd-ONPs** are quite similar to the ones measured in solution, in terms of position and shape of the bands. However, the size of the ONPs determines a strong scattering, particularly at wavelength shorter than 400 nm, due to the comparable size of the dispersed nanoparticles. Correcting the absorption spectra for the scattering contribution was possible, using a suspension of pure TTM-$\alpha$H nanoparticles with similar size and size distribution as a reference.

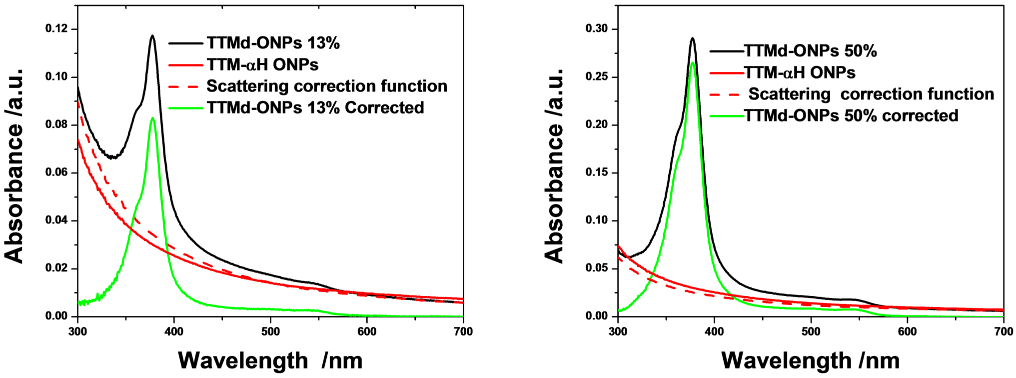

Figure 4.10: Absorbance correction of the 13% and 50% **TTMd-ONPs** samples. Recorded spectrum of **TTMd-ONPs** (black); recorded spectrum of TTM-$\alpha$H ONPs (red); scattering-correction fitting curve (dashed-red); absorption spectrum of **TTMd-ONPs** after correction (green).

This method allows a good estimation of the absorbance, in particular for highly-doped samples. In fig.4.10 are reported two examples of correction of **TTMd-ONPs** suspensions. The correction have been performed for all ONPs and the corrected absorption spectra of **TTMd-ONPs** and **PTMd-ONPs** are reported in fig.4.11.

**Luminescence of TTMd-ONPs** Luminescence spectra of **TTMd-ONPs** suspensions are reported in fig.4.12. The good evaluation of absorbance allows a reliable estimation of LQY. The LQY of the **TTM-ONPs** with low radical doping is strongly improved with respect to the solution. Also not considering the 0.5% **TTMd-ONPs** sample, where the error on the absorbance determination (due to scattering correction) could be significant, it is clear that a rigid environment strongly enhances the emission efficiency giving, at room temperature, values of LQY 10 times higher than in solution.

Table 4.3: Spectroscopic Characteristics of **TTMd-ONPs** and **PTMd-ONPs**.

| Sample | Doping (%mol) | $\lambda_{Abs}$ max (nm) | $\lambda_{Em}$ max (nm) | LQY[a] |
|---|---|---|---|---|
| **TTMd-ONPs** | 0.5% | 380 | 565 | 0.25 |
| | 3% | 380 | 567 | 0.19 |
| | 6.5% | 380 | 567/645 | 0.16 |
| | 13% | 380 | 567/655 | 0.13 |
| | 26% | 380 | 572/665 | 0.07 |
| | 50% | 380 | 685 | 0.02 |
| **PTMd-ONPs** | 0.5% | 390 | 604 | 0.39 |
| | 3% | 390 | 608 | 0.34 |
| | 6.5% | 390 | 610 | 0.15 |
| | 13% | 390 | 612 | 0.07 |
| | 26% | 390 | 612 | 0.02 |
| | 50% | 390 | - | - |

[a] Luminescence quantum yield was estimated through the comparative method, using cresyl violet as a reference (LQY$= 0.55$, MeOH).For **TTMd-ONPs** the LQY refers to the total emission, including both emission bands.

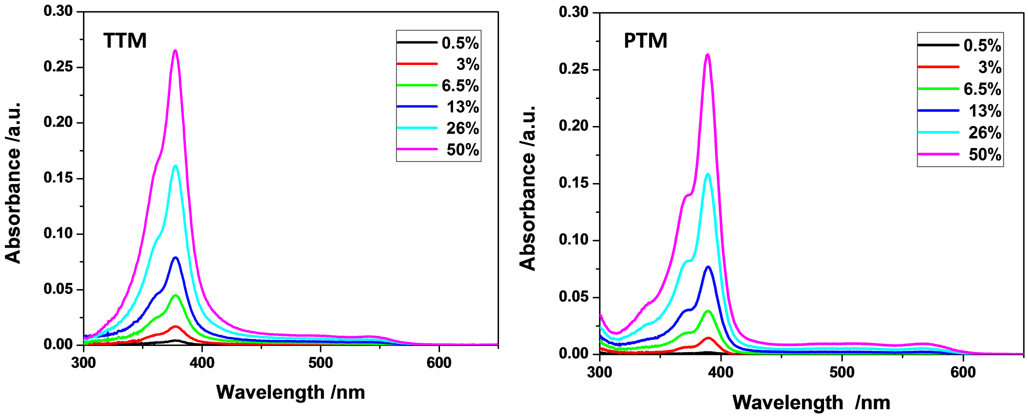

Figure 4.11: UV-vis absorption spectra of **TTMd-ONPs** (left) and **PTMd-ONPs** after scattering correction.

Very interestingly, for percentages of radical-doping equal or higher than 6.5%, dual emission is observed, with a band corresponding to the one observed at lower concentrations, and a new broad and structureless band appearing at longer wavelengths, with a maximum shifting from 645 to 685 nm with increasing radical concentration. This latter band acquires relative intensity with respect to the other one with increasing percentage of radical-doping, while the total LQY decreases. Self-absorption effects can be ruled out both for the short-wavelength emission band (for these radicals the $D_0$-$D_1$, HOMO-SUMO, transition is almost symmetry-forbidden, with molar absorptivity values lower than 1000 $cm^{-1}M^{-1}$) and for the long-wavelength emission band (the samples do not absorb at all in that spectral region).

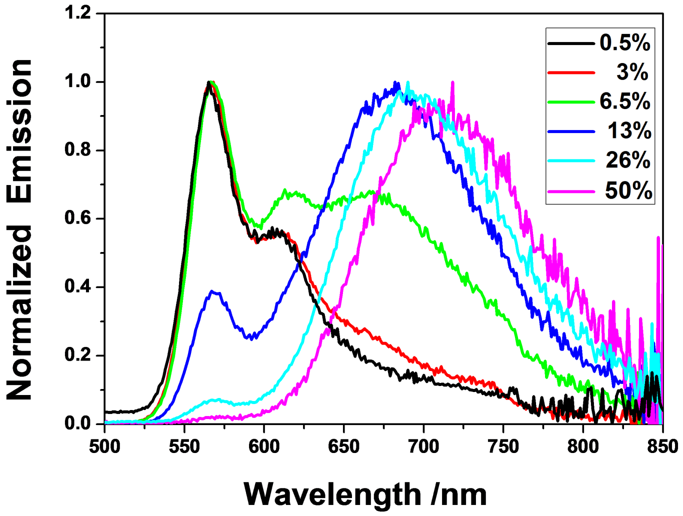

Figure 4.12: Normalized Emission spectra of **TTMd-ONPs in aqueous suspension**

The long-wavelength emission band can be safely ascribed to the formation of excimers of **TTM** radicals inside the host ONPs. In fact, the absorption spectrum is not affected by the concentration of dopant, suggesting a non-interacting ground state, while only emission is affected, as typical of excimers [48, 112]. Moreover, the excitation profile is the same when detecting luminescence on one emission band or the other (fig.4.13): this clearly demonstrates that the ground state is dissociated while the excited state can be monomer-like or excimer-like. The excimer is of the "preformed" (or incipient) type [113], since diffusion is hindered by the rigid matrix, so that the interacting molecules must already be close before excitation, even if the interaction turns on only when one of the molecules in the dimer is excited.

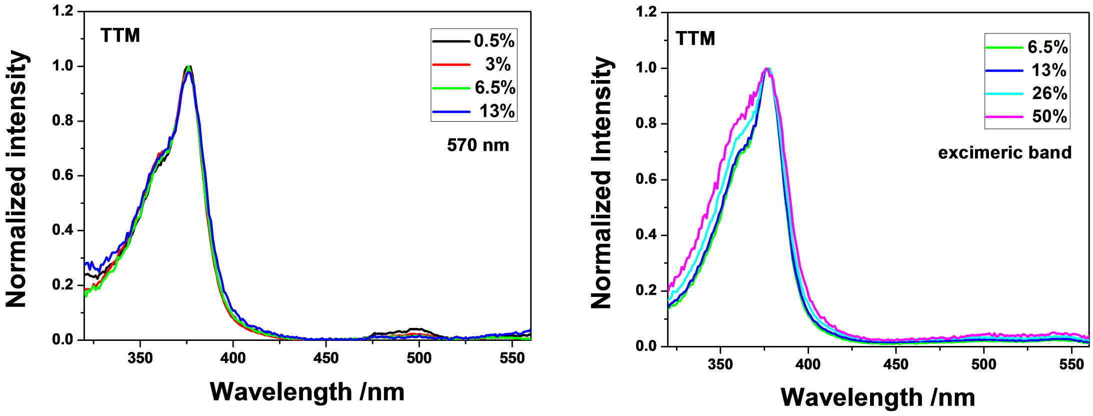

Figure 4.13: Normalized fluorescence excitation spectra of **TTMd-ONPs** registered for emission wavelength fixed at the maximum of the monomer-like emission (left) or at the maximum of the excimer emission (right).

**Luminescence of PTMd-ONPs** The emission characteristics of **PTMd-OPNs** show similarities with respect to **TTMd-ONPs**. The LQY of the **PTMd-ONPs** with low radical doping increases more than 15 times with respect to the solution, while increasing the dopant concentration luminescence is progressively quenched (table 4.3). We observe a slight shift to the red for increasing the doping, but in this case, we do not have strong evidence of the formation of excimers (fig.4.14).

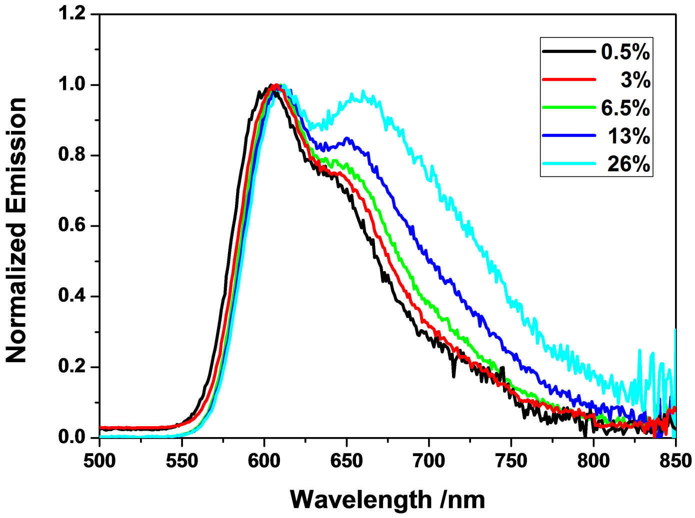

Figure 4.14: Normalized Emission spectra of **PTMd-ONPs in aqueous suspension**

### 4.3.4 PMMA thin films doped with TTM

In order to study the role of the host matrix in the luminescence behaviour and excimer formation and figure out the possibility to use these radical-based luminescent materials for optoelectronic devices, **TTM**-doped PMMA films were prepared. Films were obtained via drop-casting of a TTM/PMMA solution on quartz substrates.

For the preparation of films, PMMA (m.w.=960000) was dissolved in chloroform together with different amounts of **TTM** radical. Polymeric films with 1% ,5%, 10%, 15%, and 20% (wt%) concentration of **TTM** were prepared. For the deposition, 80 microlitres of the stock solution were drop-casted on a quartz substrate. When the solution was dry, films were stabilized under vacuum for 4h.

The estimation of LQY in thin films is a more complex procedure than for solution. To get reliable results, we used an integrating sphere (Quanta-Φ), mounted in fluorometer, to determine the absolute value of LQY (see Appendix 2) [114]. Moreover, a low-pass filter at 476 nm was applied in the emission path during recording. A thin film of pure PMMA was used as the scattering reference.

The normalized luminescence spectra of the **TTMd-PMMA** films are reported in Fig.4.15 and the spectroscopic characteristics are summarized in Table 4.4.

Table 4.4: Spectroscopic Characteristics of **TTMd-PMMA** films .

| TTMd-PMMA (wt%) | $\lambda_{Abs}$ max (nm) | $\lambda_{Em}$ max (nm) | LQY[a] |
|---|---|---|---|
| 1% | 375 | 566 | 0.26 |
| 5% | 375 | 575 | 0.09 |
| 10% | 375 | 574/732 | 0.04 |
| 15% | 375 | 572/732 | 0.03 |
| 20% | 375 | 572/736 | 0.02 |

[a] LQY was measured by an integrating sphere, following the standard method.The LQY refers to the total emission, including both emission bands.

The luminescence behaviour is qualitatively similar to what observed for **TTMd-ONPs**, with a monomer-like emission for low radical concentration and a dual emission starting from 10% radical doping amount. For increasing radical concentration, the relative intensity of the excimer emission increases, while the total LQY is strongly quenched. The excimer emission is centred approximately at 735 nm, i.e. even more to the red with respect to the excimer emission observed for the **TTMd-ONPs**, and no emission shift with the concentration is observed.

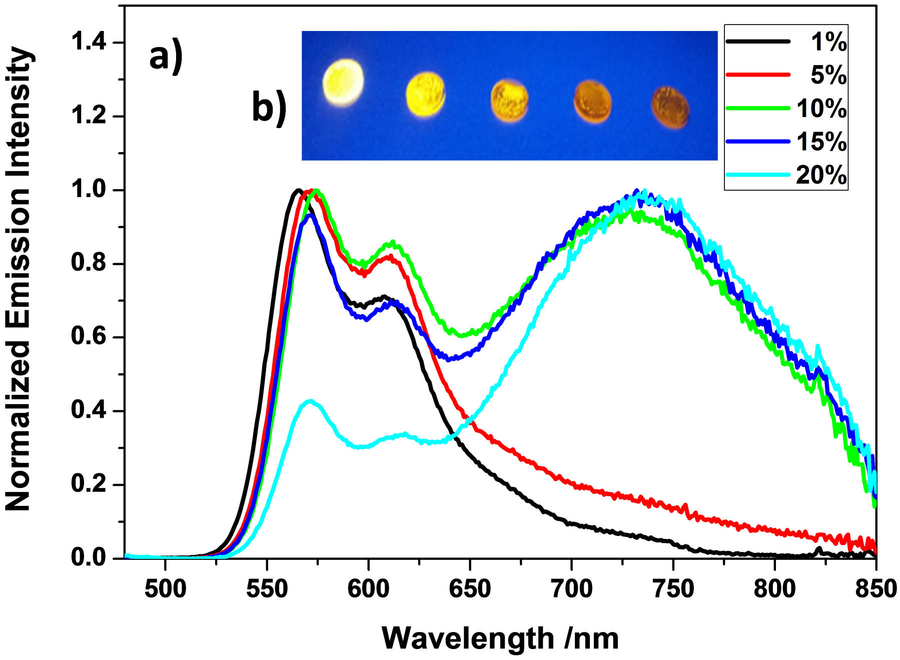

Figure 4.15: a) Normalized emission spectra of **TTMd-PMMA** films with different concentrations of radical. Inset (b): image of the films under 365 nm illumination (radical concentration increasing from left to right).

Although an excimeric emission is observed both in ONPs and in films for high enough radical doping, the position of this emission band and its evolution with the radical concentration are different for the two matrices. In particular, the PMMA doped films show a more red-shifted excimer emission and the position does not depend on the **TTM** amount, while the excimer emission band of **TTMd-ONPs** shifts to the red for increasing doping. The dependence of the excimer emission on the radical concentration is also different in the two types of samples.

These differences can be connected to the different rigidity of the two matrices. In fact, the rigidity and the size of the environmental cage (the volume in which guest molecules are trapped) play a major role in determining the properties of an excimer [115]. The formation of an excimer requires the presence of a molecular pair that is not favourably interacting in the ground state, but that gains energy once one of the two molecules is excited. Reaching the minimum energy for the excimer implies the relaxation along one or more coordinates, including intermolecular distance (most of all in solution or low-viscosity media), vibrational and conformational modes. Our experimental data suggest that, in a rigid environment as the ONPs, the excimers are trapped in more and more stabilized configurations as the fluorophore concentration increases, with a consequent red-shift of the excimer emission (fig.4.16). Instead, in a less rigid environment, such as the polymeric films, relaxation allows to achieve the minimum energy for the excimer, with a consequent concentration-independent excimer emission located at lower energy (fig.4.16).

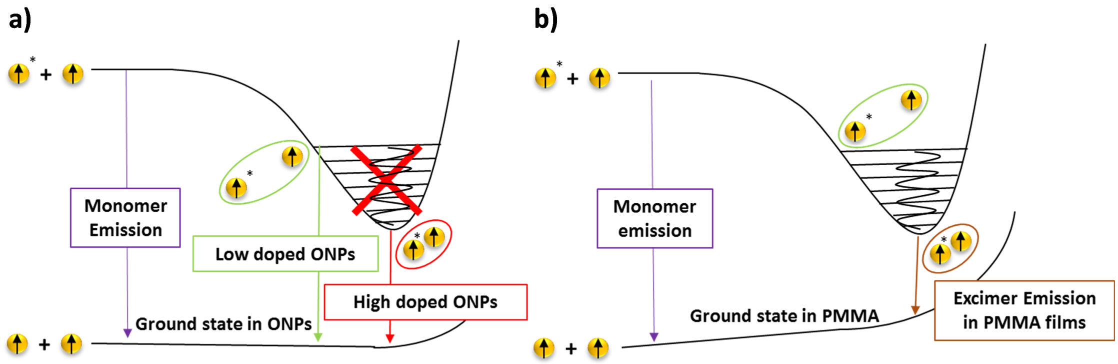

Figure 4.16: The excimer formation in a) **TTMd-ONPs** and b) **TTMd-PMMA** films. The lower monotonous curve represents the repulsive energy between the two molecules in the ground state. The upper curve, which is relative to two molecules, one being in the ground state and the other in the excited state, exhibits a minimum corresponding to the optimum formation of the excimer. In ONPs, the exciton is trapped in more and more stabilized excimer configurations as the radical amount increases. In films the conformational relaxation allows the excimer to achieve the most stable configuration, independently of the concentration.

### 4.3.5 Luminescence Lifetime Decay Analysis

Luminescence lifetime decays were measured under excitation with NanoLed@370nm adjusted to the magic angle configuration. Two polarizers were applied in excitation and emission paths respectively to reduce the scattering. The emission decays measured for the ONPs and thin films could not be fitted via single-exponential functions, but at least three exponentials were needed.

Since no direct physical meaning could be associated to the three-exponential fitting, we also performed fittings through a more meaningful function, namely the so-called stretched-exponential function [116], also known as the Kohlraush-Williams-

Watts (KWW) decay function (Appendix 3):

$$I(t) = I_o exp[-(t/\tau_o)^{\beta}] \tag{4.1}$$

where $\tau_0$ is the relaxation time and $\beta$ is the stretch factor, ranging from 0 to 1. The closer the $\beta$ value is to 0 the more the function deviates from a single exponential. The stretched-exponential function is suitable whenever a distribution of decay times or rate constants is expected, as in heterogeneous samples showing continuous lifetime distributions (rigid solutions, samples where energy transfer among like or unlike fluorophores occurs, and so on) [117, 118]. In particular, the stretched-exponential decay model can provide a direct measure of the heterogeneity of the sample. Typically the parameter $h = \frac{1}{\beta}$ is introduced, so that $h$ increases when the heterogeneity degree increases ($\beta$ approaching 0). All the luminescence decays were fitted through the stretched-exponential function and the results are reported in tables 4.5 and 4.6. The average time constants were obtained as:

$$< \tau >= \tau_o \Gamma(1 + 1/\beta) \tag{4.2}$$

where $\Gamma$ indicates the Gamma function:

$$\Gamma(z) = \int_0^{\infty} x^{z-1} e^x dx \tag{4.3}$$

**TTMd-ONPS** The luminescence decays of momomeric and excimeric bands and the stretched exponential fitting curves are provided in fig.4.17 and fig.4.18 respectively. The average emission lifetimes (table 4.5) for the **TTM-doped** ONPs are always longer than the lifetime obtained in THF solution. In particular, the 0.5% **TTMd-ONPs** have a lifetime of about 220 ns, that is more than one order of magnitude longer than the

**TTM** radical in THF solution (∼10 ns). Increasing the concentration of **TTM**, we observe a decrease of the lifetime associated to the monomer-like emission. This is not surprising, since the increased **TTM** concentration increases the number of aggregates and/or incipient excimers, and hence increases the number of potential quenchers for the monomer [48].

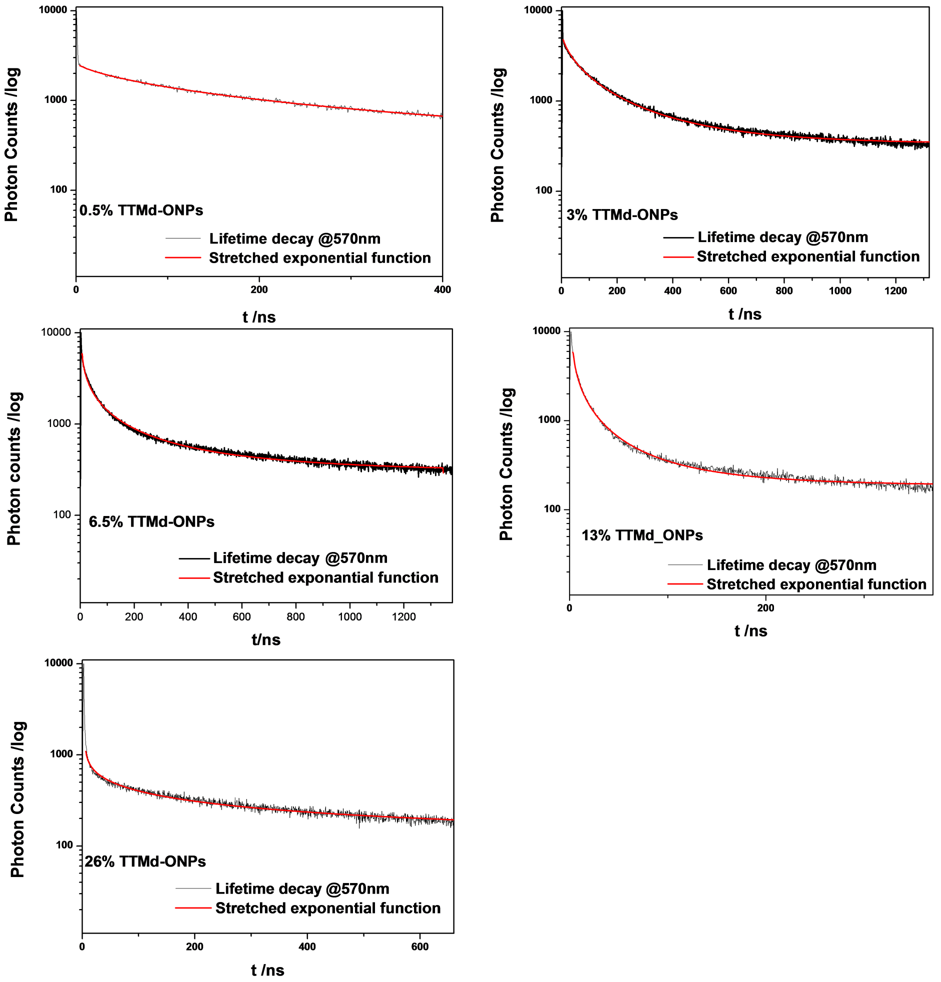

Figure 4.17: Luminescence decays and corresponding stretched-exponential fits for detection in the monomeric band, for **TTMd-ONPs**.

On the contrary, the average lifetime associated to the excimer emission increases slightly more than linearly with the concentration (from ∼100 ns for the 6.5% **TTMd-ONPs** to ∼700 ns for the 26% **TTMd-ONPs**), while a decrease is obtained for the most doped sample (50% **TTMd-ONPs**, but it should be taken into account that this sample is very weakly emitting, with a LQY on the order of 2%)

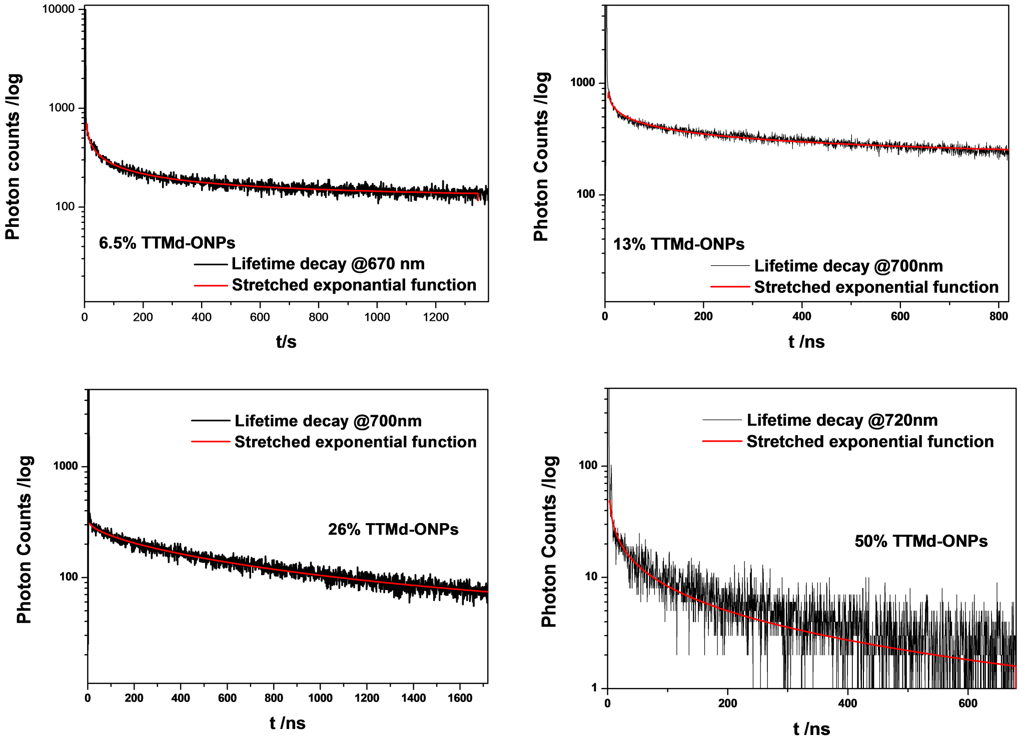

Figure 4.18: Luminescence decays and corresponding stretched-exponential fits for detection in the excimeric band, for **TTMd-ONPs**.

These results can also be discussed in relation to the specific observed intensities of monomer and excimer emission. The monomer's and excimer's emission intensities ($I_M$ and $I_E$, respectively) are given by:

$$I_M \propto n_{abs} k_r \tau_M \tag{4.4}$$

$$I_E \propto n_{abs} f k_r' \tau_E \propto n_{abs} k_E \tau_M k_r' \tau_E \tag{4.5}$$

where $n_{abs}$ is the number of absorbed photons (typically proportional to the fluoro-

Table 4.5: Results of the fitting analysis of the luminescence decays for **TTMd-ONPs** at the emission wavelength of the monomer (M) and/or of the excimer (E).

| | | 3-exponential[a] | | | stretched exponential [b] | | |
|---|---|---|---|---|---|---|---|
| **TTMd-ONPs** (% w/w) | $\lambda^{Em}$ (nm) | $\tau_1$ (s) | $\tau_2$ (s) | $\tau_3$ (s) | $\tau_o$ (s) | $h$ | $<\tau>$ (s) |
| **0.5%** | 570 (M) | $1.5x10^{-7}$<br>(28.67) | $5.6x10^{-7}$<br>(69.63) | $2.2x10^{-8}$<br>(1.7) | $1.5x10^{-7}$ | 1.6 | $2.2x10^{-7}$ |
| **3%** | 570 (M) | $1.1x10^{-7}$<br>(42.80) | $5.0x10^{-7}$<br>(52.91) | $2.2x10^{-8}$<br>(4.29) | $5.7x10^{-8}$ | 1.8 | $9.5x10^{-8}$ |
| **6.5%** | 570 (M) | $4.7x10^{-8}$<br>(33.03) | $4.0x10^{-7}$<br>(63.24) | $1.8x10^{-9}$<br>(3.74) | $1.1x10^{-8}$ | 2.8 | $5.4x10^{-8}$ |
| | 670 (E) | $8.7x10^{-8}$<br>(18.51) | $6.6x10^{-7}$<br>(76.61) | $1.6x10^{-8}$<br>(4.88) | $4.9x10^{-9}$ | 4.0 | $1.1x10^{-7}$ |
| **13%** | 570 (E) | $2.8x10^{-8}$<br>(15.46) | $4.3x10^{-7}$<br>(78.16) | $2.2x10^{-9}$<br>(6.38) | $2.1x10^{-9}$ | 2.6 | $8.1x10^{-9}$ |
| | 670 (E) | $3.9x10^{-8}$<br>(3.17) | $8.1x10^{-7}$<br>(95.84) | $6.8x10^{-9}$<br>(1.00) | $1.3x10^{-8}$ | 4.4 | $5.4x10^{-7}$ |
| **26%** | 570 (M) | $6.0x10^{-8}$<br>(10.85) | $5.1x10^{-7}$<br>(82.94) | $1.0x10^{-9}$<br>(6.21) | $1.6x10^{-9}$ | 3.8 | $3.0x10^{-8}$ |
| | 670 (E) | $1.0x10^{-7}$<br>(4.41) | $8.7x10^{-7}$<br>(95.29) | $3.5x10^{-9}$<br>(0.3) | $5.4x10^{-7}$ | 1.5 | $7.5x10^{-7}$ |
| **50%** | 670 (E) | $6.0x10^{-8}$<br>(6.43) | $9.2x10^{-7}$<br>(91.81) | $4.6x10^{-9}$<br>(1.76) | $1.5x10^{-9}$ | 4.1 | $4.5x10^{-8}$ |

[a] Results of the three-exponential fitting reconvolution fit analysis (corresponding lifetimes $\tau_1$, $\tau_2$, $\tau_3$ and relative amplitudes)

[b] Mean luminescence lifetimes, $\tau$, and heterogeneity factor, $h = \frac{1}{\beta}$ , as estimated through stretched-exponential reconvolution fit analysis of the luminescence decay of the monomer-like (570 nm) or excimer-like (670 nm) emission band. The quality of the fitting was judged by the reduced $\chi^2$ value.

phore concentration);$k_r$ and $k_r'$ are the radiative emission rates of the monomer and of the excimer, respectively; $\tau_M$ and $\tau_E$ are the emission lifetimes associated to the monomer and to the excimer, respectively; f is the fraction of excited monomers converted into excimers. This last factor is given by the ratio between the formation rate of the excimer ($k_E$) and the sum of the rates depopulating the monomer excited state ($\tau_M^{-1}$). In the case of diffusion-driven excimer formation, $k_E$ is usually proportional to the fluorophore concentration, while a very different dependence on concentration can be expected in other cases: for example, in the case of intramolecular excimers (where no translation is needed) $k_E$ can be assumed as independent of the concentration.

Expressions (1) and (2) lead to estimate the excimer/monomer (E/M) emission ratio as:

$$\frac{I_E}{I_M} = \frac{k'_r}{k_r} k_E \tau_E \tag{4.6}$$

In fig.4.19 the emission intensity is reported as normalized with respect to $n_{abs}$ (i.e. to the absorbance of each sample), as to better discuss the non-trivial dependence of the intensities on the fluorophore concentration. $I_M/n_{abs}$ decreases with increasing concentration, suggesting an almost linear decrease of $k_r\ \tau_M$, in agreement with the measured decrease of $\tau_M$. At the same time, $I_E/n_{abs}$ increases (less than linearly) with the concentration up to the 13%-doping: since the decrease in $\tau_M$ roughly compensate the increase of $\tau_E$, the dependence of $I_E/n_{abs}$ on the concentration is mostly governed by $k_E$. The estimated less-than-linear increase of $k_E$ with concentration thus explains the dependence of $I_E/n_{abs}$ on the fluorophore concentration. For higher TTM radical concentration (already starting from the 26% **TTMd-ONPs**) the excimer emission is affected by ACQ, leading to a complete loss of luminescence in the pure **TTM** samples (either powders or ONPs).

In other words, the observed E/M emission ratio increases roughly quadratically with respect to the concentration (at least up to the 26%-doped sample): since a slightly more than linear dependence is accounted for by the excimer lifetime, we expect $k_E$ to increase less than linearly with the fluorophore concentration. This is not surprising, since a linear increase of $k_E$ with the fluorophore concentration is only expected in the case of diffusion-driven excimer formation.

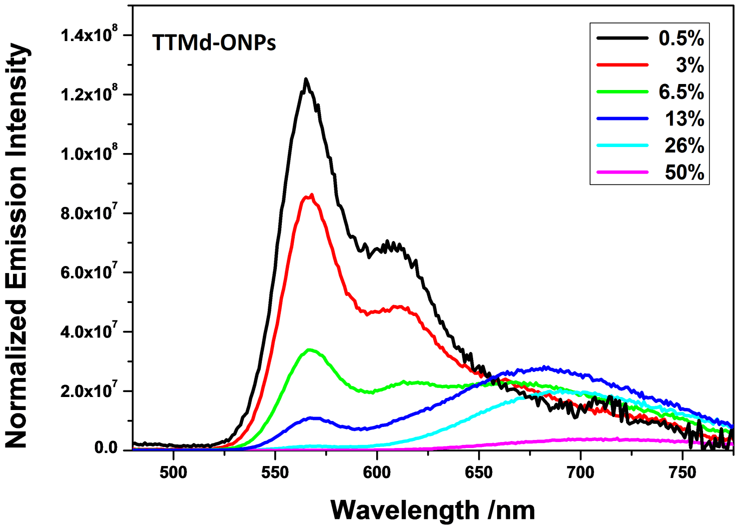

Figure 4.19: Emission spectra of **TTMd-ONPs** . The emission intensity is normalized with respect to absorbance of each sample.

The $h$ value associated to the decay of the monomer-like band increases with increasing radical concentration, suggesting an increased heterogeneity of the monomer-like emissive species for increasing concentration of the emitters themselves. This is consistent with the fact that, for very low radical amount, the emissive radical is mainly surrounded by TTM-$\alpha$H host molecules (low heterogeneity) while, for increasing concentration of radical, each **TTM** molecule can be surrounded by a variable amount of TTM-$\alpha$H host molecules or alike **TTM** radicals (even if weakly interacting), increasing the heterogeneity. The $h$ value associated to the excimer band seems more insensitive to radical concentration, even if a specific trend cannot be recognized (it should be noted, however, that the excimer emission band is partly overlapped to the monomer emission band, so that a contribution from the monomer emission could affect the measured excimer decay).

**PTMd-ONPs** This analysis has been performed for luminescence decays of **PTMd-ONPs** as well. The luminescence lifetime decays were fitted with 3-exponential and stretched-exponential functions. The luminescence decays measurements and the stretched exponential fitting curves are provided in fig.4.20. Table 4.6 collects the fluorescence lifetimes extracted from the 3-exponential fitting analysis, and the mean lifetime and the heterogeneity factor obtained by the stretched exponential fitting. The results indicate very similar behaviour with **TTM** suspensions. Lifetime decays of ONPs are always longer with respect to **PTM** in solution, and increasing the concentration of radical, a decrease of the lifetime of two orders of magnitude is obtained: from 120 ns (0.5% sample) to 6.6 ns (26% sample). Even if no clear evidence of excimer formation is observed in case of **PTMd-ONPs**, the quenching of fluorescence occurs for even lower doping, with complete quench for 50% sample. Consistently with the analysis we performed on **TTM**, a trend is observed about the homogeneity of the ONPs: the *h* factor rises when the doping of radical increases, expressing the changes in the microenvironment of the emitters.

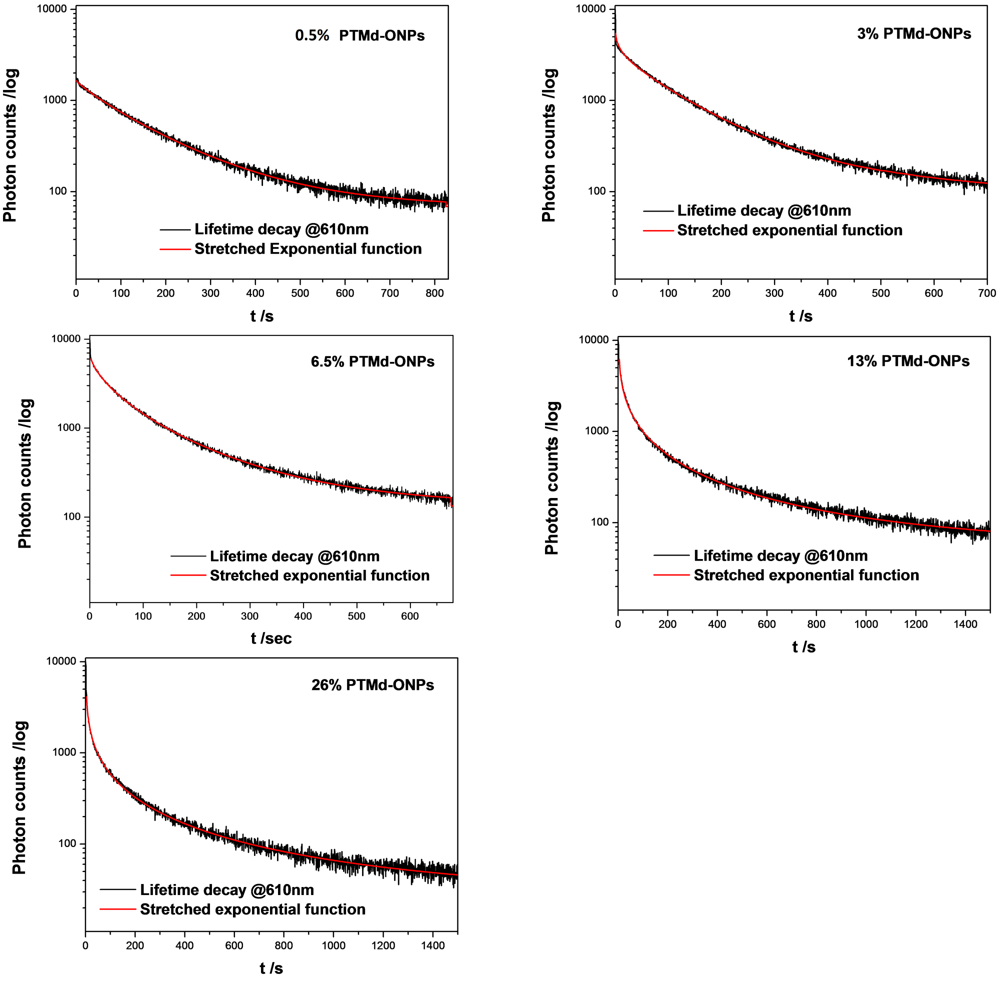

Figure 4.20: Luminescence decays and corresponding stretched-exponential fits for **PTMd-ONPs**.

Table 4.6: Results of the fitting analysis of the luminescence decays for **PTMd-ONPs** at the maximum of emission (610 nm)

| | | 3-exponential[a] | | | stretched exponential [b] | | |
|---|---|---|---|---|---|---|---|
| **PTMd-ONPs** (% w/w) | $\lambda^{Em}$ (nm) | $\tau_1$ (s) | $\tau_2$ (s) | $\tau_3$ (s) | $\tau_o$ (s) | $h$ | <$\tau$> (s) |
| **0.5%** | 610 | $1.7x10^{-7}$<br>(80.04) | $7.6x10^{-8}$<br>(19.41) | $5.1x10^{-9}$<br>(0.55) | $1.2x10^{-7}$ | 1.2 | $1.19x10^{-7}$ |
| **3%** | 610 | $1.0x10^{-7}$<br>(67.06) | $2.7x10^{-8}$<br>(5.59) | $4.5x10^{-7}$<br>(27.04) | $7.3x10^{-8}$ | 1.6 | $1.07x10^{-7}$ |
| **6.5%** | 610 | $6.3x10^{-8}$<br>(51.42) | $3.3x10^{-7}$<br>(45.48) | $1.4x10^{-9}$<br>(3.1) | $4.5x10^{-8}$ | 1.6 | $3.12x10^{-8}$ |
| **13%** | 610 | $2.8x10^{-8}$<br>(30.68) | $1.9x10^{-7}$<br>(64.68) | $1.7x10^{-9}$<br>(5.17) | $4.1x10^{-9}$ | 3.3 | $2.27x10^{-8}$ |
| **26%** | 610 | $3.7x10^{-8}$<br>(27.78) | $2.7x10^{-7}$<br>(60.01) | $2.6x10^{-9}$<br>(12.21) | $6.6x10^{-9}$ | 3.1 | $1.73x10^{-8}$ |
| **50%** | 610 | ND | ND | ND | ND | ND | ND |

ND very weak fluorescence signal

[a] Results of the three-exponential fitting reconvolution fit analysis (corresponding lifetimes $\tau_1$, $\tau_2$, $\tau_3$ and relative amplitudes)

[b] /[c] Mean luminescence lifetimes, <$\tau$>, and heterogeneity factor, $h = \frac{1}{\beta}$ , as estimated through stretched-exponential reconvolution fit analysis. The quality of the fitting was judged by the reduced $\chi^2$ value.

**TTM-doped thin films** As in the case of radical-doped ONPs, luminescence decays could be fitted via either three-exponential or stretched-exponential functions. The average time constants extracted from the stretched-exponential fittings are reported in table 4.7, together with the values of the *h* parameter. The behaviour is similar to what reported for radical-doped ONPs: the lifetime associated to the monomer-like emission is lower than in ONPs but decreases for increasing doping, while the lifetime associated to the excimer emission has a non-monotonic trend.

Analogously, the *h* parameter relative to the monomer-like species increases for increasing doping concentration, while the *h* parameter associated to the excimer behaves non-monotonically. The qualitative (and almost quantitative) similarity with doped-ONPs is impressive, suggesting that the nature of the matrix (small organic molecule vs polymer) does not strongly influence the degree of heterogeneity of the sample.

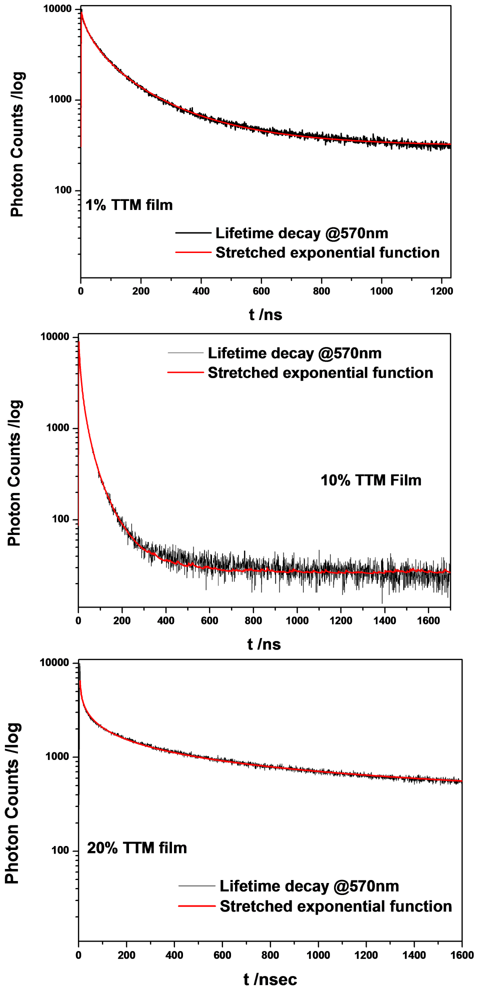

Figure 4.21: Luminescence decays and corresponding stretched-exponential fits for detection in the monomeric band, for **TTM-doped** thin films.

The E/M emission ratio increases roughly linearly with the concentration, suggesting an excimer formation rate barely dependent on the concentration itself. Consistently, $I_E/n_{abs}$ barely depends on the **TTM** concentration (fig.4.23).

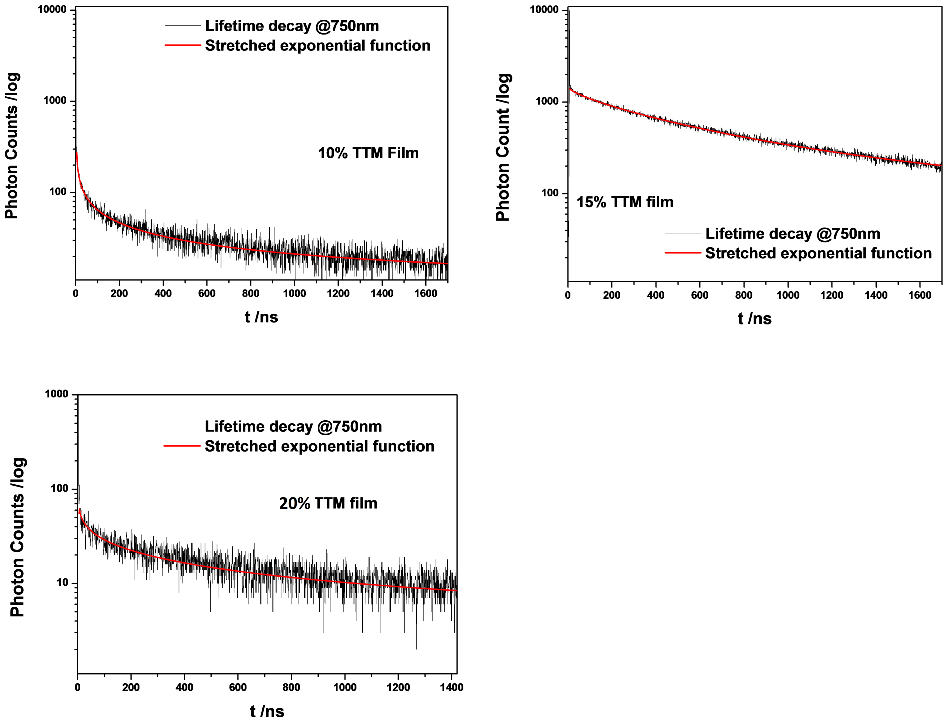

Figure 4.22: Luminescence decays and corresponding stretched-exponential fits for detection of excimeric band, for **TTM-doped PMMA** thin films.

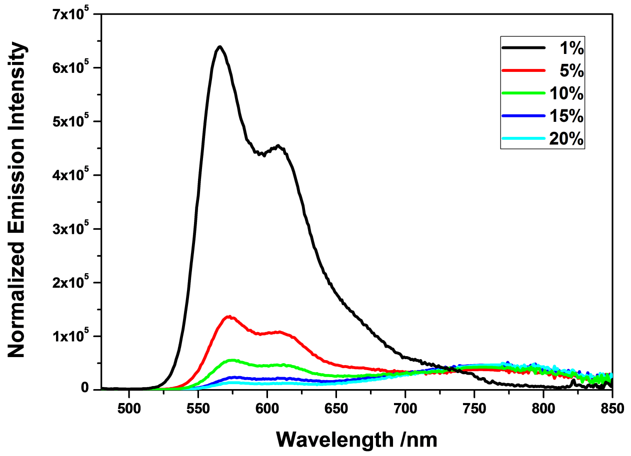

Figure 4.23: Emission spectra of **TTMd-PMMA** thin films . The emission intensity is normalized with respect to absorbance of each sample.

Table 4.7: Results of the fitting analysis of the luminescence decays of the **TTMd-PMMA** thin films at the emission wavelength of the monomer (M) and/or of the excimer (E).

| | | 3-exponential[a] | | | stretched exponential [b] | | |
|---|---|---|---|---|---|---|---|
| TTM films | $\lambda^{Em}$ (nm) | $\tau_1$ (s) | $\tau_2$ (s) | $\tau_3$ (s) | $\tau_o$ (s) | $h$ | <$\tau$> (s) |
| **1%** | 570 (M) | $1.5x10^{-8}$<br>(5.91) | $9.1x10^{-8}$<br>(50.73) | $3.7x10^{-7}$<br>(6.86) | $4.52x10^{-8}$ | 1.8 | $7.5x10^{-8}$ |
| **5%** | 570 (M) | $5.7x10^{-8}$<br>(26.05) | $4.8x10^{-7}$<br>(66.78) | $8.1x10^{-9}$<br>(7.17) | $1.9x10^{-8}$ | 1.9 | $3.6x10^{-8}$ |
| **10%** | 570 (M) | $2.3x10^{-8}$<br>(52.60) | $8.5x10^{-8}$<br>(30.50) | $4.0x10^{-9}$<br>(16.9) | $3.5x10^{-9}$ | 2.3 | $9.5x10^{-9}$ |
| | 750 (E) | $8.7x10^{-8}$<br>(17.12) | $5.8x10^{-7}$<br>(76.45) | $1.1x10^{-8}$<br>(6.43) | $3.3x10^{-11}$ | 6.6 | $8.0x10^{-8}$ |
| **15%** | 570 (E) | $1.9x10^{-8}$<br>(36.91) | $2.1x10^{-7}$<br>(48.86) | $3.4x10^{-9}$<br>(14.24) | $2.2x10^{-11}$ | 6.1 | $1.8x10^{-8}$ |
| | 750(E) | $1.8x10^{-7}$<br>(8.92) | $8.2x10^{-7}$<br>(90.76) | $1.1x10^{-8}$<br>(0.32) | $5.0x10^{-7}$ | 1.3 | $5.9x10^{-7}$ |
| **20%** | 570 (M) | $6.0x10^{-8}$<br>(10.85) | $5.1x10^{-7}$<br>(82.94) | $1.0x10^{-9}$<br>(6.21) | $7.2x10^{-9}$ | 4.2 | $2.5x10^{-7}$ |
| | 750(E) | $5.3x10^{-9}$<br>(1.22) | $6.2x10^{-7}$<br>(87.38) | $2.0x10^{-7}$<br>(11.40) | $6.3x10^{-8}$ | 3.4 | $4.6x10^{-7}$ |

[a] Results of the three-exponential fitting reconvolution fit analysis (corresponding lifetimes $\tau_1$, $\tau_2$, $\tau_3$ and relative amplitudes)

[b] Mean luminescence lifetimes, $\tau$, and heterogeneity factor, $h = \frac{1}{\beta}$ , as estimated through stretched-exponential reconvolution fit analysis of the luminescence decay of the monomer-like (570 nm) or excimer-like (670 nm) emission band. The quality of the fitting was judged by the reduced $\chi^2$ value.

### 4.3.6 Photostability of TTMd-ONPs

The rigid environment offered by the TTM-$\alpha$H matrix not only helps to obtain good luminescence properties but, thanks to its shielding effect, also contributes to increase the radical photostability, preventing photodegradation processes. The emission intensities of monomeric and excimeric bands of deoxygenated 13% **TTMd-ONPs** aqueous suspension were measured as a function of time under continuous irradiation at 375 nm, in order to estimate the photobleaching rate. The results were compared with **TTM** deoxygenated solution in THF . The decay of the monomer-like band is characterized by two components: the first one dominating up to 400 s, which matches the decay of

**TTM** in solution, and a second, slower one, sensibly contributing at longer times.

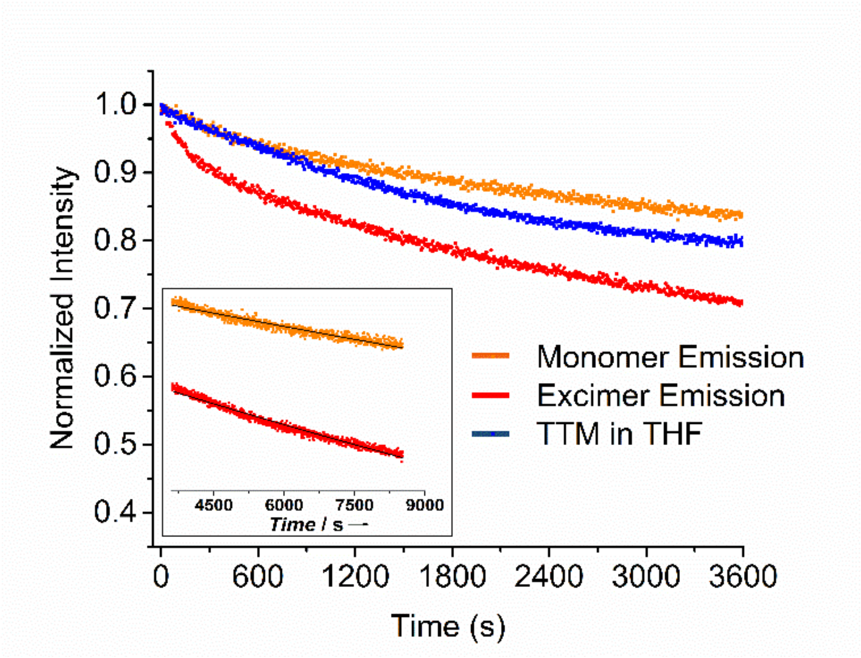

Figure 4.24: Luminescence decay of **TTM** in THF solution (blue points) and 13% **TTMd-ONPs** water suspension (monomer-like emission band, orange points, excimer emission band, red points) under continuous irradiation at 375 nm. Inset: luminescence decays of monomeric and excimeric bands of 13% **TTMd-ONPs** for time > 1h, together with the corresponding monoexponential fitting curves (black lines)

Two components can be recognized also in the decay of the excimeric band, but in this case the photobleaching is faster than for **TTM** in solution, as expected for a dimeric species. The two components in the photobleaching process in ONPs could be due to the different environment experienced by **TTM** molecules on the surface of ONPs with respect to **TTM** molecules in the inner part of ONPs: more exposed and less hindered the former (leading to faster photodegradation), while completely surrounded by host molecules the latter (leading to slower photodegradation). The decay curves for times longer than 1 hour (i.e. minimizing the effect of the faster photodegradation ascribed to the surface effect) were fitted through mono-exponential curves (inset fig.4.24). The time constant extracted for the monomer-like emission (6.05x$10^5$s) is about twice the time constant estimated for the excimer emission (3.16x$10^5$s), confirming the dimeric nature of the species emitting at long wavelengths.

## 4.4 Two-Photon Absorption of PTM and TTM

Due to their possible two-photon excitation and their emission in the spectral range where biological tissue are optical transparent, the two-photon absorption cross sections of **PTM** and **TTM** were determined. The two-photon absorption cross section was measured via the two-photon excitation spectra, for the molecules in THF. The output of a TOPAS-Prime in combination with a NIRUVis frequency mixer (both from Light Conversion) was used as excitation source. The excitation intensity was adjusted using a combination of a broadband zero-order halfwaveplate and a Glan-Taylor polarizer set in vertical polarization. The beam was focused on sample by a lens of focal length 40 mm. The pump power was monitored using a powermeter (Thorlabs PM100A) equipped with a thermal sensor. The fluorescence was focused onto the entrance slit of a monochromator (0.25 Cornerstone, Oriel, grating 74166 Newport) equipped with a multi-pixel photon-counter avalanche photodiode detector. The output signal was preamplified. The power dependence of the fluorescence intensity was monitored throughout the measurement.

This measurement gives the action two-photon absorption cross section ($\sigma_2\Phi$) at different excitation wavelengths and then the corresponding two photon absorption cross section ($\sigma_2$) can be extracted (fig.4.25). Due to the high concentration of the solutions (needed in order to get enough signal) aggregation effects cannot be excluded, so that the results could represent effective 2PA responses.

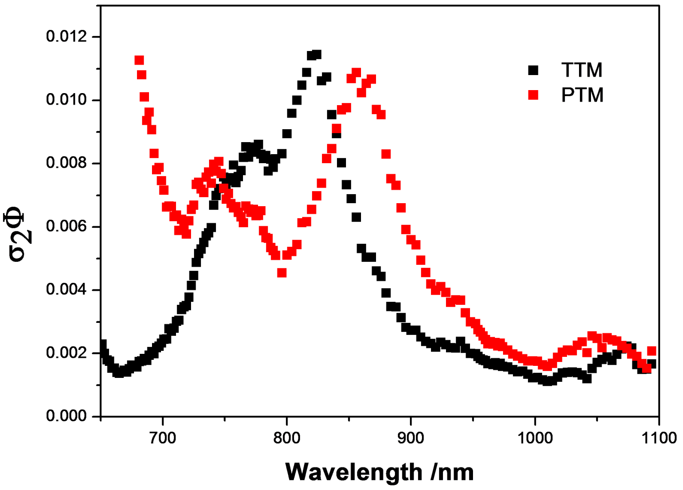

Figure 4.25: Action two photon absorption cross section of **PTM** and **TTM** in THF. 1 GM=$10^{-50} cm^4 s$

Table 4.8: Two-photon excitation characteristics of **TTM** and **PTM** in THF.

| Sample | Solvent | $\lambda_{1PAbs}$ max (nm) | $\lambda_{2PAbs}$ max (nm) | $\sigma_2^{max}\Phi$[a] |
|---|---|---|---|---|
| **TTM** | THF | 373 | 824 | 0.012 |
| **PTM** | THF | 385 | 856 | 0.011 |

[a] Rhodamine 6G used as a reference.

As shown in figure 4.25 **TTM** and **PTM** in organic solvent exhibit a broad two-photon response in the whole 700-1000 nm spectral region. **TTM** displays a broad two-photon absorption band with a maximum at 830 nm and a shoulder at 790 nm. **PTM** displays two bands, one located at 860-870 nm and a second at 730 nm. In fig.4.26 the TPA spectra are compared with the rescaled linear absorption spectra.

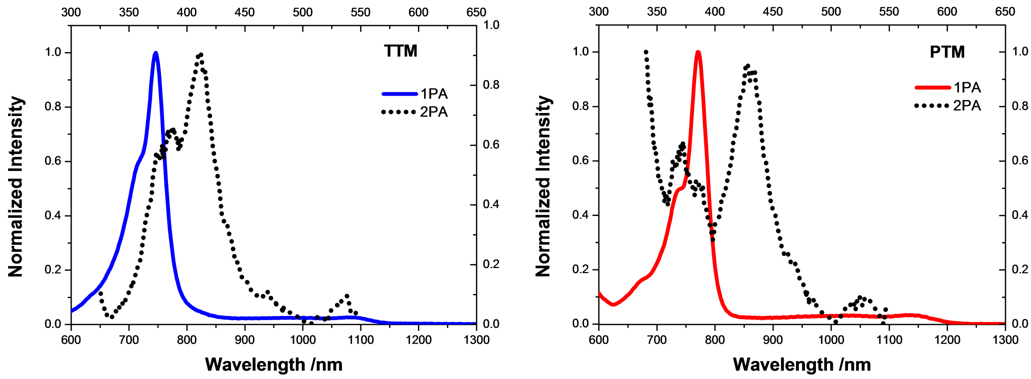

Figure 4.26: Normalized one and two photon excitation profiles of **TTM** and **PTM** in THF.

Experiment for the determination of the two-photon absorption cross section have also been performed for nanoparticle suspension, but no significant signal could be detected. The main limiting factor was the significant low concetration of the radical in nanoparticle, which was not sufficient to obtain a good signal induced by the two photon process. Typically, the concentration of dyes in these types measurements is an order of $10^{-4}$M or higher. In the case of radical-doped nanoparticles with low concentration of radical (0,5%) we have highly LQY but small amount of emitting spieces, while high doped samples lack fluorescence. Z-scan could be an alternative method, because it allows the determination of two-photon cross section of non-fluorescent materials.

## 4.5 Conclusions

In this chapter the luminescence properties of new materials based on carbon-centered radicals, namely polychlorotriphenylmethyl radicals were studied. Aggregation and medium effects were exploited, in order to improve the fluorescence and photostability of these materials. Particularly, we demonstrated the possibility to obtain ONPs and polymeric films doped with **TTM** and **PTM**, characterised by good luminescence quantum yields and long lifetimes, together with an improved photostability.

In case of samples doped with **TTM** (ONPs and films) an interesting trend is obtained: as radical concentration increases, a red-shifted, broad and structureless emission band appears, safely attributed to excimers of the **TTM** radical. In both systems, the lifetime associated to the excimer emission is close to the $\mu$s timescale, suggesting an almost spin-forbidden emission transition for the excimer species as due, for example, to triplet radical-pairs. In order to validate this hypothesis, further experiments on photo and electro luminescence under magnetic field are in progress.

These excimers, observed for the first time in the case of persistent free-radicals, are promising for bioimaging applications as well as for the fabrication of OLEDs with high internal quantum efficiency. Specifically, the **TTM**-doped ONPs allow to overcome the drawback of water solubility of TTM and increase its biocompatibility [119], constituting a good example of nano-bioprobes [120].

The two-photon absorption cross section of **TTM** and **PTM** radicals in solution has been measured, covering the 700-1000 nm spectral region. The peculiar electronic structure of the photoactive radicals provides a perfect scenario for both two-photon excitation and luminescence inside the so-called biological transparency window (namely between 700 and 1500 nm), most of all if the excimer emission was exploited.

Similarly, the radical-doped polymeric films could be exploited for novel optoelectronic applications, in particular in WOLEDs fabrication, in which blue emitting host materials are doped with low amount of orange-red emitting guest. In this context, the good LQY, the high chemical-photochemical stability offered by the rigid environment, the possibility to cover a wide part of the visible range thanks to the excimer formation and the doublet nature of the emitters, make polychlorotriphenylmethyl radicals a suitable alternative to heavy-metal complexes [121].

# Chapter 5

# Two-Photon Polymerization

This chapter is divided into two parts: the first section is devoted to a method for monitoring the photo-polymerization process through fluorescence technique, and in the second part the synthesis of a non-linear aldehyde as a photo-initiator for 2-photon polymerization is described.

## 5.1 Monitoring the Photo-polymerization via Fluorescence Spectroscopy

Fluorescence is a highly sensitive technique, that is widely used as a tool of investigation, analysis and control in many fields relevant to physical, chemical, biological and material sciences. Fluorescent labelling [122], dyes [123], biological detectors [124], microscopy [125], fluorescent lamps [126] are some of the most common applications.

In polymer science fluorescence spectroscopy has become a powerful tool to monitor microscopic changes in polymer systems. The processes that could take place in a polymeric material are diverse, such as chemical reactions, photodegradation, thermal transitions and so on [127], [128]. One of the most studied processes in polymers with fluorescence is the photo-polymerization reaction. This is due to several advantages of fluorescence:

- High sensitivity and selectivity
- Non-destructive technique
- In situ and real time monitoring of photo-polymerization

A drawback is that intrinsic fluorescence of polymeric materials is usually weak and the evolution of the process cannot be followed. Therefore, the addition of a fluorescent molecule that can give information about the processes is required [129]. Fluorescence Probe Techniques (FPT) [130] used to measure fluorescence changes of probes include steady state, anisotropy and time-resolved measurements. Usually the parameters to correlate with changes in the medium are: maximum emission wavelength, fluorescence intensity ratio between two wavelengths, fluorescence lifetimes, monomer/excimer ratio.

Here, we investigated the photo-polymerization of a commercially available polymer, namely **E-Shell 300** doped with three different dyes. **Coumarin 153**, **Coumarin 334** and a non-commercially available dye, namely **MBQ** (fig.5.1) have been selected according to their spectroscopic characteristics and their solubility in **E-shell** resist. During the photo-polymerization, steady state fluorescence spectra were obtained and the evolution of fluorescence intensity ratio between two wavelengths was evaluated.

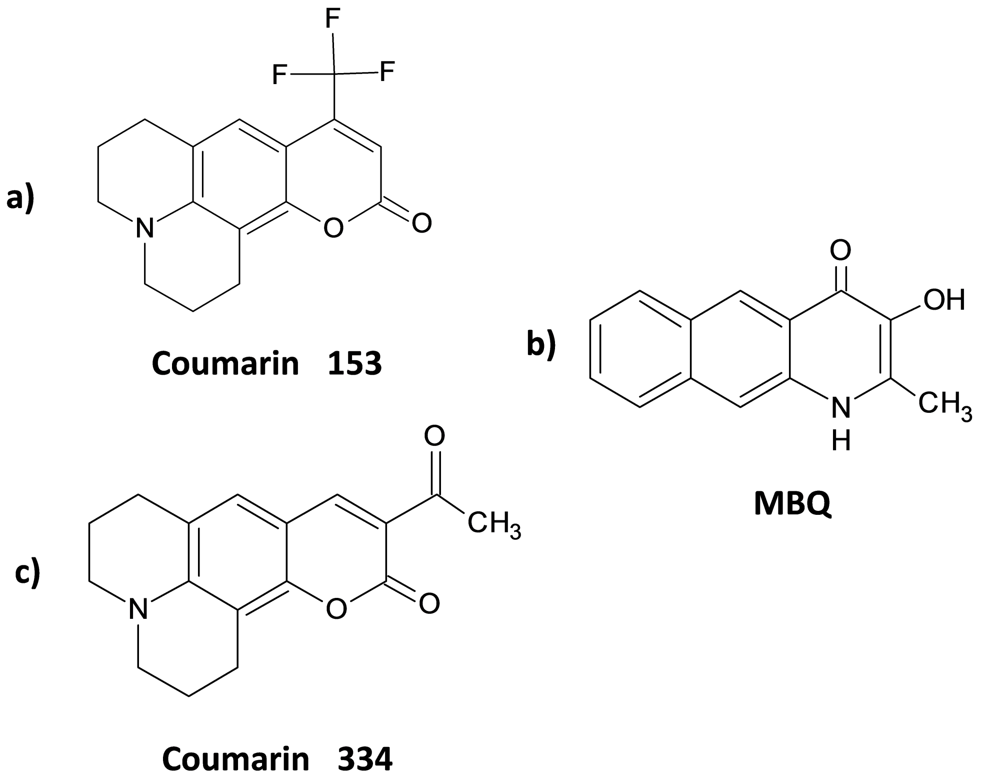

Figure 5.1: Molecular structures of dyes used for monitoring photo-polymerization : a) **Coumarin 153**; b) **Coumarin 334**; c) **MBQ**.

The progress of the photopolymerization was monitored with a special setup: Labis Nanoled (@365nm) was used as an excitation source (1 Watt). The stability of the led was checked in order to ensure the quality of excitation source (fig.5.2). Dye was dissolved in E-shell monomer mixture and a drop of the solution was deposited on a glass substrate. The polymerization was initiated upon irradiation with Nanoled@365nm. The process was monitored via fluorescence spectroscopy in real time by a Maya 2000 Pro Spectrometer (OceanOptics) and steady-state spectra were recorded, with time-step of 5 min. A low-pass filter at 420 nm was used .

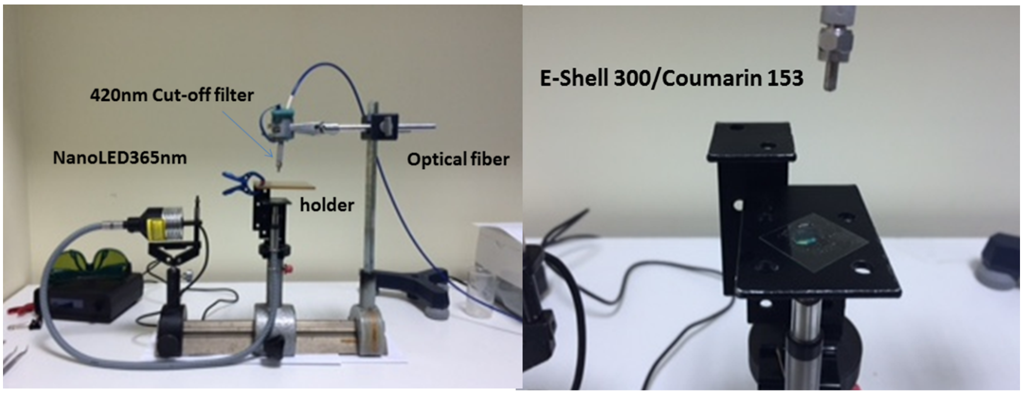

Figure 5.2: (left) Image of the experimental setup (right); image of substrate with **E-Shell** doped with **Coumarin 153** after the photo-polymerization.

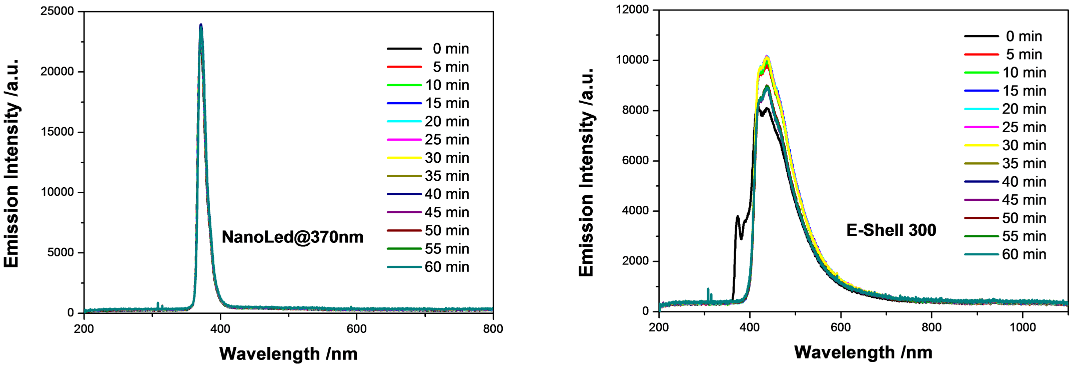

Figure 5.3: (left) Control of stability of excitation source (Nanoled@370nm);(right) evolution of emissions intensity of pristine **E-Shell 300** during the photo-polymerization.

### 5.1.1 E-Shell 300 doped with Coumarin 153

Coumarin derivative, are well known dyes for labeling applications. Coumarines are UV-vis-excitable and they exhibit a wide range of fluorescence emission (∼410 to 470 nm) [131]. The first dye we investigated as probe was **Coumarin 153**. The compound has maximum absorption at 422 nm and emission at 530 nm in ethanol. Its emission depends strongly on the micro environment and the solvent polarity.

Table 5.1: Coumarin 153

| **Polymerization Time (min)** | $I_{440nm}/I_{470nm}$ |
|---|---|
| 0 | 0,669 |
| 5 | 0,716 |
| 10 | 0,732 |
| 15 | 0,759 |
| 20 | 0,794 |
| 25 | 0,820 |
| 30 | 0,850 |
| 35 | 0,871 |
| 40 | 0,900 |

The evolution of fluorescence spectra of the **E-Shell 300** doped with **Coumarin 153** are reported in fig.5.4. When the photo-polymerization begins we observe two peaks: one located at 440 nm and another at 470 nm. During the polymerization the band at 440 nm progressively increases, the band at 470 nm decreases and slightly shifts to the blue. The fluorescence intensity ratio between 440 nm and 470 nm wavelengths has been evaluated versus time (table 5.1). Particularly a trend is recognized (fig.5.4): the ratio $I_{440nm}/I_{470nm}$ increases linearly with time.

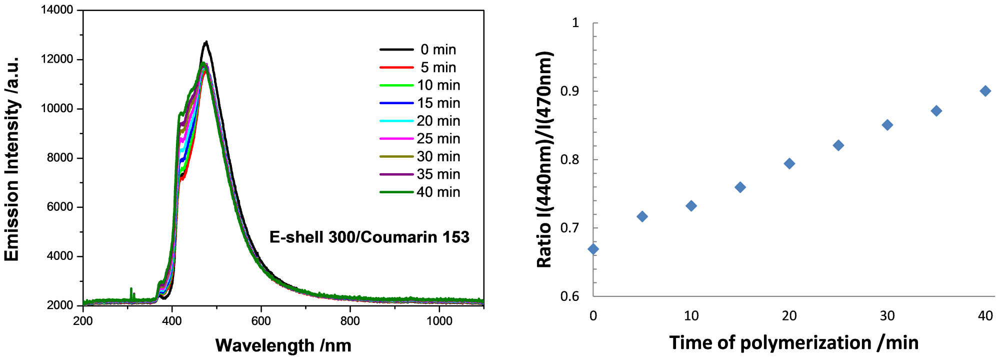

Figure 5.4: (left) Evolution of emission intensity of **E-Shell 300** doped with **Coumarin 153** during photo-polymerization process; (right) ratio evolution between the maximum intensities of the two emission bands ($I_{440nm}/I_{470nm}$).

### 5.1.2 E-Shell 300 doped with Coumarin 334

Another coumarin derivative used as probe was **Coumarine 334**. The dye has maximum absorption at 435 nm and emission at 475 nm in ethanol [132]. The evolution of fluorescence spectra of the **E-Shell 300** doped with **Coumarin 334** are reported in fig.5.5. In this case, at the beginning of process two emission bands are observed, located at 400 nm and 490 nm. During the polymerization the band at 400 nm increases, while the band at 490 nm decreases and marginally blue shifts. As the process is going on, a third band appears at 450 nm. The ratio $I_{400nm}/I_{490nm}$ increases linearly during the first 30 minutes and reaches a plateau after 40 minutes suggesting that the polymerization is accomplished (fig.5.5).

Table 5.2: Coumarin 334

| **Polymerization Time (min)** | $I_{400nm}/I_{490nm}$ |
|---|---|
| 0 | 0,173 |
| 5 | 0,249 |
| 10 | 0,341 |
| 15 | 0,427 |
| 20 | 0,533 |
| 25 | 0,631 |
| 30 | 0,699 |
| 35 | 0,773 |
| 40 | 0,830 |
| 45 | 0,857 |
| 50 | 0,889 |
| 55 | 0,907 |
| 60 | 0,919 |
| 65 | 0,937 |
| 70 | 0,954 |

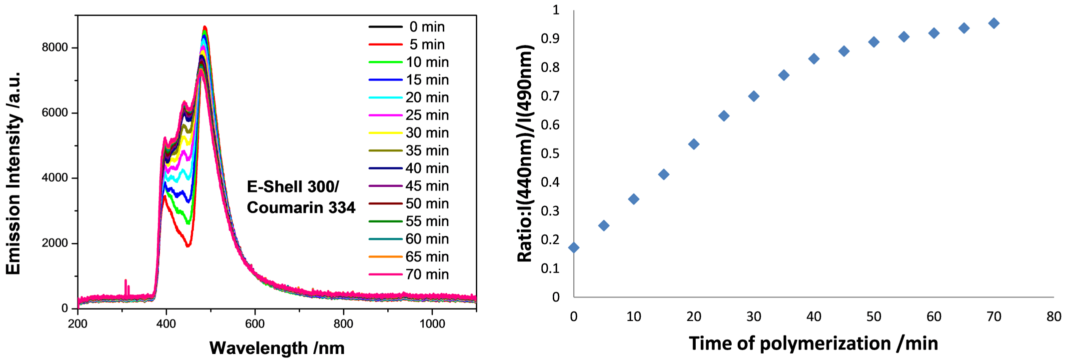

Figure 5.5: (left) Evolution of emission intensity of **E-Shell 300** doped with **Coumarin 334** during photo-polymerization process; (right) ratio evolution between the maximum intensities of the two emission bands ($I_{400nm}/I_{490nm}$).

### 5.1.3 E-Shell 300 doped with MBQ

The third dye used as probe is 3-hydroxy-2-methylbenzo[g]quilin-4(1H) (**MBQ**). The dye has an absorption band at 430 nm and an emission band with maximum at 470 nm in acetonitrile (fig.5.6).

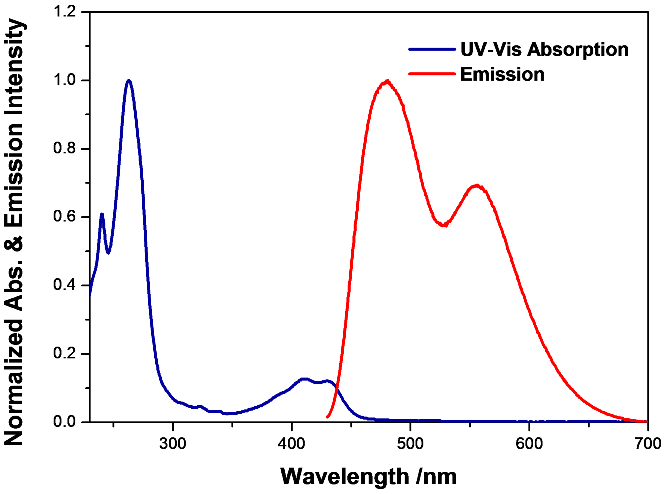

Figure 5.6: UV-Vis and emission spectra of **MBQ** in acetonitrile.

The recorded fluorescence spectra of the **E-Shell 300** doped with **MBQ** are presented in fig.5.7. Two sharp peaks are located at 417 nm and at 438 nm. Their intensity increases while the photo-polymerization is taking place. The evolution of ratio $I_{417nm}/I_{438nm}$ is almost constant indicating that it is not a good ratiometric probe.

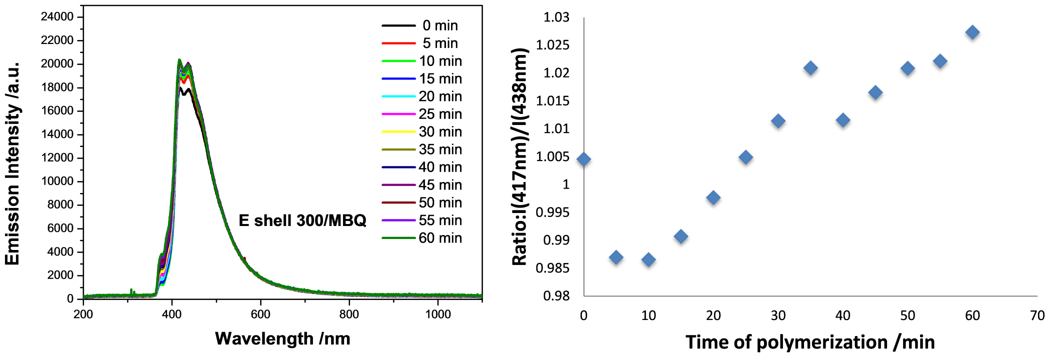

Figure 5.7: (left) Evolution of emission intensity of **E-Shell 300** doped with **MBQ** during photo-polymerization process; (right) ratio evolution between the maximum intensities of the two emission bands ($I_{417nm}/I_{438nm}$).

Table 5.3: MBQ

| **Polymerization Time (min)** | $I_{417nm}/I_{438nm}$ |
|---|---|
| 0 | 1,004 |
| 5 | 0,986 |
| 10 | 0,986 |
| 15 | 0,990 |
| 20 | 0,997 |
| 25 | 1,004 |
| 30 | 1,011 |
| 35 | 1,020 |
| 40 | 1,011 |
| 45 | 1,016 |
| 50 | 1,020 |
| 55 | 1,022 |
| 60 | 1,027 |

## 5.2 Synthesis of Aldehyde for Two-Photon Polymerization

In this section we describe the synthetic routine of an asymmetric aldehyde, as a precursor of a two-photon initiator. In our case, the target molecule was a compound composed by a triphenylamine group which has the role of electron donor and an aldehyde group is the acceptor connected by a $\pi$ bridge (bi-thienothiophene) (fig.5.8). The synthesis of the intermediates is described in detail, and has been performed according to the protocol reported by Ruikui Chen et al. [133]. The synthetic routine includes three chemical reactions: a monoformylation, a bromination and a Suzuki reaction. According to the retrosynthetic scheme reported in fig.5.8 Only the first and second steps were performed by my self during my secondment in University of Bordeaux.

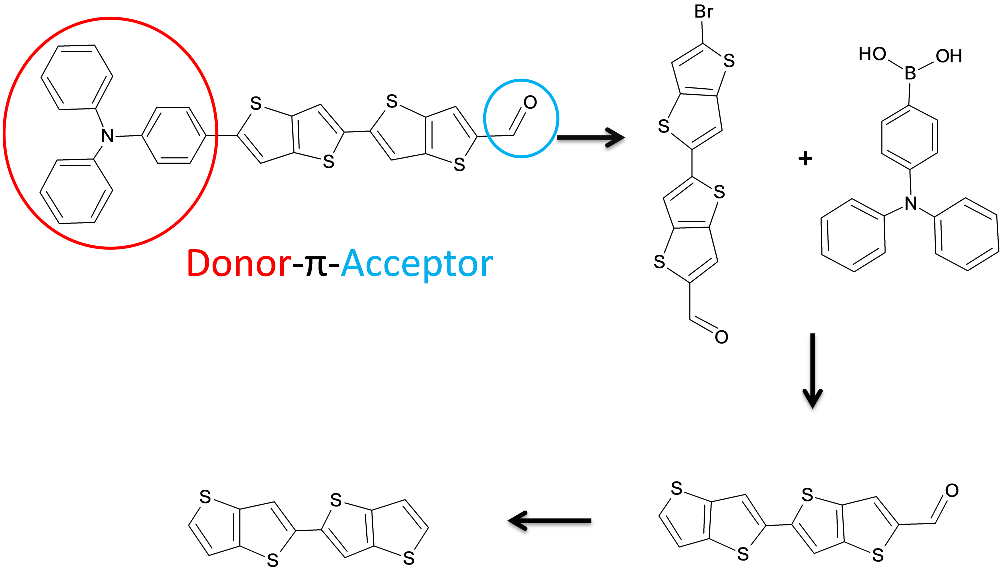

Figure 5.8: Retrosynthetic path of the aldehyde (D-$\pi$-A)

**Monoformylation reaction** Vilsmeier-Haack reaction (monoformylation) (fig.5.9) was performed to obtain the intermediate bi-thienothiophene aldehyde.

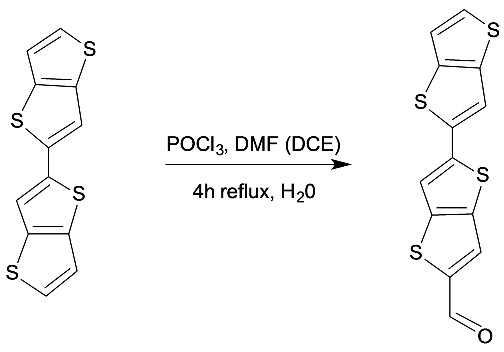

Figure 5.9: Vilsmeier-Haack (monoformylation) reaction

A solution of 100 mg of compound 2,2-bithieno[3,2-b]thiophene (commercially available) in anhydrous 1,2-Dichloroethane (2mL) is mixed with 36 $\mu$L of anhydrous DMF and 35 $\mu$L of $POCl_3$. The mixture was refluxed for 4 hours at $84^o$C under inert atmosphere. When the reaction was completed, iced water (10 mL) was introduced in the reaction mixture. The crude remained on ice for 2 hours under stirring. The qualitative control through naked eyes showed a variation of mixture's color from yellow to orange/brown, indicating that the reaction was performed.

The separation of the organic phase was obtained via decantation. During the "work up", water and DCM were used as solvents. The two phases were mixed and washed carefully three times. The organic phase was collected, dried with $Na_2SO_4$ and filtered. At the end the organic solvent was removed through rotary evaporation. TLC results indicate the presence of 3 fractions.

After the reaction, the fractions were separated with a normal phase column chromatography. During the purification a mixture of Petroleum Ether and Dichlomethane was used, in a ratio (PE/DCM): 2/1, 1/1, 1/2, only DCM. At the end 3 fractions were separated. The NMR spectra of fraction 2 revealed the presence of our expected product. NMR spectra of fraction 3 revealed the formation of bis-formylation product. The weight of the 2nd fraction was 27 mg corresponding to a yield of the reaction estimated of 25%. The amount of product was sufficient to shift to bromination.

Table 5.4: Fractions after monoformylation

| Fraction | Mass (mg) | Colour | Yield (%) |
|---|---|---|---|
| 1 | - | - | - |
| 2 | 27 | yellow | 25 |
| 3 | 12 | orange | - |

**Bromination** During the second step of the reaction, the product (aldehyde) was mixed with N-Bromosuccinimide (NBS) dissolved in dried DMF (fig.5.10). The reaction mixture was stirred at room temperature for 24 hours under inert conditions. After stirring the mixture was poured into 10 mL of water and drained into a Buchner funnel. TLC results indicate that the reaction did not occur. Since the bromination had not taken place, the starting material was collected and dissolved in THF with 5 equivalents of NBS, heated at $40^o$ C and stirred overnight. At the end of the reaction an orange precipitate solid was obtained. TLC results indicate that probably bromination did not complete. Purification was performed by normal phase column chromatography using a mixture of DCM and Petroleum Ether in ratio 1/1 and 1/2. NMR spectrum displays two peaks into CHO (aldehydes) range. It is possible that we achieved a mixture of regioisomeres.

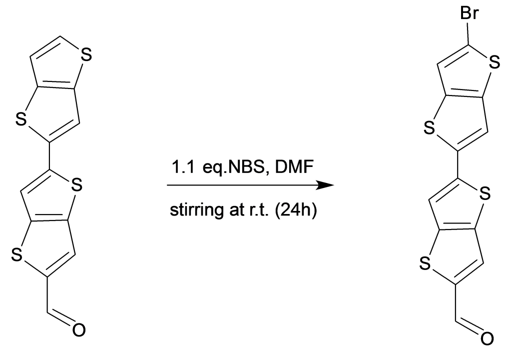

Figure 5.10: Bromination

As the 2nd step was not successful, we performed mononoformylation altering the equivalents of DMF and of $POCl_3$. After reaction the solvent (DCE) was not evaporated. For the "work up" Ethyl Acetate was used instead of DCM. The yield in second trial was of $8\%$. A third trial, keeping the initial stoichiometry but using THF as solvent instead of DCE, waked with a yield of $6\%$.

Table 5.5: Stoichiometry in monoformylation reaction

| Trial | $C_{12}H_6S_4$ | $POCl_3$ | $C_3H_7ON$ | $C_{13}H_6S_4O$ | Solvent | Yield (%) |
|---|---|---|---|---|---|---|
| 1 | 1 | 1.04 | 1.28 | 1 | DCE | 25 |
| 2 | 1 | 1 | 1 | 1 | DCE | 8 |
| 3 | 1 | 1.04 | 1.28 | 1 | THF | 6 |

**Distillation of DMF** Stirring with $CaH_2$ ($5\%$ w/v) overnight, filtered and then distilled at 20 mm Hg under Argon atmosphere. The distilled DMF was stored over 3Ä molecular sieves.

**Distillation of 1-2 Dichloroethane** For small amounts (up to 10 mL) of solvent, a Hickman Still micro-distillator was used. The distillator was evacuated and fluxed with

Argon.

## 5.3 Conclusions

In the first part of the chapter we suggests a method to monitor and control photo-polymerization using fluorescence probes. The photo-polymerization of **E-Shell 300** doped with **Coumarin 153**, with **Coumarin 334** and with **MBQ** was followed by fluorescence spectroscopy. The evolution of fluorescence intensity ratio between two wavelengths was evaluated in order to define the proper probe for the particular experiment. In **Coumarin 153** the ratio increases linear, and in **Coumarin 334** the ratio increases linear by up to 40 minutes and then reaches a plateau, suggesting that the polymerization is accomplished. **MBQ** was not suitable as ratiometric probe. It can be conclude that among three dyes **Coumarin 334** is a proper probe for the particular photo-reaction.

In the second part of the chapter we described the first steps of the organic synthesis of an non symmetrical aldehyde meant be used as initiator in two-photon polymerization.

# Chapter 6

# Outreach Activities and Communication of Science

## 6.1 Introduction

This PhD work was carried out in the frame of the European Commission ITN Nano2Fun project. Marie Curie Actions focus attention not only on research achievements, but also encourage researchers to approach the non-scientific community, in order to present main concepts and implications of their projects. For this purpose, outreach activities are organized where scientific results and technological achievements are communicated in accessible ways to the society.

Outreach activities are meant to engage a large audience and to bring knowledge and expertise on a particular topic to the general public. The activities can take several forms such as school presentations, workshops, public talks and lab visits. The objective of outreach is to explain the benefits of research to a larger public. Outreach implies an interaction between the scientists and the general public and is important for both sides, for scientists to have a feedback about their work and for society to approach science topics.

During the last three years several outreach activities have been organized having as main subject light and phenomena arising from its interaction with matter. Furthermore, a number of activities took place in the frame of the International Year of Light (IYL 2015). The International Year of Light and Light-based Technologies 2015 was a United Nations observance that aimed to communicate the achievements of light science and its applications. The Nano2Fun network, since its research interest was directly connected with this field, gave a great contribution to all of these events. Our research group visited an number of schools , was involved in Researchers Nights and contributed in exhibitions organized by the University of Parma.

Successful communication, especially with children requires a clear language and attractive scientific subjects with outstanding results, that can catch the attention of the audience and stimulate a passion for learning. The choice of tools and the way of presentation are important and deserves significant attention. The demonstrations should take into account several factors i.e. the age of the audience, the place, the available tools, the safety rules, and for sure if the message is arriving correctly from the sender to the receiver.

In this chapter, a series of basic optical experiments are presented, mainly addressed to school students. The main aim of the suggested activities is to show the basic properties of light interacting with matter, in a simple and stimulating way. Tools and materials are easily accessible and low cost.

## 6.2 "Playing with the Light"

Common optical phenomena are often due to the interaction of light with matter. Typical paradigms are: the rainbow, when light from the sun is reflected and refracted by water droplets; the color of the sky due to the scattering, when sun light interacts with atmosphere. These physical phenomena are daily observable and attract the curiosity of people, but often are not comprehensible . Other examples are the colours, the discrimination of transparent materials, glowing objects, refraction, diffraction or polarization of light: all these phonomena can easily be demonstrated in a classroom [134]. Here, we present a number of hands-on experience of these optical processes. The experiments are organized in a straightforward manner in order to be presented to non-scientific audience. [135] Particularly, the optical phenomena, we discuss, are:

- Refraction and dispersion of light
- Diffraction of light
- Light and Colours
- Polarization of light
- Fluorescence and phosphorescence

### 6.2.1 Refraction and Dispersion of Light

When light propagates through a medium it can be refracted. Refraction is the change in speed of an electromagnetic wave due to a change of the transmission medium. The change of the speed implies a change in the propagation direction. The refraction angle depends on wavelength of light, so that we can observe dispersion of polychromatic light. To demonstrate these phenomena we can use simple instruments such as lenses of different shape (for example, trapezoid, convex and concave), dispersive prism and sources of monochromatic or white light (fig 6.1) [136].

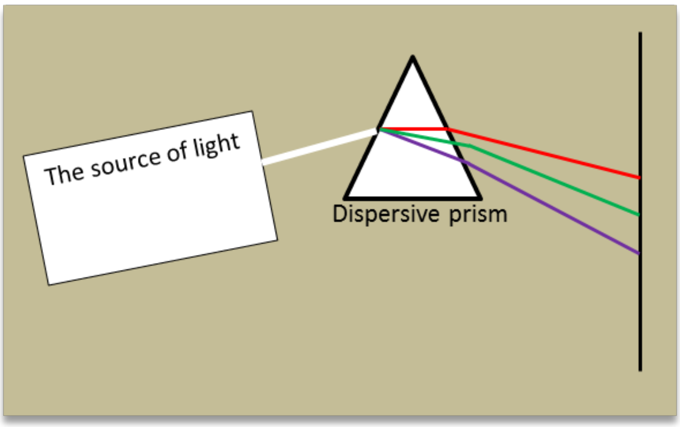

Figure 6.1: a) The refraction of the light in a dispersive element

An experiment that is based on optical phenomenon of refraction and helps to understand the term of refractive index, is the "invisible objects". For this experiment two beakers (glassware) in different size and sunflower oil are needed. We place the small beaker into the big one. Then, we fill the small beaker with sunflower oil and continue to fill it, till the glass is totally covered. The small glass then becomes invisible. The different refractive indexes between the mediums allows us to discern the transparent materials. For each material there is a specific refractive index. The sunflower and the fireproof glassware have the same refractive index. When the light propagates through the glass and the oil, it is not refracted. As a result, we cannot distinguish the beaker inside the oil, while we can clearly distinguish it in water in the air.

Another interesting experiment is related to total reflection. Particularly, we used a stream of water (a bottle of water with a hole) to capture and bend a laser beam. The laser beam is "trapped" inside the water because of total internal reflection. As the light tries to pass from the more-optically dense water to the less- optically dense air, it is totally reflected. In the narrow column of water, the light wave continues bouncing off the boundaries of the stream of water but cannot pass into the air.(fig.6.2)

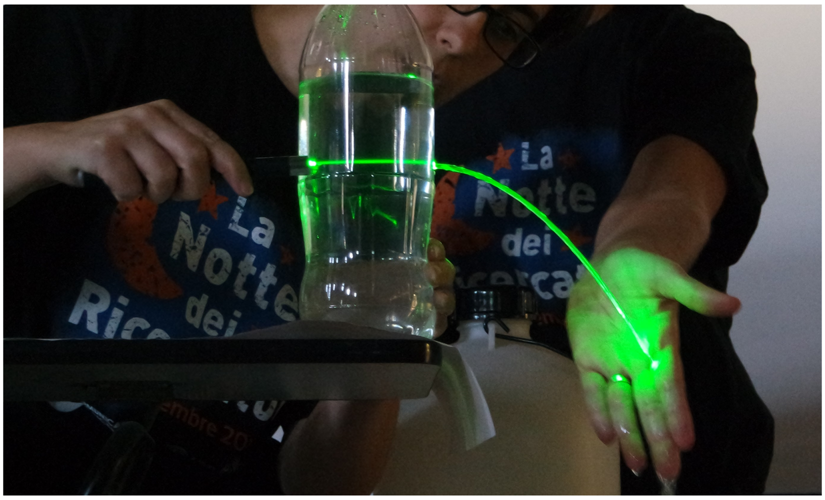

Figure 6.2: Light bends due to the phenomenon of total reflection.

### 6.2.2 Diffraction of Light

Diffraction of light occurs when a light wave passes through an obstacle or through an opening or slit having a size similar or even smaller than light's wavelength. For example, if we hit a hair with a monochromatic coherent light *from a laser pointer(, we observe diffraction of light, according to a diffraction pattermdepending on the thickness of the hair and the wavelength of light. Since diffraction from the same objectdepends on the wavelength of light, each component of white light is diffracted differently. In fact, when white light hits a diffraction grating (an optical component with a periodic structure), the grating splits white light into a rainbow thanks to to refraction and interference [137]. Because of this, gratings are commonly used in monochromators and spectrometers. The sparkling effects from the closely spaced narrow tracks on optical storage disks such as CDs or DVDs are an example and can be used to fabricate a "home made" spectroscope.

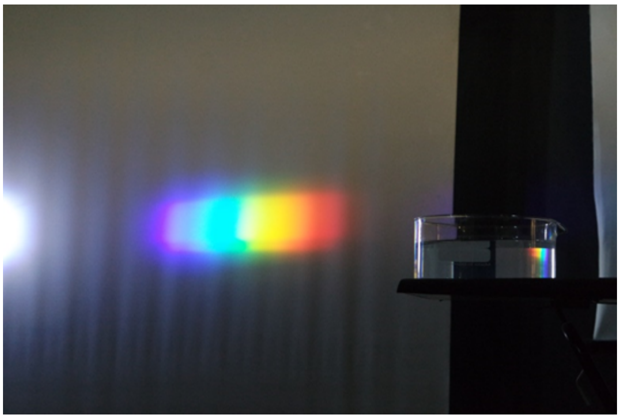

Figure 6.3: The white light splits into different colours (different wavelengths) by a diffraction grating

.

It is possible to fabricate a handmade spectroscope with simple materials like a paper, a cd and a tape. The spectroscope splits light into the wavelengths that make it up and helps to realize that different sources of light do not shine in the same way. Figure 6.4 shows a discrete and a continuous emission spectrum of two different light sources.

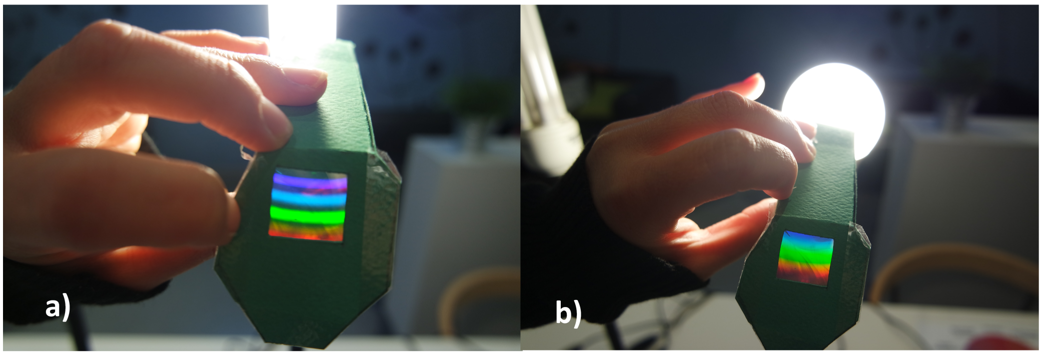

Figure 6.4: Emission spectra of two different commercial lamps obtained via a homemade spectrometer a) Discrete emission spectrum b) Continuous emission spectrum.

### 6.2.3 Light and Colours

Here, we demonstrate that white light is constituted by different colors, and that a coloured substance absorbs the complementary color with respect to the observed one. To perform this experiment a visible source, a dispersion element and coloured filters are needed. Illuminating the dispersion element with the light source, the white light will separate in the rainbow colors. Then placing a coloured filter between the light source and the dispersion element, the dispersed light will not contain any more the complementary color of the filter, e.g. if the filter is yellow, the dispersed will not show the violet-blue component (fig.6.5). This means that the color of a substance (in this case the filter) is determined by the portion of the light spectrum that it absorbs.

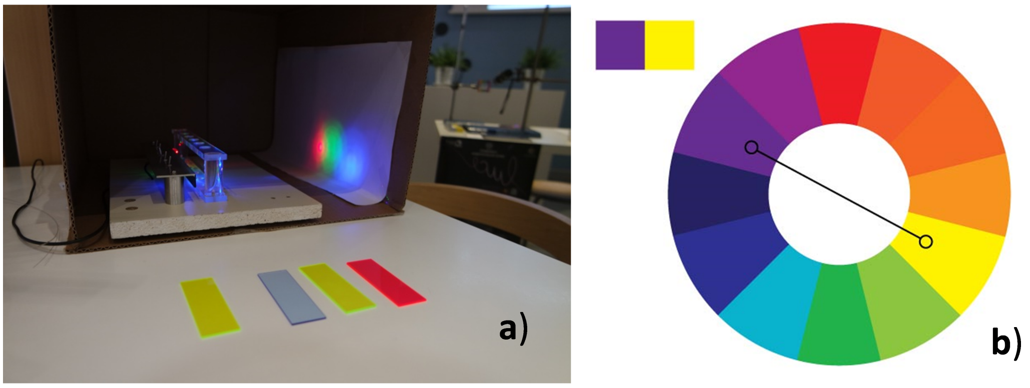

Figure 6.5: a) Dispersed light and coloured filters b) Complementary colors are opposite each other on the color wheel i.e. the yellow component of light is absorbed by the violet filter.

### 6.2.4 Polarization of Light

Another interesting property of light is polarization. To observe this property we can carry out a simple experiment with a source of non polarized light and two linear polarizers. When polarization planes of the two polarizers are parallel, we observe transmission of light through this system. When polarization planes are perpendicular we do not observe any transmitted light. Alternatively, it is possible to replace the light source with a laser light and see if it is polarized [138], or check if light emitted from LCD or LED screen is polarized or not.

### 6.2.5 Fluorescence and Phosphorescence

The experiment shows that some materials emit light after illumination with UV or visible light (excitation). Spontaneous emission can be distinguished into fluorescence and phosphorescence, according to the lifetime of the process. Phosphorescence is a very long process: it continues for seconds, minutes or hours after excitation. Fluorescence is very short: it turns off in some (hundreds of) nanoseconds so that it cannot be seen after excitation. For this experiment, fluorescent and phosphorescent material (e.g.tonic water, detergent whitener, toys that glow in the dark) and a UV lamp are needed. To distinguish fluorescence from phosphorescence, we illuminate the materials with the UV-lamp (fig.6.6): all the luminescence materials will emit light. Turn off the light: some of them will continue emitting light (phosphorescent materials), while emitted light of the others is turned off in the absence of excitation (fluorescent materials)

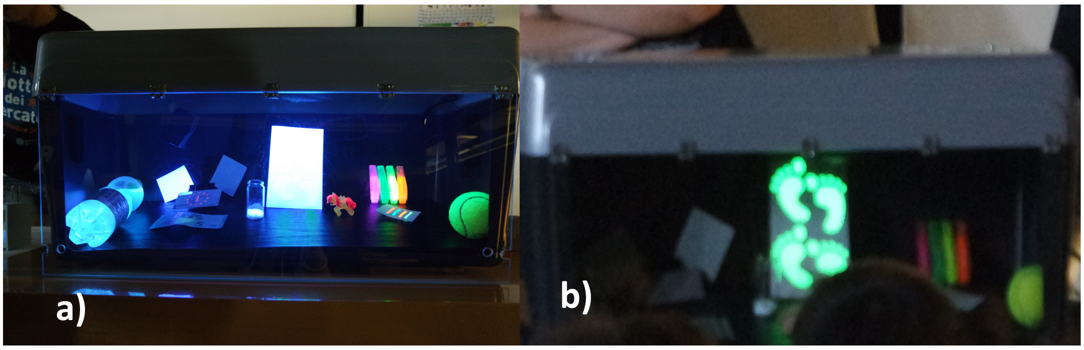

Figure 6.6: a) Emissive materials under excitation with UV light b) Phosphorescent material emits for long time after excitation is switched off.

# Appendix 1:Two-Photon Excited Fluorescence

The Two-Photon Absorption Cross Section data reported in chapter 3, were measured via the Two-Photon Excited Fluorescence technique. In this technique, the fluorescence signal of a fluorophore is recorded upon excitation through two-photon absorption process. The cross section of TPA $\sigma_2(\lambda)$ is derived by comparison to a reference compound and by the fluorescence quantum yield ($\Phi$) of the sample. Considering that $\Phi$ is equal for one and two photon excitation, the fluorescence signal $F$ induced by two-photon absorption is:

$$F = \frac{CP^2 f \sigma_2(\lambda)\Phi}{n^2}$$

where $C$ is the concentration of absorbing fluorophore, $P$ is the power of the incident beam, $f$ is a correction factor depending on the instrument and $n$ is the refractive index of the medium.

The Two-Photon Absorption Cross Section, for each wavelength, is estimated from the formula:

$$\sigma_2(\lambda) = \frac{[\sigma_2(\lambda)]_R f_R F}{\Phi f P^2}(\frac{F_R}{P_R^2})^{-1}$$

where $[\sigma_2(\lambda)]_R$ is the Two-Photon Absorption Cross Section of a reference compound (R), at specific wavelength $\lambda$. The output signals are given by the ratio $\frac{F}{P^2}$ of sample and reference. The power *P* is varied 3 times for every wavelength: the obtained ratio values must be constant and the fluorescence signal must have quadratic dependence on the incident power.

The excitation source was a Ti:sapphire laser, generating 150 fs pulses at 76 MHz repetition rate. To extend the spectral region up to 1200 nm, an optical parametric oscilator (OPO) was used. Two references compounds were used: fluorescein in 0.01 M NaOH Water, from 700 to 980 nm, and Nilered in EtOH from 980 to 1200 nm. The fluorescence signal was collected in epifluorescence geometry.

# Appendix 2: Integrating Sphere

The absolute luminescence quantum yield can be determined by an integrating sphere setup. The method allows the direct measurement of the efficiency of the conversion of absorbed light into emitted light of highly scattering materials such as powders or films. The LQY of thin films reported in chapter 4 were measured by an integrating sphere mounted in a fluorometer.

The standard method, includes three measurements. The first couple of measurements allows the estimation of the absorbance of the sample:

$$A = \frac{L_b - L_c}{L_b}$$

where $L_b$ is the integrated excitation profile when the sample is diffusely illuminated by the integrating sphere's surface and $L_c$ is the integrated excitation profile when the sample is directly excited by the incident beam.

The luminescence quantum yield ($\Phi$),by definition, is the total number of emitted photons divided by the total number of absorbed photons:

$$\Phi = \frac{E_c - (1 - A)E_b}{L_a A} = \frac{E_c - E_a}{L_a - L_c}$$

where $E_c$ is the integrated luminescence of the film caused by direct excitation, and $E_b$ is the integrated luminescence of the film caused by indirect illumination from the sphere. The term $L_a$ is the integrated excitation profile from an empty integrating sphere and $E_a$ is the integrated luminescence from an empty integrating sphere. Actually $L_a$ in more reliably obtained using an appropriate reference (in the case of our films, the reference was a pure PMMA film obtained in the same conditions on the samples).

# Appendix 3:

# Kohlrausch-Williams-Watts stretched exponential function (KWW)

The stretched exponential function has application in modelling various types of experimental relaxation data. It is also known as the Kohlrausch-Williams-Watts (KWW) function because it was firstly introduced by Rudolf Kohlrausch to describe the discharge of a capacitor and subsequently used by G. Williams and D.C. Watts to describe dielectric spectra of polymers.

The KWW function have proved to be more appropriate than a multi-exponential function with an arbitrary number of discrete lifetimes in modelling the associated relaxation and decay processes in complex systems or heterogeneous samples such as suspensions, solid samples or bio-systems, where the entire spectrum of relaxation times is non-linear and not purely exponential, while shows continuous lifetime distributions

In relaxation processes, including time-dependent luminescence spectroscopy, a perturbation is applied to the system up to an instant set as the origin of time (t = 0). At this moment, the perturbation is suddenly removed, and the system relaxes towards the equilibrium ($t \to \infty$). The time-dependent relaxation function $I(t)$, defined from a property *P* of the system as:

$$I(t) = \frac{P(t) - P(\infty)}{P(0) - P(\infty)}$$

can also be written as:

$$I(t) = exp(-\int_0^t w(u)du)$$

where w(t) is a time-dependent rate coefficient,

$$w(t) = -\frac{dlnI}{dt}$$

In the simplest case, w(t) is time-independent and the decay is exponential. For dw/dt > 0, the decay is super-exponential, and if dw/dt < 0, the decay is sub-exponential. However, the presence of progressively depleted random sinks that capture excitation can modify a spontaneous decay process, such that the decay rate itself is dependent on time, stretching the decay.

The stretched exponential decay function is given by:

$$I(t) = I_o exp[-(t/\tau_o)^{\beta}]$$

where I(t) is the fluorescence intensity at time t, $I_0$ is the fluorescence intensity at time 0, $\tau_0$ is the characteristic time scale of the decay and $\beta$ is the stretching factor ($0 < \beta \leq 1$). The function is close to an exponential when the stretching exponent $\beta$ is near unity.

The stretched exponential offers an additional parameter: the heterogeneity constant *h* defined as $h = 1/\beta$, ($h \leq 1$). For $h = 1$ corresponds to homogeneous systems. Also, the mean relaxation time can be directly obtained from:

$$< \tau >= \tau_o \Gamma(1 + 1/\beta)$$

where $\Gamma$ is the Gamma function:

$$\Gamma(z) = \int_0^\infty x^{z-1} e^x dx$$

# Publications

1. Elisa Campioli, Domna M. Nikolaidou, Vincent Hugues, Marco Campanini, Lucia Nasi, Mireille Blanchard-Desce and Francesca Terenziani.

   *Amplified two-photon brightness in organic multicomponent nanoparticles*

   **J. Mater. Chem. C**, 2015, 7483-7491.

2. Davide Blasi, Domna M. Nikolaidou, Francesca Terenziani, Imma Ratera and Jaume Veciana.

   *Excimers from Stable and Persistent Supramolecular Radical-Pairs in Red/NIR-Emitting Organic Nanoparticles and Polymeric Films*

   **Phys.Chem.Chem.Phys.**, 2017, 9313-9319.

3. Article in preparation

   *Photophysical properties and aggregation effects on Polychlorotriphenyl methyl radical.*

# Bibliography

[1] J. H. Strickler and W. W. Webb, *Optics letters*, vol. 16, no. 22, pp. 1780–1782, 1991. 1

[2] B. H. Cumpston, S. P. Ananthavel, S. Barlow, D. L. Dyer, J. E. Ehrlich, L. L. Erskine, A. A. Heikal, S. M. Kuebler, I.-Y. S. Lee, D. McCord-Maughon *et al.*, *Nature*, vol. 398, no. 6722, pp. 51–54, 1999. 1

[3] X. Yin, N. Fang, X. Zhang, I. B. Martini, and B. J. Schwartz, *Applied Physics Letters*, vol. 81, no. 19, pp. 3663–3665, 2002. 1

[4] S. Jeon, V. Malyarchuk, J. A. Rogers, and G. P. Wiederrecht, *Optics Express*, vol. 14, no. 6, pp. 2300–2308, 2006. 1

[5] C. Xu, W. Zipfel, J. B. Shear, R. M. Williams, and W. W. Webb, *Proceedings of the National Academy of Sciences*, vol. 93, no. 20, pp. 10 763–10 768, 1996. 1, 7

[6] P. T. So, C. Y. Dong, B. R. Masters, and K. M. Berland, *Annual review of biomedical engineering*, vol. 2, no. 1, pp. 399–429, 2000. 1

[7] W. Denk, J. H. Strickler, W. W. Webb *et al.*, *Science*, vol. 248, no. 4951, pp. 73–76, 1990. 1, 7

[8] A. Diaspro, *Confocal and Two-Photon Microscopy: Foundations, Applications and Advances, by Alberto Diaspro (Editor), pp. 576. ISBN 0-471-40920-0. Wiley-VCH, November 2001.*, p. 576, 2001. 1, 7

[9] C. Spangler, *Journal of Materials Chemistry*, vol. 9, no. 9, pp. 2013–2020, 1999. 1

[10] J. Chen, H. Peng, C. C. Law, Y. Dong, J. W. Lam, I. D. Williams, and B. Z. Tang, *Macromolecules*, vol. 36, no. 12, pp. 4319–4327, 2003. 1

[11] M. Drobizhev, A. Karotki, A. Rebane, and C. W. Spangler, *Optics letters*, vol. 26, no. 14, pp. 1081–1083, 2001. 1, 6

[12] S. Kim, Q. Zheng, G. S. He, D. J. Bharali, H. E. Pudavar, A. Baev, and P. N. Prasad, *Advanced Functional Materials*, vol. 16, no. 18, pp. 2317–2323, 2006. 1

[13] M. Gary-Bobo, Y. Mir, C. Rouxel, D. Brevet, I. Basile, M. Maynadier, O. Vaillant, O. Mongin, M. Blanchard-Desce, A. Morere *et al.*, *Angewandte Chemie*, vol. 123, no. 48, pp. 11 627–11 631, 2011. 1

[14] J. L. Hua, B. Li, F. S. Meng, F. Ding, S. X. Qian, and H. Tian, *Polymer*, vol. 45, no. 21, pp. 7143–7149, 2004. 1

[15] F. Terenziani, C. Katan, E. Badaeva, S. Tretiak, and M. Blanchard-Desce, *Advanced Materials*, vol. 20, no. 24, pp. 4641–4678, 2008. 3, 5

[16] M. Albota, D. Beljonne, J.-L. Bredas, J. E. Ehrlich, J.-Y. Fu, A. A. Heikal, S. E. Hess, T. Kogej, M. D. Levin, S. R. Marder *et al.*, *Science*, vol. 281, no. 5383, pp. 1653–1656, 1998. 3

[17] M. Rumi and J. W. Perry, *Adv. Opt. Photon.*, no. 4, pp. 451–518, Dec 2010. 3

[18] D. Petrov, A. Gomes, and C. B. de Araujo, *Applied physics letters*, vol. 65, no. 9, pp. 1067–1069, 1994. 4

[19] M. Sheik-Bahae, A. A. Said, T.-H. Wei, D. J. Hagan, and E. W. Van Stryland, *IEEE journal of quantum electronics*, vol. 26, no. 4, pp. 760–769, 1990. 4

[20] C. Xu and W. W. Webb, *JOSA B*, vol. 13, no. 3, pp. 481–491, 1996. 5

[21] F. Terenziani, A. Painelli, C. Katan, M. Charlot, and M. Blanchard-Desce, *Journal of the American Chemical Society*, vol. 128, no. 49, pp. 15 742–15 755, 2006. 6

[22] F. Terenziani, O. V. Przhonska, S. Webster, L. A. Padilha, Y. L. Slominsky, I. G. Davydenko, A. O. Gerasov, Y. P. Kovtun, M. P. Shandura, A. D. Kachkovski *et al.*, *The Journal of Physical Chemistry Letters*, vol. 1, no. 12, pp. 1800–1804, 2010. 6

[23] M. Oheim, E. Beaurepaire, E. Chaigneau, J. Mertz, and S. Charpak, *Journal of neuroscience methods*, vol. 111, no. 1, pp. 29–37, 2001. 7

[24] K. Gaus, E. Gratton, E. P. Kable, A. S. Jones, I. Gelissen, L. Kritharides, and W. Jessup, *Proceedings of the National Academy of Sciences*, vol. 100, no. 26, pp. 15 554–15 559, 2003. 7

[25] M. Drobizhev, N. S. Makarov, S. E. Tillo, T. E. Hughes, and A. Rebane, *Nature methods*, vol. 8, no. 5, pp. 393–399, 2011. 7

[26] E. Brown, T. McKee, A. Pluen, B. Seed, Y. Boucher, R. K. Jain *et al.*, *Nature medicine*, vol. 9, no. 6, pp. 796–800, 2003. 7

[27] P. T. So, C. Y. Dong, B. R. Masters, and K. M. Berland, *Annual review of biomedical engineering*, vol. 2, no. 1, pp. 399–429, 2000. 8, 9

[28] B. R. Masters, P. So, and E. Gratton, *Biophysical journal*, vol. 72, no. 6, pp. 2405–2412, 1997. 10

[29] Y.-H. Pao and P. Rentzepis, *Applied Physics Letters*, vol. 6, no. 5, pp. 93–95, 1965. 10

[30] F. Claeyssens, E. A. Hasan, A. Gaidukeviciute, D. S. Achilleos, A. Ranella, C. Reinhardt, A. Ovsianikov, X. Shizhou, C. Fotakis, M. Vamvakaki *et al.*, *Langmuir*, vol. 25, no. 5, pp. 3219–3223, 2009. 10, 11

[31] M. Farsari and B. N. Chichkov, *Nature photonics*, vol. 3, no. 8, p. 450, 2009. 10, 11

[32] K. Ueno, S. Juodkazis, T. Shibuya, Y. Yokota, V. Mizeikis, K. Sasaki, and H. Misawa, *Journal of the American Chemical Society*, vol. 130, no. 22, pp. 6928–6929, 2008. 10, 11

[33] H.-B. Sun and S. Kawata, 2004, pp. 169–273. 10

[34] M. Farsari, M. Vamvakaki, and B. N. Chichkov, *Journal of Optics*, vol. 12, no. 12, p. 124001, 2010. 11, 12

[35] V. Prokhorenko, D. Steensgaard, and A. Holzwarth, *Biophysical journal*, vol. 85, no. 5, pp. 3173–3186, 2003. 12

[36] A. Davydov, *Theory of molecular excitons*. Springer, 2013. 13

[37] G. D'Avino, F. Terenziani, and A. Painelli, *The Journal of Physical Chemistry B*, vol. 110, no. 51, pp. 25 590–25 592, 2006. 13

[38] K. D. Belfield, M. V. Bondar, F. E. Hernandez, O. V. Przhonska, and S. Yao, *Chemical physics*, vol. 320, no. 2, pp. 118–124, 2006. 13

[39] J. Shin, N. S. Kang, K. H. Kim, T. W. Lee, J.-I. Jin, M. Kim, K. Lee, B. K. Ju, J.-M. Hong, and D. H. Choi, *Chemical Communications*, vol. 48, no. 68, pp. 8490–8492, 2012. 13

[40] I. Vaya, T. Gustavsson, T. Douki, Y. Berlin, and D. Markovitsi, *Journal of the American Chemical Society*, vol. 134, no. 28, pp. 11 366–11 368, 2012. 14

[41] J. G. Morin and J. Hastings, *Journal of cellular physiology*, vol. 77, no. 3, pp. 313–318, 1971. 14

[42] A. R. Clapp, I. L. Medintz, J. M. Mauro, B. R. Fisher, M. G. Bawendi, and H. Mattoussi, *Journal of the American Chemical Society*, vol. 126, no. 1, pp. 301–310, 2004. 14

[43] H. Wallrabe and A. Periasamy, *Current opinion in biotechnology*, vol. 16, no. 1, pp. 19–27, 2005. 14

[44] E. A. Jares-Erijman and T. M. Jovin, *Nature biotechnology*, vol. 21, no. 11, pp. 1387–1395, 2003. 14

[45] P. Wu and L. Brand, *Analytical biochemistry*, vol. 218, no. 1, pp. 1–13, 1994. 14

[46] A. K. Kenworthy, *Methods*, vol. 24, no. 3, pp. 289–296, 2001. 14

[47] R. F. de Almeida, L. M. Loura, A. Fedorov, and M. Prieto, *Journal of molecular biology*, vol. 346, no. 4, pp. 1109–1120, 2005. 14

[48] J. R. Lakowicz, Ed., *Principles of Fluorescence Spectroscopy*, 2006, pp. 277–330. 15, 21, 86, 94

[49] M. Kasha, *Radiation research*, vol. 20, no. 1, pp. 55–70, 1963. 15

[50] T. Forster, “Excimers,” *Angewandte Chemie International Edition in English*, vol. 8, no. 5, pp. 333–343, 1969. 15, 16

[51] P. Wu and L. Brand, *Biochemistry*, vol. 31, no. 34, pp. 7939–7947, 1992. 17

[52] N. Anton, J.-P. Benoit, and P. Saulnier, *Journal of Controlled Release*, vol. 128, no. 3, pp. 185 – 199, 2008. 20

[53] S. Hornig and T. Heinze, *Biomacromolecules*, vol. 9, no. 5, pp. 1487–1492, 2008. 20

[54] X. Li, N. Anton, C. Arpagaus, F. Belleteix, and T. F. Vandamme, *Journal of Controlled Release*, vol. 147, no. 2, pp. 304 – 310, 2010. 20

[55] I. K. Wright, A. Higginbotham, S. M. Baker, and T. D. Donnelly, *ACS Applied Materials Interfaces*, vol. 2, no. 8, pp. 2360–2364, 2010. 20

[56] C. Weber, C. Coester, J. Kreuter, and K. Langer, *International Journal of Pharmaceutics*, vol. 194, no. 1, pp. 91 – 102, 2000. 20

[57] H. Wang, E. Zhao, J. W. Lam, and B. Z. Tang, *Materials Today*, vol. 18, no. 7, pp. 365 – 377, 015. 21

[58] Z. Ning, Z. Chen, Q. Zhang, Y. Yan, S. Qian, Y. Cao, and H. Tian, *Advanced Functional Materials*, vol. 17, no. 18. 21

[59] Y. Hong, J. W. Y. Lam, and B. Z. Tang, *Chem. Soc. Rev.*, vol. 40, pp. 5361–5388, 2011. 21

[60] H. Kasai, H. S. Nalwa, H. Oikawa, S. Okada, H. Matsuda, N. Minami, A. Kakuta, K. Ono, A. Mukoh, and H. Nakanishi, *Japanese Journal of Applied Physics*, vol. 31, no. 8A, p. L1132, 1992. 23

[61] V. Parthasarathy, S. Fery-Forgues, E. Campioli, G. Recher, F. Terenziani, and M. Blanchard-Desce, *Small*, vol. 7, no. 22, 2011. 24

[62] Z. Tan, A. Masuhara, H. Kasai, H. Nakanishi, and H. Oikawa, *Japanese Journal of Applied Physics*, vol. 47, no. 2S, p. 1426, 2008. 24

[63] R. C. Evans, *Chem. Soc. Rev.*, vol. 1, pp. 4190–4200, 2013. 24

[64] P. C. Rodrigues, B. D. Fontes, B. B. M. Torres, W. S. Sousa, G. C. Faria, D. T. Balogh, R. M. Faria, and L. Akcelrud, *Journal of Applied Polymer Science*, vol. 132, no. 38, 2015. 24

[65] K. D. Belfield, C. C. Corredor, A. R. Morales, M. A. Dessources, and F. E. Hernandez, *Journal of Fluorescence*, vol. 16, no. 1, pp. 105–110, 2006. 24

[66] K. D. Belfield, D. J. Hagan, E. W. Van Stryland, K. J. Schafer, and R. A. Negres, *Organic Letters*, vol. 1, no. 10, pp. 1575–1578. 24

[67] S. Yao, H.-Y. Ahn, X. Wang, J. Fu, E. W. Van Stryland, D. J. Hagan, and K. D. Belfield, *The Journal of Organic Chemistry*, vol. 75, no. 12, pp. 3965–3974, 2010. 24

[68] S. A. Kurhuzenkau, A. W. Woodward, S. Yao, K. D. Belfield, Y. O. Shaydyuk, C. Sissa, M. V. Bondar, and A. Painelli, *Phys. Chem. Chem. Phys.*, vol. 18, pp. 12 839–12 846, 2016. 24, 26

[69] E. Ishow, A. Brosseau, G. Clavier, K. Nakatani, P. Tauc, C. Fiorini-Debuisschert, S. Neveu, O. Sandre, and A. Leaustic, *Chemistry of Materials*, vol. 20, no. 21, pp. 6597–6599, 2008. 27

[70] H.-B. Fu and J.-N. Yao, *Journal of the American Chemical Society*, vol. 123, no. 7, pp. 1434–1439, 2001. 30

[71] M. D. Smith, B. Mostofian, L. Petridis, X. Cheng, and J. C. Smith, *The Journal of Physical Chemistry B*, vol. 120, no. 4, pp. 740–747, 2016. 33

[72] H. Tokuhisa, M. Era, T. Tsutsui, and S. Saito, *Applied Physics Letters*, vol. 66, no. 25, pp. 3433–3435, 1995. 36

[73] J. Zhang, M. Matsuoka, H. Yamashita, and M. Anpo, *Langmuir*, vol. 15, no. 1, pp. 77–82, 1999. 36

[74] X. Zhang, X. Xie, H. Wang, J. Zhang, B. Pan, and Y. Xie, *Journal of the American Chemical Society*, vol. 135, no. 1, pp. 18–21, 2013. 40

[75] J. M. Costa-Fernandez, R. Pereiro, and A. Sanz-Medel, *TrAC Trends in Analytical Chemistry*, vol. 25, no. 3, pp. 207 – 218, 2006. 40

[76] M. Hauser, M. Wojcik, D. Kim, M. Mahmoudi, W. Li, and K. Xu, “Correlative super-resolution microscopy: New dimensions and new opportunities,” *Chemical Reviews*, 2017. 40

[77] T. Asahi, T. Sugiyama, and H. Masuhara, *Accounts of Chemical Research*, vol. 41, no. 12, pp. 1790–1798, 2008. 40

[78] X. Michalet, F. F. Pinaud, L. A. Bentolila, J. M. Tsay, S. Doose, J. J. Li, G. Sundaresan, A. M. Wu, S. S. Gambhir, and S. Weiss, *Science*, vol. 307, no. 5709, pp. 538–544, 2005. 40

[79] X. Gao, L. Yang, J. A. Petros, F. F. Marshall, J. W. Simons, and S. Nie, *Current opinion in biotechnology*, vol. 16, no. 1, pp. 63–72, 2005. 40

[80] W. C. Chan, D. J. Maxwell, X. Gao, R. E. Bailey, M. Han, and S. Nie, *Current Opinion in Biotechnology*, vol. 13, no. 1, pp. 40 – 46, 2002. 40

[81] C. Rouxel, M. Charlot, O. Mongin, T. R. Krishna, A.-M. Caminade, J.-P. Majoral, and M. Blanchard-Desce, *Chemistry–A European Journal*, vol. 18, no. 51, pp. 16 450–16 462, 2012. 40

[82] J. Shen, Y. Zhu, X. Yang, and C. Li, *Chem. Commun.*, vol. 48, pp. 3686–3699, 2012. 40

[83] T. Ribeiro, S. Raja, A. S. Rodrigues, F. Fernandes, J. P. S. Farinha, and C. Baleizao, *RSC Adv.*, vol. 3, pp. 9171–9174, 2013. 40

[84] I.-Y. Kim, E. Joachim, H. Choi, and K. Kim, *Nanomedicine: Nanotechnology, Biology and Medicine*, vol. 11, no. 6, pp. 1407–1416, 2015. 41

[85] J. Duan, Y. Yu, Y. Li, Y. Yu, Y. Li, X. Zhou, P. Huang, and Z. Sun, *PLOS ONE*, vol. 8, 04 2013. 41

[86] E. Genin, Z. Gao, J. A. Varela, J. Daniel, T. Bsaibess, I. Gosse, L. Groc, L. Cognet, and M. Blanchard-Desce, *Advanced Materials*, vol. 26, no. 14, pp. 2258–2261, 2014. 41

[87] D. R. Larson, W. R. Zipfel, R. M. Williams, S. W. Clark, M. P. Bruchez, F. W. Wise, and W. W. Webb, *Science*, vol. 300, no. 5624, pp. 1434–1436, 2003. 41, 66

[88] A. Jana, K. T. Nguyen, X. Li, P. Zhu, N. S. Tan, H. Agren, and Y. Zhao, *ACS nano*, vol. 8, no. 6, pp. 5939–5952, 2014. 41

[89] T. Funada, T. Hirose, N. Tamai, and H. Yao, *Physical Chemistry Chemical Physics*, vol. 17, no. 16, pp. 11 006–11 013, 2015. 41

[90] Y. Jiang, Y. Wang, J. Hua, J. Tang, B. Li, S. Qian, and H. Tian, *Chemical Communications*, vol. 46, no. 26, pp. 4689–4691, 2010. 42

[91] R. J. Hunter. Academic press, 2013, vol. 2. 47

[92] X. Shi, Z. Xu, Q. Liao, Y. Wu, Z. Gu, R. Zheng, and H. Fu, *Dyes and Pigments*, vol. 115, pp. 211–217, 2015. 65

[93] S. B. Noh, R. H. Kim, W. J. Kim, S. Kim, K.-S. Lee, N. S. Cho, H.-K. Shim, H. E. Pudavar, and P. N. Prasad, *Journal of Materials Chemistry*, vol. 20, no. 35, pp. 7422–7429, 2010. 65

[94] R. O. Al-Kaysi, A. M. Muller, T.-S. Ahn, S. Lee, and C. J. Bardeen, *Langmuir*, vol. 21, no. 17, pp. 7990–7994, 2005. 66

[95] M. Ballester, I. Pascual, C. Carreras, and J. Vidal-Gancedo, *Journal of the American Chemical Society*, vol. 116, no. 10, pp. 4205–4210, 1994. 69

[96] I. Ratera and J. Veciana, *Chem. Soc. Rev.*, vol. 41, pp. 303–349, 2012. 69, 70

[97] L. Yuan, C. Franco, N. Crivillers, M. Mas-Torrent, L. Cao, C. S. Sangeeth, C. Rovira, J. Veciana, and C. A. Nijhuis, *Nature communications*, vol. 7, 2016. 70

[98] A. Y. Tesio, D. Blasi, M. Olivares-Marin, I. Ratera, D. Tonti, and J. Veciana, *Chem. Commun.*, vol. 51, pp. 17 623–17 626, 2015. 70

[99] L. Fajari, R. Papoular, M. Reig, E. Brillas, J. L. Jorda, O. Vallcorba, J. Rius, D. Velasco, and L. Julia, *The Journal of Organic Chemistry*, vol. 79, no. 4, pp. 1771–1777, 2014. 70, 71

[100] A. Heckmann, S. Dummler, J. Pauli, M. Margraf, J. Kohler, D. Stich, C. Lambert, I. Fischer, and U. Resch-Genger, *The Journal of Physical Chemistry C*, vol. 113, no. 49, pp. 20 958–20 966, 2009. 70, 71

[101] Q. Peng, A. Obolda, M. Zhang, and F. Li, *Angewandte Chemie International Edition*, vol. 54, no. 24, 2015. 71

[102] J. Veciana, C. Rovira, M. I. Crespo, O. Armet, V. M. Domingo, and F. Palacio, *Journal of the American Chemical Society*, vol. 113, no. 7, pp. 2552–2561, 1991. 71

[103] Y. Hattori, T. Kusamoto, and H. Nishihara, *Angewandte Chemie International Edition*, vol. 54, no. 12, pp. 3731–3734, 2015. 71

[104] Y. Hattori, "Rsc advances, 2015, 5, 64802-64805;(d) y. hattori, t. kusamoto and h. nishihara," *Angew. Chem. Int. Ed*, vol. 53, pp. 11 845–11 848, 2014. 71

[105] Y. Hattori, T. Kusamoto, T. Sato, and H. Nishihara, *Chemical Communications*, vol. 52, no. 91, pp. 13 393–13 396, 2016. 71

[106] Y. Hattori, T. Kusamoto, and H. Nishihara, *Angewandte Chemie International Edition*, vol. 53, no. 44, pp. 11 845–11 848, 2014. 71

[107] N. Crivillers, M. Mas-Torrent, S. Perruchas, N. Roques, J. Vidal-Gancedo, J. Veciana, C. Rovira, L. Basabe-Desmonts, B. J. Ravoo, M. Crego-Calama *et al.*, *Angewandte Chemie International Edition*, vol. 46, no. 13, pp. 2215–2219, 2007. 72

[108] C. Simao, M. Mas-Torrent, N. Crivillers, V. Lloveras, J. M. Artes, P. Gorostiza, J. Veciana, and C. Rovira, *Nature Chemistry*, vol. 3, no. 5, p. 359, 2011. 72

[109] J. Mei, N. L. Leung, R. T. Kwok, J. W. Lam, and B. Z. Tang, *Chem. Rev*, vol. 115, no. 21, pp. 11 718–11 940, 2015. 72

[110] G. M. Farinola and R. Ragni, *Chem. Soc. Rev.*, vol. 40, pp. 3467–3482, 2011. 72

[111] Y. Jiang, G. Li, W. Che, Y. Liu, B. Xu, G. Shan, D. Zhu, Z. Su, and M. R. Bryce, *Chem. Commun.*, vol. 53, pp. 3022–3025, 2017. 72

[112] J. Birks, "Excimers and Exciplexes," *Nature*, vol. 214, pp. 1187–1190, Jun. 1967. 86

[113] B. Valeur. Wiley-VCH Verlag GmbH, 2001. 86

[114] J. C. de Mello, H. F. Wittmann, and R. H. Friend, *Advanced materials*, vol. 9, no. 3, pp. 230–232, 1997. 88

[115] U. Giovanella, M. Pasini, and C. Botta. Springer International Publishing, 2016, pp. 145–196. 91

[116] M. Berberan-Santos, E. Bodunov, and B. Valeur, *Chemical Physics*, vol. 315, no. 1, pp. 171–182, 2005. 92

[117] V. Ptatschek, B. Schreder, K. Herz, U. Hilbert, W. Ossau, G. Schottner, O. Rahauser, T. Bischof, G. Lermann, A. Materny *et al.*, *The Journal of Physical Chemistry B*, vol. 101, no. 44, pp. 8898–8906, 1997. 93

[118] A. L. Wong, J. M. Harris, and D. B. Marshall, *Canadian Journal of Physics*, vol. 68, no. 9, pp. 1027–1034, 1990. 93

[119] K. K. Ng and G. Zheng, *Chemical Reviews*, vol. 115, no. 19, pp. 11 012–11 042, 2015. 109

[120] E. Campioli, C. Rouxel, M. Campanini, L. Nasi, M. Blanchard-Desce, and F. Terenziani, *Small*, vol. 9, no. 11, 2013. 109

[121] C. Fan and C. Yang, *Chemical Society reviews*, vol. 43, no. 17, pp. 6439–6469, 2014. 110

[122] M. Bruchez, M. Moronne, P. Gin, S. Weiss, and A. P. Alivisatos, *Science*, vol. 281, no. 5385, pp. 2013–2016, 1998. 111

[123] N. Panchuk-Voloshina, R. P. Haugland, J. Bishop-Stewart, M. K. Bhalgat, P. J. Millard, F. Mao, W.-Y. Leung, and R. P. Haugland, *Journal of Histochemistry and Cytochemistry*, vol. 47, no. 9, pp. 1179–1188, 1999. 111

[124] K. Sapsford, Y. Shubin, J. Delehanty, J. Golden, C. Taitt, L. Shriver-Lake, and F. Ligler, *Journal of Applied Microbiology*, vol. 96, no. 1, pp. 47–58, 2004. 111

[125] D. A. Agard, Y. Hiraoka, P. Shaw, and J. W. Sedat, "Chapter 13 fluorescence microscopy in three dimensions," *Methods in Cell Biology*, vol. 30, pp. 353 – 377, 1989. 111

[126] C. Blanco, M. Alonso, E. Lopez, A. Calleja, and M. Rico, in *Applied Power Electronics Conference and Exposition, 1996. APEC '96. Conference Proceedings 1996., Eleventh Annual*, vol. 2, Mar 1996, pp. 616–621 vol.2. 111

[127] L. Douminge, X. Feaugas, J. Bernard, and S. Mallarino, *Current Applied Physics*, vol. 13, no. 8, pp. 1751 – 1757, 2013. 111

[128] J. Ortyl, M. Galek, P. Milart, and R. Popielarz, *Polymer Testing*, vol. 31, no. 3, pp. 466 – 473, 2012. 111

[129] K. Ren, P. Serguievski, H. Gu, O. Grinevich, J. H. Malpert, and D. C. Neckers, *Macromolecules*, vol. 35, no. 3, pp. 898–904, 2002. 112

[130] K. Hakala, R. Vatanparast, S. Li, C. Peinado, P. Bosch, F. Catalina, and H. Lemmetyinen, *Macromolecules*, vol. 33, no. 16, pp. 5954–5959, 2000. 112

[131] A. Paul, P. K. Mandal, and A. Samanta, *The Journal of Physical Chemistry B*, vol. 109, no. 18, pp. 9148–9153, 2005. 114

[132] G. Reynolds and K. Drexhage, *Optics Communications*, vol. 13, no. 3, pp. 222 – 225, 1975. 116

[133] R. Chen, X. Yang, H. Tian, X. Wang, A. Hagfeldt, and L. Sun, *Chemistry of Materials*, vol. 19, no. 16, pp. 4007–4015, 2007. 120

[134] V. Twersky, *JOSA*, vol. 52, no. 2, pp. 145–171, 1962. 127

[135] V. V. Dyomin and I. G. Polovtsev, *Proc. ETOP 2007*, pp. 310–320, 2007. 127

[136] M. Mansuripur, *Classical optics and its applications, second edition.* Cambridge University Press, 1 2009. 127

[137] C. C. L. Ennio Arimondo and S. F. Yelin, Eds., ser. Advances In Atomic, Molecular, and Optical Physics. Academic Press, 2016, vol. 65. 129

[138] M. Born and E. Wolf, *Principles of Optics (7th Ed).* Cambridge University Press, 1999. 132